Study of Cold Nuclear Matter effect with prompt D^0 meson production in pPb collisions at LHCb

Emilie Maurice[1,2], Francesco Bossu[2], Frederic Fleuret[1,2], Yuanning Gao[3], Giulia Manca[4],
Patrick Robbe[2], Michael Winn[2], Zhenwei Yang[3], Yanxi Zhang[2], Laure Marie Massacrier[*]

[1]*Laboratoire Leprince-Ringuet, École polytechnique, CNRS/IN2P3, Palaiseau, France*
[2]*Laboratoire de l'Accélérateur Linéaire, Université Paris-Sud, CNRS/IN2P3, Orsay, France*
[3]*Tsinghua University, Beijing, China*
[4]*Università degli studi di Cagliari and INFN, Cagliari, Italy*
[*]*L'institut de physique nucléaire d'orsay, France*

Abstract

The productions of prompt D^0 mesons in proton-lead collisions in the forward and backward configurations are studied. The data are collected with the LHCb detector with $\sqrt{s_{NN}} = 5.02$ TeV, corresponding to an integrated luminosity of 1.06 ± 0.02 nb^{-1} (0.52 ± 0.01 nb^{-1}) in the proton-lead (lead-proton) configuration. The integrated cross-section is measured to be 230.6 ± 0.5(stat)± 13.0(syst)± 4.3(lumi) mb (252.7 ± 1(stat)± 20.0(syst)± 5.4(lumi) mb) for the forward (backward) rapidity range $1.5 < y^* < 4$ ($-5 < y^* < -2.5$), in the $p_{\rm T}$ range $0 < p_{\rm T} < 10$ GeV/c. Cold nuclear modification factors and forward-backward ratios are determined, suggesting suppression in the forward direction. This note describes the update of the previous result released in March 2016.

History

- version 4.4, Feb 2017 : new pp reference cross-section, RpPb are changed

- version 4.2, Feb 2017 : implemented comments from Roberta.

- version 4.1, Jan 2017 : implemented first comments from Valery.

- version 4.0 December 2016: New version of the analysis with the requested updates:

  - The 10% stripping prescale factor was removed and all the luminosity available in the sample is used. The luminosity was $0.106(0.05)$ nb^{-1} and it is now $1.06(0.52)$ nb^{-1} for the forward (backward) sample.

  - The sample was restripped with new code. This allowed to remove the p_T threshold requirement, in order to keep more low-pT tracks which are important to calibrate the low momentum bins of D^0. At the same time, the prescale of the PID calibration line was increased from 0.89 to 1.

  - The measurement was extended to the p_T range $0 < p_\mathrm{T} < 10 \, \mathrm{GeV}/c$ (it was $0 < p_\mathrm{T} < 8 \, \mathrm{GeV}/c$).

  - The size of the simulation sample was doubled.

  - The efficiency of the MCTruth match in simulation was re-evaluated with a more precise method.

  - The PID efficiency was measured using the tracking calibration method which became available, especially for the low p_T bins, as a result of the new stripping line implemented.

  - The method and function used to fit the signal and background yields and the χ^2_{IP} were changed. We now follow more like the pp analysis, where a two step fit is performed. Invariant distribution was first fitted to determine the numbers of signals and backgrounds, then the χ^{IP} is fitted with the signal and background yields contraint from the invaiant mass fit. The fitted range of χ^2_{IP} is also relaxed.

  - Added systematic uncertainty on the fit, more like the pp analysis.

  - Changed method to extract fraction of prompt D^0, from a global number to bin by bin numbers due to increase of statistics.

  - Measurements of R_{pPb} as a function of rapidity also presented.

- March 2015: Results shown in version 3.3 of the analysis note approved to be shown at Moriond QCD 2016 (LHCb-CONF-2016-003).

Contents

1 Introduction

In hadronic collisions heavy quarks are produced in scattering processes with large momentum transfer. Theoretical predictions based on perturbative Quantum Chromo-Dynamics (QCD) describe the p_T differential charm production cross sections in pp collisions at different energies [1–6].

The interpretation of heavy-ion collision experimental results is consistent with the formation of a high-density colour-deconfined medium, the Quark-Gluon Plasma (QGP) [6, 7]. Heavy quarks are sensitive to the transport properties of the medium since they are produced on a short time-scale and traverse the medium interacting with its constituents. In Pb–Pb collisions at $\sqrt{s}_{NN} = 2.76$ TeV, the D-meson nuclear modification factor R_{AA}, defined as the ratio of the yield in nucleus-nucleus collisions to that observed in the pp ones scaled by the number of binary nucleon-nucleon collisions, indicates a strong suppression of the D-meson yield for $p_T > 2$ GeV/c [8] which is interpreted as due to in-medium energy loss [9–13].

A complete understanding of the Pb–Pb results requires an understanding of cold-nuclear-matter (CNM) effects in the initial and final state, which can be accessed by studying p–Pb collisions assuming that the QGP is not formed in these collisions. In the initial state, the nuclear environment affects the quark and gluon distributions (PDF), which are modified in bound nucleons depending on the parton fractional momentum x and the atomic mass number A [14,15], i.e. nuclear PDF (NPDF) are different from those in free nucleons.

At LHC energies, with small x where gluon density is high, the most relevant effect is gluon saturation, which can modify the D-meson production significantly at low p_T. This effect can be described either by means of calculations based on phenomenological modification of the Parton Distribution Functions (PDFs) [16–18] or with the Colour Glass Condensate (GCG) effective theory [19–22]. Partons can also lose energy in the initial stages of the collision via initial-state radiation, thus modifying the centre-of-mass energy of the partonic system [23] or experience transverse momentum broadening due to multiple soft collisions before the $c\bar{c}$ pair is produced [24]. Recent calculations of parton energy loss in the nuclear medium suggest that the formed $c\bar{c}$ pair is also affected by these processes in p–Pb collisions [25].

The presence of final-state effects in small collision systems is suggested by recent studies on long-range correlations of charged hadrons [26–29] in p–Pb collisions. This results on the species-dependent nuclear modification factors of pions, kaons and protons [30] in d–Au collisions and on the larger suppression of the $\psi(2S)$ meson with respect to the J/ψ in both d–Au [31] and p–Pb [32–34] collisions.

Previous studies to address cold-nuclear-matter effects in heavy-flavour production were carried out at RHIC by measuring the production of leptons from heavy-flavour hadrons decays in d–Au collisions at $\sqrt{s} = 200$ GeV [35]. PHENIX measured an enhancement of about 40% of the heavy-flavour decay electrons in the 20% most central d–Au collisions with respect to pp collisions [35]. PHENIX also measured an enhancement (suppression) of heavy-flavour decay muons at backward (forward) rapidities in d–Au collisions [36]. The

1

difference observed in the two rapidity regions exceeds predictions based on initial parton density modifications, suggesting the presence of other cold-nuclear-matter effects. The measurement of fully reconstructed charmed hadrons in p–Pb collisions at the LHC can shed light on the different aspects of cold-nuclear-matter effects mentioned above and, in particular, can clarify whether the observed suppression of D-meson production in Pb–Pb collisions is a genuine hot QCD matter effect. In this paper we present the measurement of the cross sections and of the nuclear modification factors, R_{pPb}, of prompt D^0 mesons in p–Pb collisions at $\sqrt{s} = 5.02$ TeV performed with the LHCb [37] detector at the LHC.

This measurement is an update of the previous measurement documented in version 3.3 of this analysis note and in the conference note LHCb-CONF-2016-003. This result is meant to superseed the previous result and aims to be published in a peer-reviewed journal.

2 Data sets and Selections

2.1 Data sets

The analysis is performed with the pPb collision data collected by the LHCb detector in early 2013. Two beam configurations were used during the data taking: the Forward (Fwd) collisions, where the proton beam traverses the LHCb detector from the VELO to the MUON stations and collides with the lead beam from the other direction in the interaction point; the Backward (Bwd) collisions, where the proton beam enters the LHCb detector from the MUON station. The data were collected with both magnet-up and magnet-down conditions. Very loose triggers were applied with both L0 and HLT2 trigger stage accepting all events (PassThrough), and HLT1 implementing a few NoBias, MicroBias and Muon lines. Following the LHCb bunch scheme, several TCKs were used, differing in the HLT1 trigger lines. Only data flagged with good quality (in fact all data are flagged as OK) are used for this analysis. Some of the data are further filtered following the analysis of J/ψ production in pA [38]. We ignore the runs with data taking conditions significantly different from the bulk of the data, including those with TCK `0x6a1710`, and run indexes (135710, 135711, 135900, 135901) because of muon inefficiency problem, those with TCK `0x6E0049` because they have a higher SumEt threshold, and those with TCK `0x6F004A` since the `Hlt1MBMicroBiasVelo` line was significantly prescaled. The luminosity for the data used in the J/ψ production analysis [38], i.e. with these filtering, has been determined with a precision of about 2%. The integrated luminosities are $(0.52 \pm 0.01)\,\mathrm{nb}^{-1}$ and $(1.06 \pm 0.02)\,\mathrm{nb}^{-1}$ for the selected Bwd data and Fwd data sample respectively[1]

Simulated samples with about 3M $D^0 \to K^- \pi^+$ decays are generated with D^0 production in pp collisions to study the reconstruction and selection efficiencies. The LHCb simulation event type is `22162000`, and the production tag `sim08e` is used for these productions to describe the detector condition. The same reconstruction pass `Reco 14r1` is used to reconstruct the event. Although the description of the detector in simulation is

---

[1]The relative uncertainties are 2.13% and 1.86% respectively.

supposed to be similar to real detector, the event multiplicity in pp collisions is significantly different from that in pA collisions. In order to correctly estimate the efficiency, which varies with the event multiplicity, the event multiplicity in simulation must be corrected, and the correction is done separately for Bwd and Fwd data. The procedure will be described in detail in section 3.

2.2 Selection

The D^0 candidate is reconstructed from a pion and a kaon track according to the decay[2] $D^0 \to K^- \pi^+$ by the LHCb official stripping `v20r3p1` (same as stripping `v20` but on pPb data instead of pp data), with the stripping line `D02HHForXSecD02HHLine`. The stripping selection criteria follow the LHCb previous analyses of D^0 production cross-section in pp collisions at $\sqrt{s} = 7\,\text{TeV}$ [39] and $\sqrt{s} = 13\,\text{TeV}$ [40]. Both tracks are required to have large transverse momentum, $p_\text{T} > 250\,\text{MeV}/c^2$, not to come from primary vertices (PV) by requiring minimum impact parameter significance, $\chi^2_\text{IP} > 4$. The tracks are also asked to be in the kinematic range $2 < \eta < 5$, where η is the pseudo-rapidity of the hadron track. The K^- track is required to be more kaon-like by requiring $\text{DLL}_{K\pi} > 0$, and the π^+ track more pion like requiring $\text{DLL}_{K\pi} < 3$. The D^0 candidate is required to have a good vertex fit quality by requiring $\chi^2/\text{ndf}(\text{vtx}) < 25$, and the vertex should be displaced from PV by requiring the D^0 to have either a significant vertex displacement (VD), $\chi^2(\text{VD}) > 16$ or a large measured proper decay time[3] $\tau > 0.15\,\text{ps}$. The prompt D^0 should have its measured momentum coincident with the line formed by the PV and the decay vertex, so the angle (direction angle) between the two is required to be less than 35 mrad ($2°$ or about 10% of the LHCb acceptance). This condition reduces the D^0 from b-hadron decays, and combinatorial backgrounds with one or both final state tracks coming from secondary decays. The selections are summarized in Table 1.

Table 1: Stripping selections of D^0 candidates.

Quantity	Selections
p_T (track)	$> 250\,\text{MeV}/c$
χ^2_IP (track)	> 4
p (track)	$3.2 < p < 100\,\text{GeV}/c$
η (track)	$2 < \eta < 5$
$\text{DLL}_{K\pi}(K^-)$	> 0
$\text{DLL}_{K\pi}(\pi^+)$	< 3
Direction angle	$< 35\,\text{mrad}$
$\chi^2/\text{ndf}(\text{vtx})$	< 25
Lifetime	$\chi^2(\text{VD}) > 16$ or $\tau > 0.15\,\text{ps}$

In the new version of the analysis the sample was restripped with new code. For the

---

[2]Charge conjugation is implied throughout the note unless otherwise specified.
[3]The lifetime of D^0 is $0.4101 \pm 0.0015\,\text{ps}$.

PID calibration sample $D^{*+} \to D^0 \pi^+$, to be discussed later in more detail, this allowed to remove the p_T threshold requirement of D^0, in order to keep more low-pT tracks which are important to calibrate the low momentum bins of D^0. At the same time, the prescale of the PID calibration line was increased from 0.89 to 1.

The offline selection is the same for the Bwd and Fwd sample and it has been chosen in order to reduce the background, particularly high in the Bwd data sample, in which more random combinations are present. Ghost tracks are suppressed by cutting on the ghost probability (less than 0.3). The requirements on the transverse momenta of the K^-, π^+ tracks are tightened to be $p_T > 400 \,\mathrm{MeV}/c$, and impact parameter significance to $\chi^2_{\mathrm{IP}} > 9$. The PID selections are tightened to $\mathrm{DLL}_{K\pi} > 5$ for the kaon, and $\mathrm{DLL}_{K\pi} < 0$ for the pion. To remove backgrounds coming from tracks from final state interactions with the detector, the impact parameter of the tracks is required to be less than $3\,\mathrm{mm}$. The D^0 candidate is asked to have a vertex fit quality requirement $\chi^2/\mathrm{ndf(vtx)} < 6$ and reconstructed proper decay time $\tau > 0.3\,\mathrm{ps}$. This variable $\chi^2_{\mathrm{IP}}(D^0)$ is fitted to determine the fraction of contamination of D^0-from-b decays, which will be described in detail in section 4, and thus no selections is applied to it. Due to limited statistics at high D^0 transverse momentum, following the previous charm cross-section analyses, the measurement is made in the range $p_T(D^0) < 10\,\mathrm{GeV}/c$, $2.0 < y < 4.5$. The offline selections are summarized in Table 2. Since the intensity of the beam was very low, the pileup is estimated to be negligible, confirmed also by the number of reconstructed PVs per event which is 1.02 for events with a reconstructed D^0 candidate.

After all the selections, there are about 1.4M (1.1M) D^0 candidates in the Fwd (Bwd) sample in the data. The simulation sample after the selections have around 0.26M signal candidates, corresponding to 3.1M generated $D^0 \to K^- \pi^+$ decays. Because of contribution of backgrounds in data, eventually the statistical uncertainty in simulation is roughly similar to those in data. The number of signal decays generated, after stripping and offline seletions in simulation are given in Table 3, for prompt D^0 and D^0-from-b separately. From Table 3, it can be seen that the $D^0-$from$-b$ has higher efficiency due to larger average decay length and thus larger probablity to pass the $\tau(D^0) > 0.3\,\mathrm{ps}$ and $\chi^2_{\mathrm{IP}}(\mathrm{track}) > 9$ cuts.

All the events in which a D^0 candidate is reconstructed are found to have the `Hlt1MBMicroBiasVelo` trigger fired while the L0 and HLT2 were configured in pass-through mode, so the trigger efficiency for D^0 event is assumed to be 100%.

3 Cross-section determination

The determination of the double-differential production cross-section for prompt D^0 requires the knowledge of the numbers of prompt D^0 in bins of the kinematic variables[4] y^* and p_T, where p_T and y^* are defined in the nucleon-nucleon (denoted as pN) center-of-mass frame, and the positive z-axis is defined as the direction of the proton beam.

---

[4]The superscript "*" means that the rapidity y is defined in the nucleon-nucleon center-of-mass frame.

Table 2: Offline selections of D^0 candidates.

Quantity	Selections
p_{T} (track)	$> 400 \, \mathrm{MeV}/c$
χ^2_{IP} (track)	> 9
IP (track)	$< 3 \, \mathrm{mm}$
ProbNNghost (track)	< 0.3
$\mathrm{DLL}_{K\pi}(K^-)$	> 5
$\mathrm{DLL}_{K\pi}(\pi^+)$	< 0
$\chi^2/\mathrm{ndf}(\mathrm{vtx})$	< 6
Decay time	$\tau > 0.3 \, \mathrm{ps}$
$p_{\mathrm{T}}(D^0)$	$< 10 \, \mathrm{GeV}/c$
$y(D^0)$	$(2.0 - 4.5)$

Table 3: Number of signal decays in simulation at each selection step.

Simulation steps	Prompt D^0	$D - from - B$
Generated	2948K	198K
After stripping sel.	393K	44K
After offline sel.	248K	35K

The laboratory frame does not coincide with the center-of-mass frame of the proton-nucleon system, which has a rapidity of $\delta y = 0.5 * \log(A_{\mathrm{Pb}}/Z_{\mathrm{Pb}}) = 0.465$ in the laboratory frame. Therefore the rapidity in the pN rest frame, y^*, is shifted by a constant value with respect to the rapidity in the laboratory frame, $y = y^* + 0.465$.

Here we define the rapidity with the direction of proton beam as positive z-axis (lead beam as negative z-axis). We thus define the rapidity acceptance in the pN center-of-mass frame to be $1.5 < y^* < 4$ ($-5 < y^* < -2.5$) for the Fwd (Bwd) collision [5]. For the differential cross-section determination, the bin width for p_{T} is $1 \, \mathrm{GeV}/c$ and for y^* 0.5; the signal yields and efficiency are determined separately for each bin, thanks to the good resolution.

The double differential cross-section for prompt D^0 production in a given (p_{T}, y^*) bin is thus defined as

$$\frac{\mathrm{d}^2\sigma}{\mathrm{d}y\mathrm{d}p_{\mathrm{T}}} = \frac{N(D^0 \to K^-\pi^+)}{\mathcal{L} \times \varepsilon_{\mathrm{tot}} \times \mathcal{B}(D^0 \to K^-\pi^+) \times \Delta y \times \Delta p_{\mathrm{T}}} \tag{1}$$

where

- $N(D^0 \to K^-\pi^+)$ is the number of prompt D^0 signals reconstructed through the $D^0 \to K^-\pi^+$ decay channel; it is obtained by the fit described in section 4;

---

[5]To be more precise, the rapidity range is $1.965 < |y| < 4.465$ ($2.0355 < |y| < 4.5355$) for the Fwd (Bwd) pPb collision in the laboratory frame; the Bwd collision corresponds to more forward region ($+0.07$) in the LHCb acceptance.

159   • $\mathcal{L}$ is the integrated luminosity.

160   • ε_{tot} is the total efficiency determined in each (p_{T}, y^*) bin, described in detail in
161   Section 5;

162   • $\mathcal{B}(D^0 \to K^- \pi^+) = (3.94 \pm 0.04)\%$ is the branching fraction of the decay $D^0 \to K^- \pi^+$
163   including $D^0 \to K^+ \pi^-$, obtained from the PDG 2014 review [41];

164   • $\Delta p_{\text{T}} = 1\,\text{GeV}/c$ is the bin width of the D^0 transverse momentum;

165   • $\Delta y = 0.5$ is the bin width of the D^0 rapidity.

166   The forward and backward cross-section measurements are in the range $p_{\text{T}}(D^0) <$
167 $10\,\text{GeV}/c$. The rapidity acceptance in the laboratory frame for D^0 is roughly $2 < y < 4.5$
168 for the Fwd collision, and $-4.5 < y < -2$ for the Bwd collision.
169   The total cross-section over a specific range is determined by integrating the double
170 differential cross-section over that particular range. The nuclear modification factor is
171 defined to be the production cross-section in pPb collisions, normalized by the number
172 of nucleons in Pb nucleus [42], relative to that in pp collisions corresponding to the same
173 nucleon-nucleon center-of-mass energy $\sqrt{s_{\text{NN}}}$,

$$R_{p\text{Pb}} = \frac{1}{A} \frac{\frac{\mathrm{d}\sigma_{p\text{Pb}}}{\mathrm{d}y^*(\mathrm{d}p_{\text{T}})}(y^*(p_{\text{T}}), \sqrt{s_{\text{NN}}})}{\frac{\mathrm{d}\sigma_{pp}}{\mathrm{d}y^*(\mathrm{d}p_{\text{T}})}(y^*(p_{\text{T}}), \sqrt{s_{\text{NN}}})}, \tag{2}$$

174 studied in bins of p_{T} and y^* integrated over y^* and p_{T} respectively. As you can see,
175 $R_{p\text{Pb}}$ is calculated integrated in all centralities, i.e. averaged over the number of binary
176 proton-nucleon collisions, which is estimated to be around 7 by the ALICE experiment at
177 LHC [43]. Another interesting variable is the forward-backward production ratio for the
178 same absolute rapidity, defined as

$$R_{\text{FB}} \equiv R_{p\text{Pb}}(+|y^*|(p_{\text{T}}))/R_{p\text{Pb}}(-|y^*|(p_{\text{T}})), \tag{3}$$

179 also studied in bins of p_{T} and y^* integrated over y^* and p_{T} respectively.

4   Signal yield determination

181 The signal yield is determined from extended unbinned maximum likelihood fit to the
182 $M(K\pi)$ invariant mass distribution. Following previous analyses [39, 40, 44], the signal
183 shape is described by a crystal ball (CB) function [45] plus a Gaussian. The two components
184 share the mean value μ. In the CB function, we fix $n = 1$ constraint from physics, while a
185 is fixed to 2.35, the value obtained from simulation. The fraction of the CB component is
186 fixed to 0.85, and the width of the Gaussian to that of CB is fixed to 1.8. These parameters
187 are also obtained from simulation, and they are found to describe very well the simulation
188 sample in different kinematic bins. The background is described by a linear function. We

6

fit the candidates in the range $M \pm |\Delta M|$ around the observed D^0 mass as $M = \text{MeV}/c^2$, with $|\Delta M| = 75\,\text{MeV}/c^2$. In Fig. 1, the fitted signal yield in different (p_{T}, y^*) bins are given. The σ of the CB is known to depend on D^0 kinematics while the μ could also be kinematic dependent due to imperfect detector alignment, so in the fit the mean μ and σ are independent parameters in each bin, and the fitted results are summarized in section D of the appendix.

To discriminate prompt D^0 and D^0 from b, the distribution of $\log(\chi^2_{\text{IP}}(D^0))$ (10 based logarithm) is fitted to determine the fraction of $D^0-\text{from}-b$, which is the number of $D^0-\text{from}-b$ candidates over the sum of $D^0-\text{from}-b$ and prompt D^0. The $\log(\chi^2_{\text{IP}}(D^0))$ for prompt D^0 decays is modelled with a modified gaussian function (f_{AGE}), where the width is allowed to be asymmetric with respect to the mean, and the tails are described by exponential functions

$$
f_{\text{AGE}}(x; \mu, \sigma, \epsilon, \rho_{\text{L}}, \rho_{\text{R}}) =
\begin{cases}
e^{\frac{\rho_{\text{L}}^2}{2} + \rho_{\text{L}} \cdot \frac{x-\mu}{(1-\epsilon)\cdot\sigma}} & x < \mu - (\rho_{\text{L}} \cdot \sigma \cdot (1-\epsilon)), \\
e^{-\left(\frac{x-\mu}{\sqrt{2}\cdot\sigma\cdot(1-\epsilon)}\right)^2} & \mu - (\rho_{\text{L}} \cdot \sigma \cdot (1-\epsilon)) \leq x < \mu, \\
e^{-\left(\frac{x-\mu}{\sqrt{2}\cdot\sigma\cdot(1+\epsilon)}\right)^2} & \mu \leq x < \mu + (\rho_{\text{R}} \cdot \sigma \cdot (1+\epsilon)), \\
e^{\frac{\rho_{\text{R}}^2}{2} - \rho_{\text{R}} \cdot \frac{x-\mu}{(1+\epsilon)\cdot\sigma}} & x \geq \mu + (\rho_{\text{R}} \cdot \sigma \cdot (1+\epsilon)).
\end{cases}
\tag{4}
$$

as it was done in previous analyses [40, 44] The tail parameters ρ_L, ρ_R and the asymmetry parameter ϵ are determined from fits to simulated sample and are fixed to be $1.3, 1.6, -0.3$, respectively. Fits to simulated events in different D^0 p_{T} and y bins indicate that the parameters have no strong dependence on the kinematics, however there are variations from bin to bin due to fluctuation. We assume that there are no kinematic dependency for these parameters within statistical uncertainties, and take the average value as nominal results, and assign systematics to this by studying the variation of the results when these parameters are changed, as described below in section 6.1.

In the Bwd sample, the fraction of $D^0-\text{from}-b$ is small, and background contribution is large, so fitting to data doesn't have the power to determined the parameters of the $D^0-\text{from}-b$ component. On the other hand, they are fixed to the values obtained from the Fwd sample, which are also not very different from values seen in simulation.

The $\log(\chi^2_{\text{IP}}(D^0))$ distribution for $D^0-\text{from}-b$ component is described by a Gaussian function, while the one for combinatorial background is constructed from the sideband region $[M_{D^0} - 75\,\text{MeV}/c^2, M_{D^0} - 40\,\text{MeV}/c^2]$ and $[M_{D^0} + 40\,\text{MeV}/c^2, M_{D^0} + 75\,\text{MeV}/c^2]$, which is more than 5σ away from the signal peak on average, with $\sigma \sim 7.5\,\text{MeV}/c^2$. A kernel density estimate PDF is used to model the distribution in the sideband as a template in the $\log(\chi^2_{\text{IP}}(D^0))$ fit. The fit is performed in each bin of D^0 p_{T} and y for events within $\pm 20\,\text{MeV}/c^2$ around the fitted mean value of the mass (defined as the signal region), and the number of background events in the signal region is constrained to be consistent with that obtained from invariant mass fit projected into this signal region, using a Gaussian likelihood function for the constraint.

The fitted fractions in different D^0 p_{T} and y^* bins are given in Figs. 2. From the plot we can observe that the fraction lies in the range $0 - 10\%$, and it increases with increasing
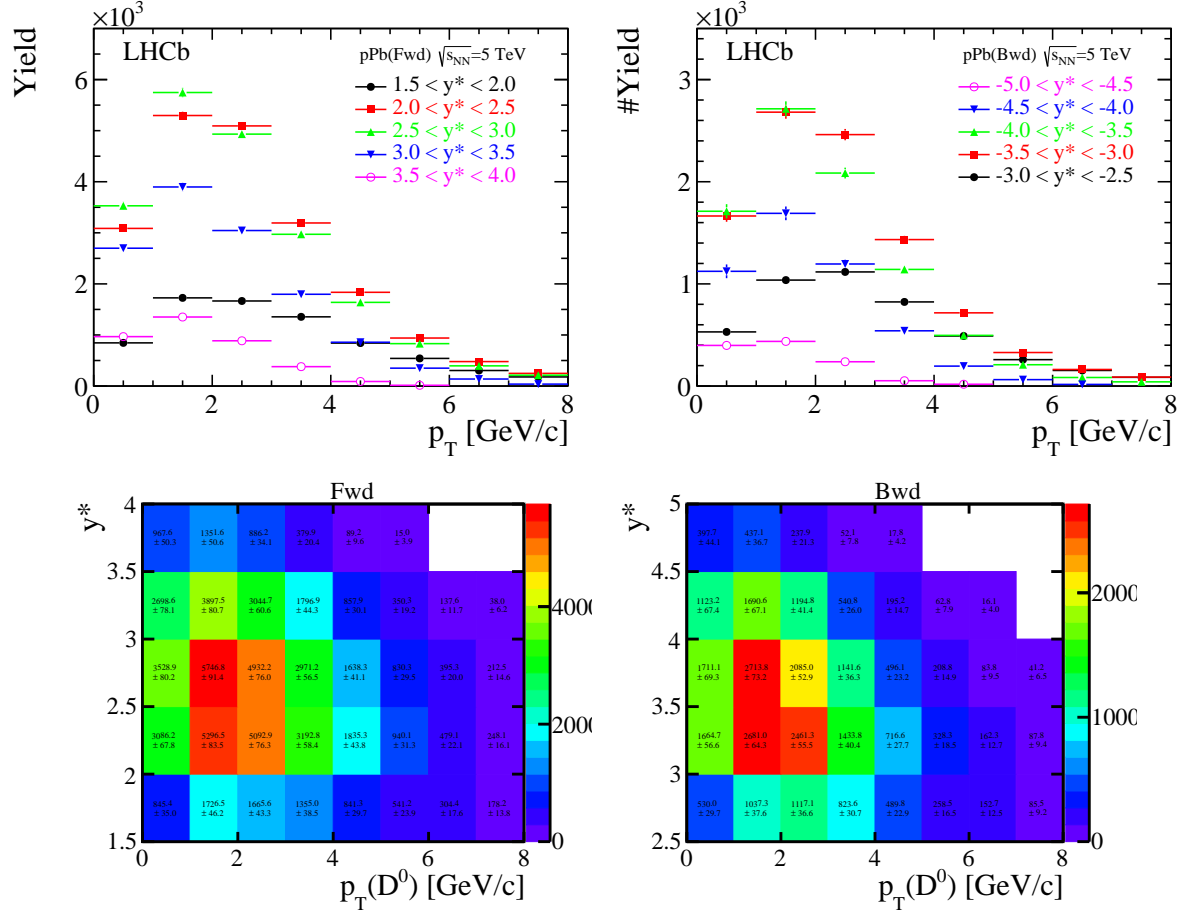
Figure 1: The fitted total D^0 signal yields as a function of p_T and y^* for (left) Fwd and (right) Bwd real data configuration. The empty bins are regions in which the statistics was too low and the fit failed.

p_T. It should be noted that these fractions should not be used to extract the production cross section of b-hadrons from that of D^0 production. In fact, the two components have very different efficiencies, in particular the lifetime-related selections favors b-hadrons.

The invariant mass and $\log \chi^2_{\mathrm{IP}}(D^0)$ distributions, together with the fits are given in Figs. 3 and 4 for two particular kinematic bins, for the Fwd and Bwd sample respectively. Good agreements are found between the mass and $\log \chi^2_{\mathrm{IP}}(D^0)$ distributions of signals in data and simulation. The $\log \chi^2_{\mathrm{IP}}(D^0)$ distributions for the prompt D^0 and the sideband are given in section D in appendix.
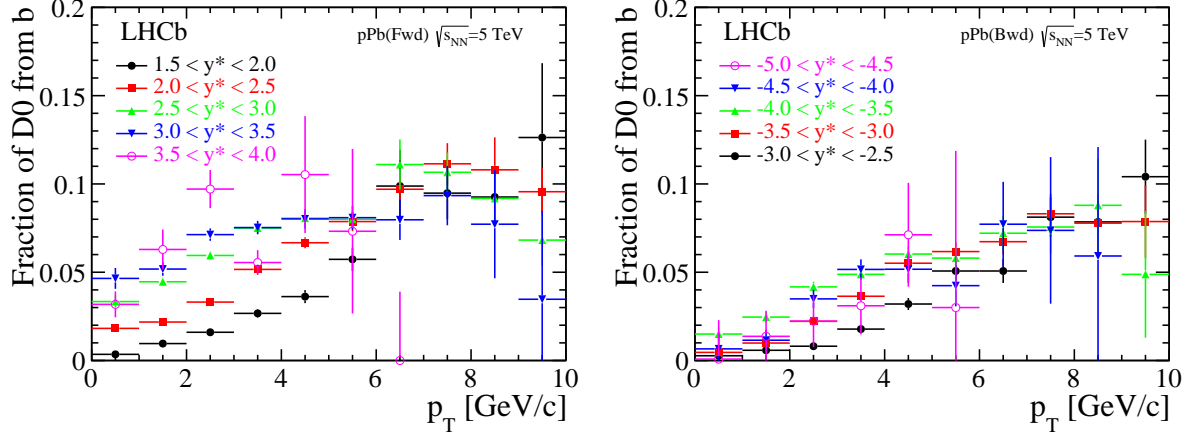
Figure 2: The fitted fractions of $D^0-$from$-b$ as a function of p_T and y^* for (left) Fwd and (right) Bwd data configuration. Only uncertainties returned by the fit are shown.
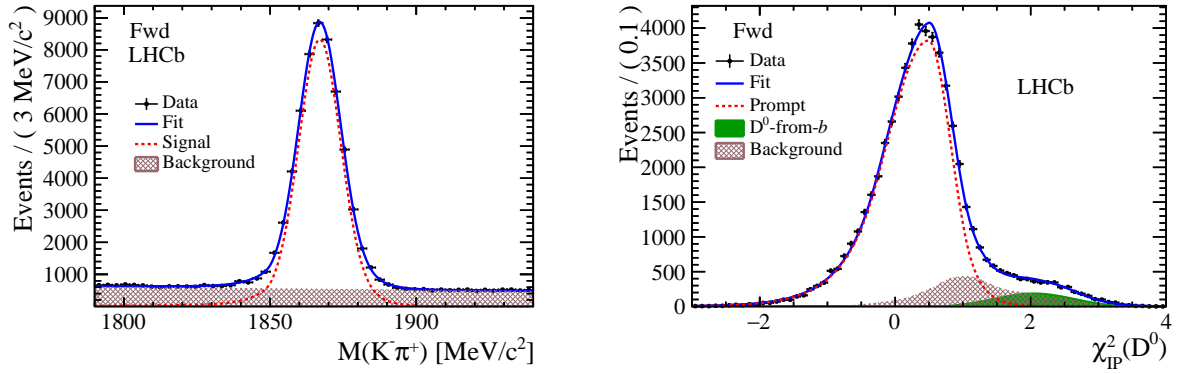

Figure 3: The (left) $M(K^-\pi^+)$ and (right) $\chi^2_{IP}(D^0)$ distributions and the fit result for the Fwd data sample for the kinematic bin $2.5 < y^* < 3, 2 < p_T < 3\,\text{GeV}/c$. The "Background" means combinatorial background.
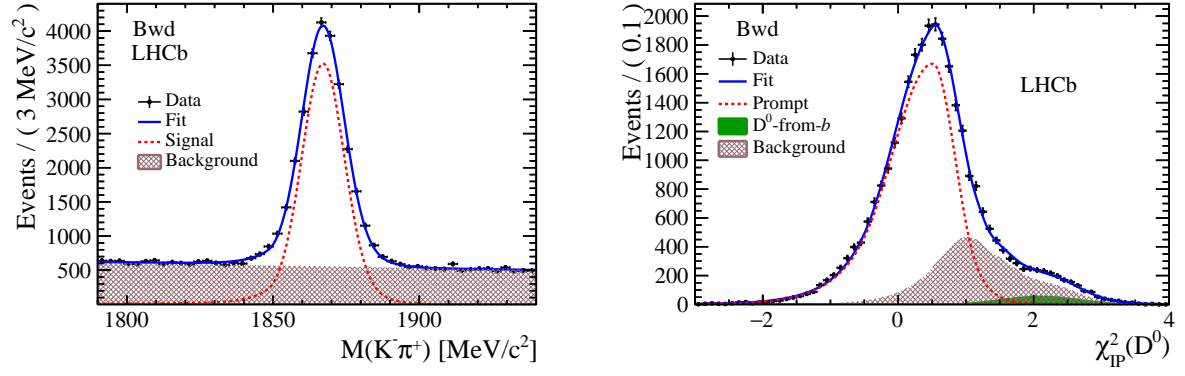
Figure 4: The (left) $M(K^-\pi^+)$ and (right) $\log \chi^2_{\mathrm{IP}}(D^0)$ invariant mass distributions and the fit result for the Bwd data sample for the kinematic bin $-4 < y^* < -3.5, 2 < p_{\mathrm{T}} < 3\,\mathrm{GeV}/c$. The "Background" means combinatorial background
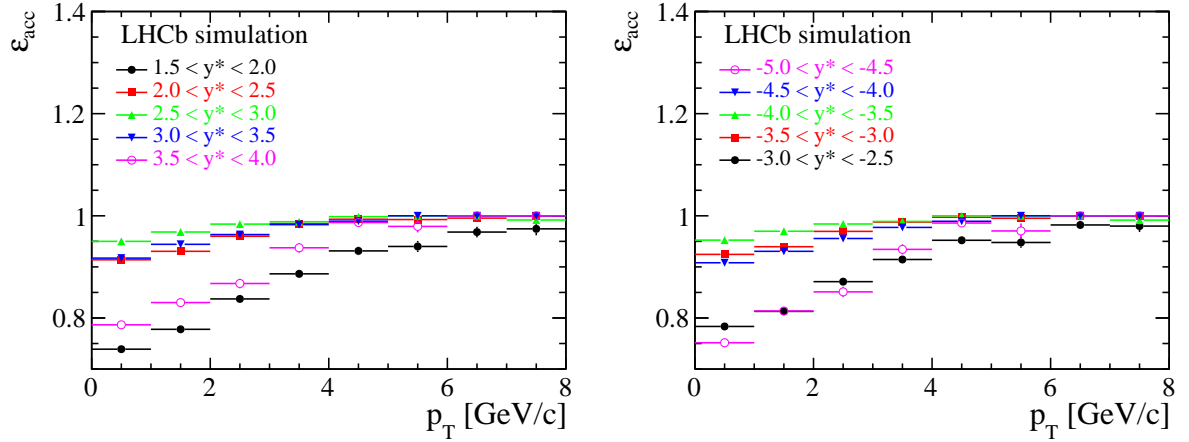
Figure 5: Geometrical acceptance efficiency ϵ_{acc} calculated using simulated events as a function of p_{T} and y^* of the prompt D^0 for (left) Fwd and (right) Bwd configuration. Only the statistical uncertainties are shown.

5 Efficiency determination

The total efficiency ϵ_{tot} is splitted into three parts, the geometrical acceptance efficiency ϵ_{acc}, the reconstruction and selection efficiency $\epsilon_{\mathrm{rec\&sel}}$ (without PID efficiency) and the PID efficiency ϵ_{PID}, according to the formula

$$\epsilon_{\mathrm{tot}} \equiv \epsilon_{\mathrm{acc}} \times \epsilon_{\mathrm{rec\&sel}} \times \epsilon_{\mathrm{PID}} \tag{5}$$

The efficiencies are determined in each p_{T} and y^* bin of the D^0 meson. In the following we address the determination of each efficiency component separately.

5.1 Geometrical acceptance efficiency

The geometrical acceptance is defined as

$$\epsilon_{\mathrm{acc}} \equiv \frac{D^0 \text{ with } K^- \pi^+ \text{ in LHCb acceptance}}{\text{Generated } D^0}. \tag{6}$$

Being in the LHCb acceptance means that the particles are within a polar angle $[10, 400]$ mrad defined with respect to the beam direction, without considering the bending in the LHCb magnet field. The efficiency ϵ_{acc} is determined using a generator level simulation sample which doesn't impose any geometrical acceptance requirement on either of the tracks.

In Fig. 5, the efficiency in each p_{T} and y^* bin for the prompt D^0 meson is shown for Fwd and Bwd configuration. The values are summarized in Tables 12 and 13 in appendix A.
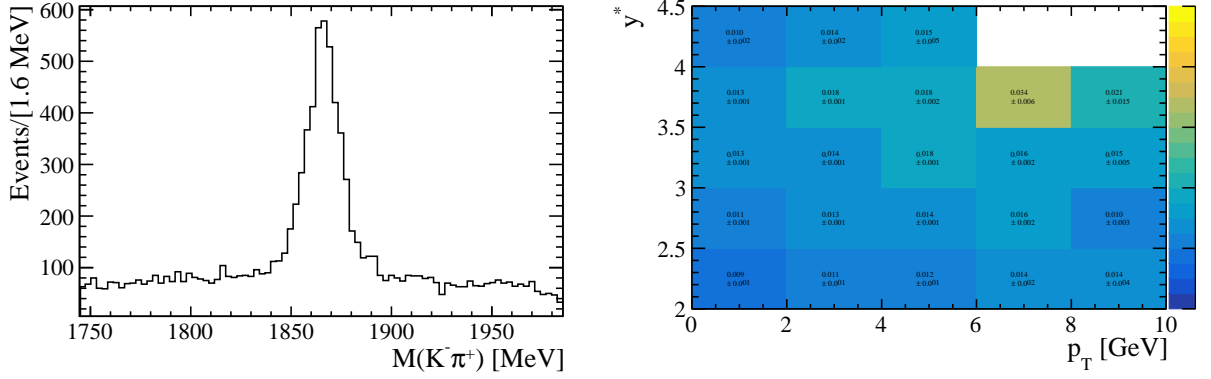
11

Figure 6: (Left) Invariant mass distributions of $D^0 \to K^- \pi^+$ decays that are not matched in simulation. (Right) Truth matching inefficiency in bins of D^0 p_{T} and y. There are no events of this type in the region with $p_{\mathrm{T}} > 6\,\mathrm{GeV}/c$ and $y^* > 4$.

5.2   Reconstruction and selection efficiency

The reconstruction&selection efficiency is estimated as

$$\epsilon_{\mathrm{rec\&sel}} \equiv \frac{\sum D^0 \text{ in acceptance, reconstructed and selected}}{D^0 \text{ with } K^- \pi^+ \text{ in LHCb acceptance}}. \tag{7}$$

It includes the efficiency of reconstructing the two hadron tracks and the refinement of the D^0 signals, with the selections that are listed in Table 2 (excluding the particle identification requirement). The efficiency is determined using truth matched $D^0 \to K^- \pi^+$ decays in the pp simulation sample, and corrected for the occupancy effects in the pPb collisions as described below.

5.2.1   Truth Matching Efficiency

The truth matching algorithm efficiency has been checked by plotting the $K\pi$ invariant mass distribution in the Monte Carlo for $D^0 \to K^- \pi^+$ signal decays which were not flagged as "true" D^0 from the algorithm (i.e., they had $D0\_TRUEID == 0$), shown in Fig. 6, left. The inefficiency is evaluated by taking the number of the not matched events which fall into the D^0 invariant mass window after sideband subtraction, as thus they should be real $D^0 \to K^- \pi^+$ signal decays. The inefficiency is shown in bins of D^0 transverse momentum and rapidity in Fig. 6, right. Since the inefficiency is small and no significant kinematic dependency is found, we take the average inefficiency 1.35%. Since this effect would result in an underestimate of the efficiency (as these events would be present in the data), the reconstruction&selection efficiency calculated using truth matched signals is multiplied by 1.0135. The uncertainty of the correction 0.02% is neglected.

12

5.2.2 Tracking Efficiency

The difference in tracking efficiency in data and simulation needs to be taken into account as well. The difference is parameterized as the efficiency ratio in bins of momentum (p) and eta (η) of the final state tracks, studied by the tracking group [https://twiki.cern.ch/twiki/bin/view/LHCb/LHCbTrackingEfficiencies]. We correct the tracking efficiency in simulation by assigning each event a correction factor, as the product of the tracking efficiency ratios for the K^- and π^+ tracks, when we use Eq. 7 to determine the efficiencies ($\epsilon(x)$, $\epsilon(p_{\mathrm{T}}, y^*)$), i.e. (with or without further binning in other variables)

$$\epsilon_{\mathrm{rec\&sel}} \equiv \frac{\sum_{D^0 \text{ reconstructed and selected}} w_i(p_{K^-}, \eta_{K^-}) \times w_i(p_{\pi^+}, \eta_{\pi^+})}{D^0 \text{ with } K^-\pi^+ \text{ in LHCb acceptance}}. \tag{8}$$

. Since the tracking efficiency ratios are measured precisely (using 2012 data), the corresponding systematic uncertainty from the uncertainties of the ratios are negligible.

5.2.3 Dependence on detector occupancy

It is known that LHCb reconstruction efficiency slightly depends on the detector occupancy, with efficiency reduced for high multiplicity events. Here by "detector occupancy", we mean any variables that could be used to measure how much the event is populated, namely the number of particles produced in the event. At LHCb, the number of reconstructed charged tracks, the number of VELO clusters and T-station clusters could be used for this purpose. The detector occupancy distributions in the pp simulation, Fwd and Bwd pPb collisions data are different, especially in the case of Bwd collision. Figure 13 shows the multiplicity of charged tracks, VELO clusters, sum of OT and IT clusters for pp simulation sample, Fwd and Bwd pPb collision respectively. It is clearly seen the increase of event activity for Fwd and Bwd pPb collisions w.r.t. pp simulated events, especially in the Bwd collisions. The distributions of the number of reconstructed PVs per event, and the number of tracks in the reconstructed PVs are shown Fig. 15, which suggests that the high detector occupancy in pA data is due to the large number of particles produced in the primary collisions. We use an "ad hoc" pp simulation sample, generated with a larger number of PVs per event to simulate the pileup. We noticed that in this sample the number of tracks used to reconstruct a PV in Fwd and Bwd sample is not the same, which is probably due to the fact that the reconstruction efficiency of the Velo detector is not the same for forward tracks and backward tracks, and most of the tracks in Bwd sample fall into the forward region (LHCb acceptance). When evaluating the reconstruction efficiency, the detector occupancy of the pPb collisions data must be taken into account, as an increase in the event activity compared to simulation means on average a decrease in efficiency. In Fig. 14, the reconstruction&selection efficiency as a function of the number of reconstructed charged tracks (EffTrk), number of VELO clusters (EffVelo), and sum of IT and OT clusters (EffTstation) is given in the pp simulation sample, integrating over the entire D^0 kinematic region used for this analysis $p_{\mathrm{T}} < 10\,\mathrm{GeV}/c$, $2 \lesssim y \lesssim 4.5$. These efficiencies (shown in Fig. 14) are calculated using Eq. 7 in each bin of the detector occupancy variable. In general the distribution can be kinematic dependent, i.e. it is
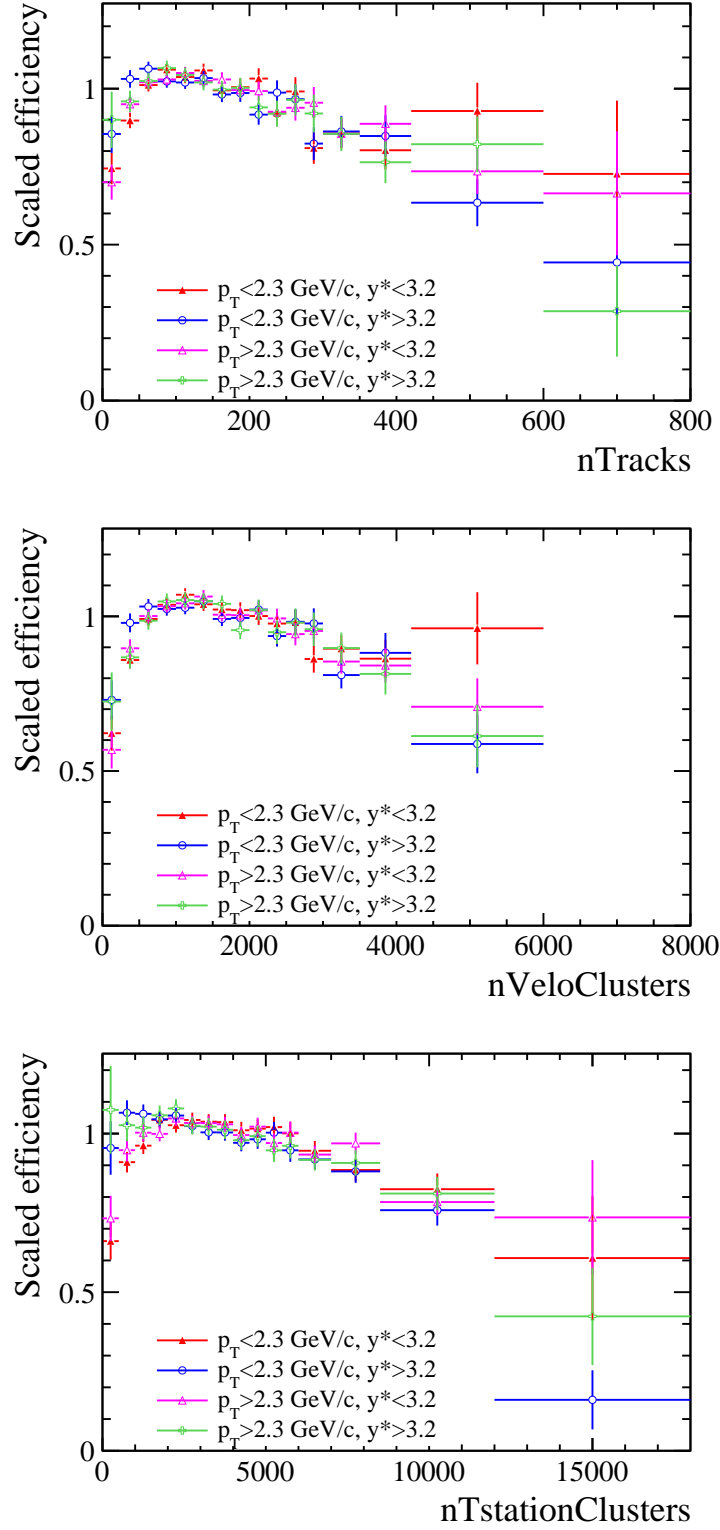
13

Figure 7: The reconstruction&selection (divided by each average efficiency) efficiency in bins of numbers of reconstructed tracks (top), VELO clusters (middle), IT plus OT clusters (bottom), in different D^0 kinematic regions, estimated using pp simulation sample. Statistical uncertainties only.
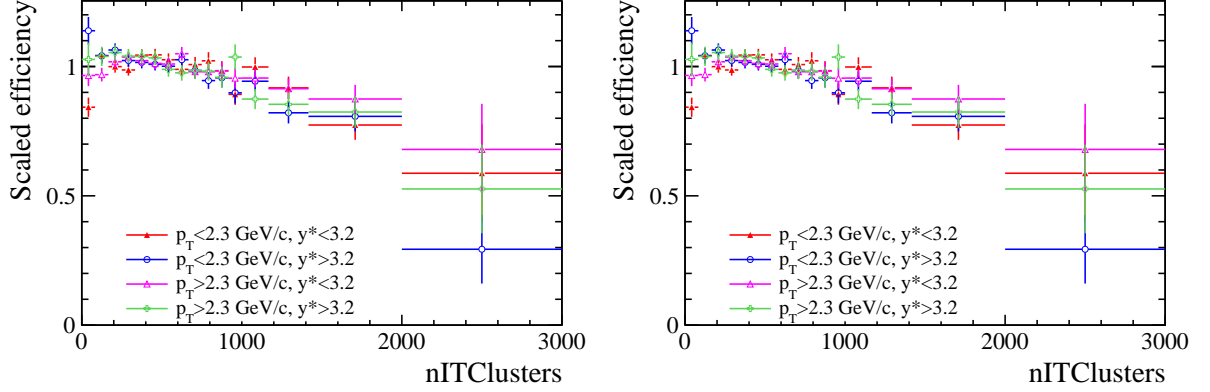
14

Figure 8: The reconstruction&selection (divided by each average efficiency) efficiency in bins of numbers of (left) IT clusters and (right) OT clusters, as estimated from simulation sample.

different in different D^0 p_T and y^* bins, and need to be determined in each kinematic bin of D^0. The distributions of the efficiencies as a function of the variable "x" (e.g. number of tracks, number of velo clusters, etc.) in general can be fitted using Empirical functions with the following form

$$\epsilon(x) = p_3 \times |s(x - p_0)|^{p_1} \times \exp^{-p_2 s(x - p_0)}, \tag{9}$$

where p_3 describes the absolute scale of the efficiency, p_0 roughly reflects the minimum detector occupancy of a D^0 event (including the ability of reconstructing a good quality PV), p_1 describes how fast the increase of efficiency as a function of detector occupancy at small detector occupancy, and p_2 the decrease of efficiency due to increase of detector occupancy. s is a constant scale factor to shift the distribution to a reasonable region (such that the parameters are easier to tune), and is 0.01, 0.001, 0.0005, for EffTrk, EffVelo and EffTstation respectively. For the three distributions of efficiencies (EffTrk, EffVelo and EffTstation), the fitted parameters p_n are given in Table 4; it can be seen that the parameters determined for different categories have similar behaviour in absolute size and relative uncertainty, using the chosen scale factors.

Table 4: Parameters describing the empirical efficiency distribution as function of various detector occupancy for the three detector occupancy variable. The uncertainty is statistical only. Each row corresponds to a plot in Fig. 14.

Distribution	p_0	p_1	p_2	p_3
EffTrk	13.3 ± 0.4	0.138 ± 0.008	0.131 ± 0.007	0.105 ± 0.001
EffVelo	117 ± 1	0.224 ± 0.009	0.176 ± 0.007	0.110 ± 0.001
EffTstation	98 ± 1	0.163 ± 0.009	0.112 ± 0.006	0.102 ± 0.001

The low detector occupancy bins are almost fully dominated by events with only a single reconstructed PV. From Fig. 14 it can be seen that the efficiency is smaller for these
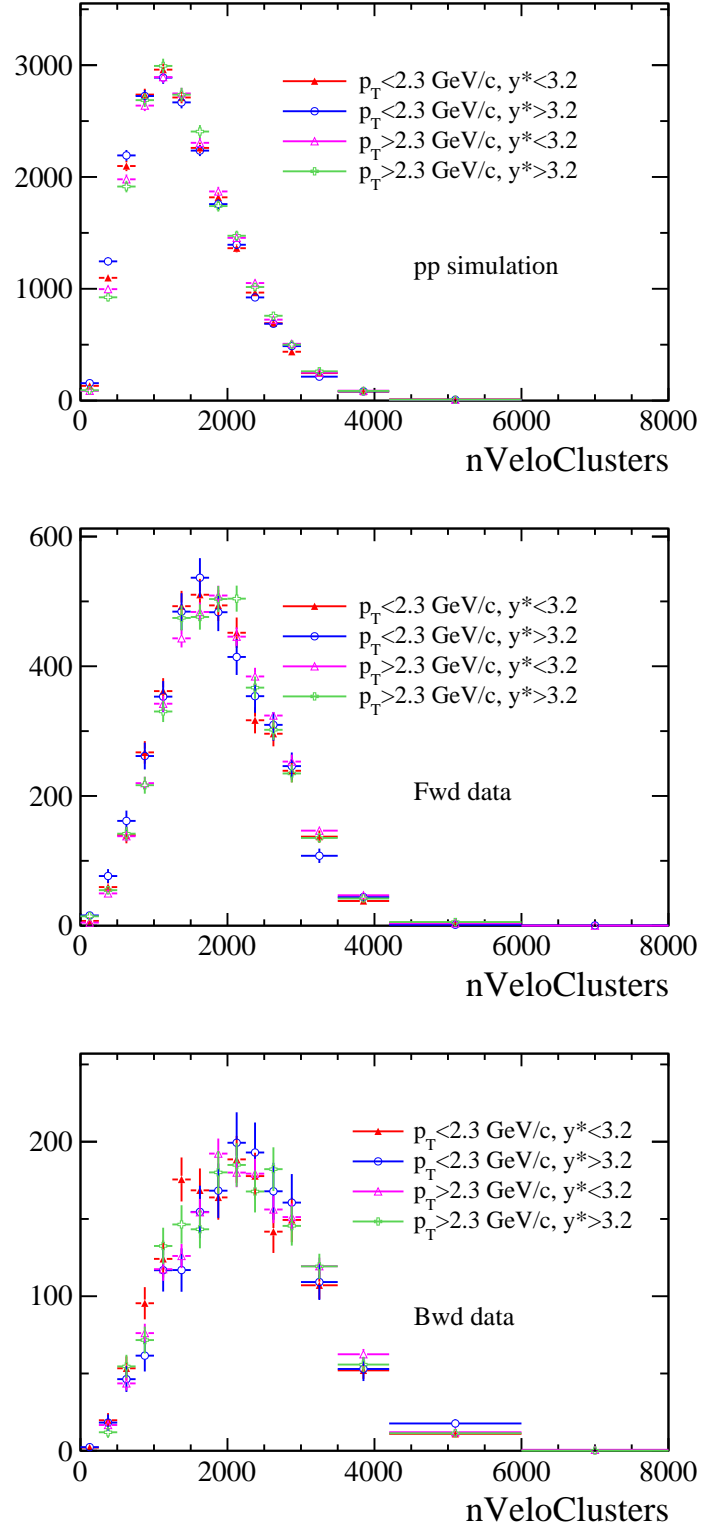
15

Figure 9: The distributions of numbers of VELO clusters in proton-proton MC sample (top), Fwd (middle) and Bwd (bottom) pPb collisions, in different D^0 kinematic regions.
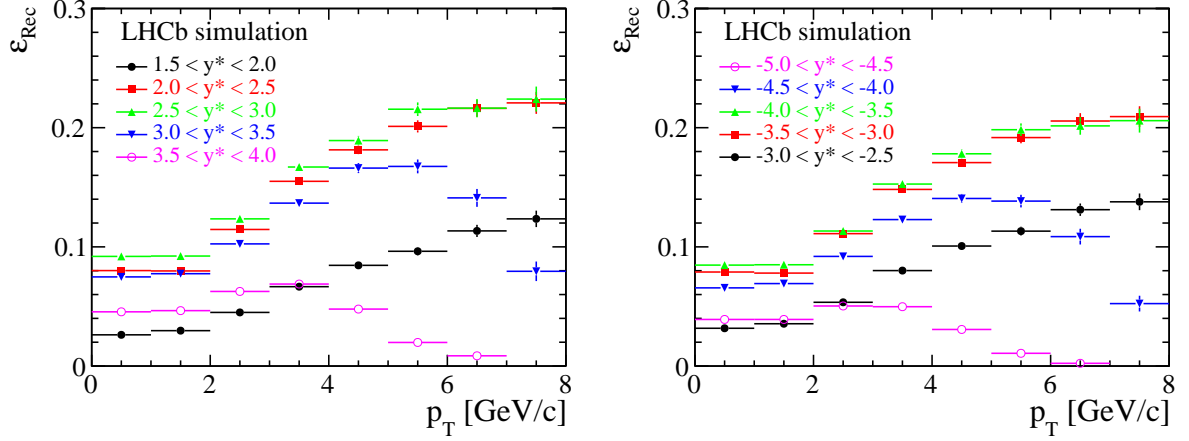
Figure 10: Reconstruction & selection efficiency ϵ_{Rec} calculated using simulated events with event multiplicity distribution from data as a function of p_{T} and y^* of the prompt D^0 for (left) Fwd and (right) Bwd data configuration. Statistical uncertainties only.
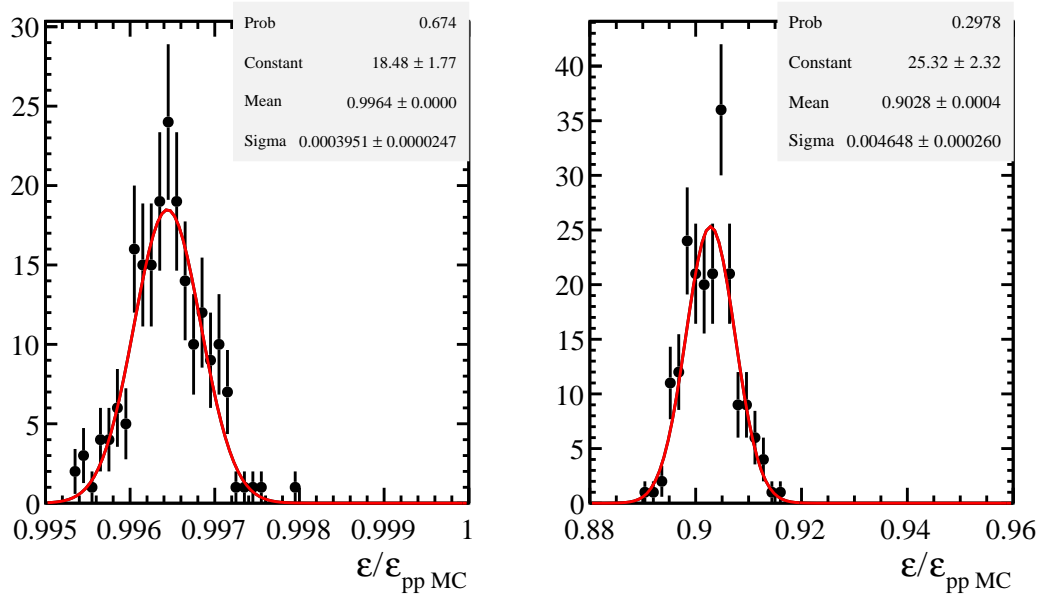
Figure 11: Distribution of reconstruction&selection efficiencies estimated with Bootstrapped data for (left) Fwd and (right) Bwd collision sample, estimated from simulation. The distribution is fitted with a Gaussian function.

events due to poor resolution of primary vertex (PV), which is related to the reconstruction of PV (a PV is required in the selection) in the event. For the low occupancy events, the probability to reconstruct a PV is smaller and the uncertainty (resolution) of the position is large, and thus the PV-related reconstruction and selection (for example χ^2_{IP}

17

Figure 12: Relative efficiency (after correction of detector occupancy) to the one in simulation (before correction of detector occupancy) for Bwd (left) and Fwd (right). The efficiency is determined using the detector occupancy observed in each kinematic bin of D^0 in data. The bin index is defined this way: the first 10 p_T bins correspond to the smallest y bin (in absolute value) with increasing p_T, the second 10 bins correspond to the second smallest y bin as so on.
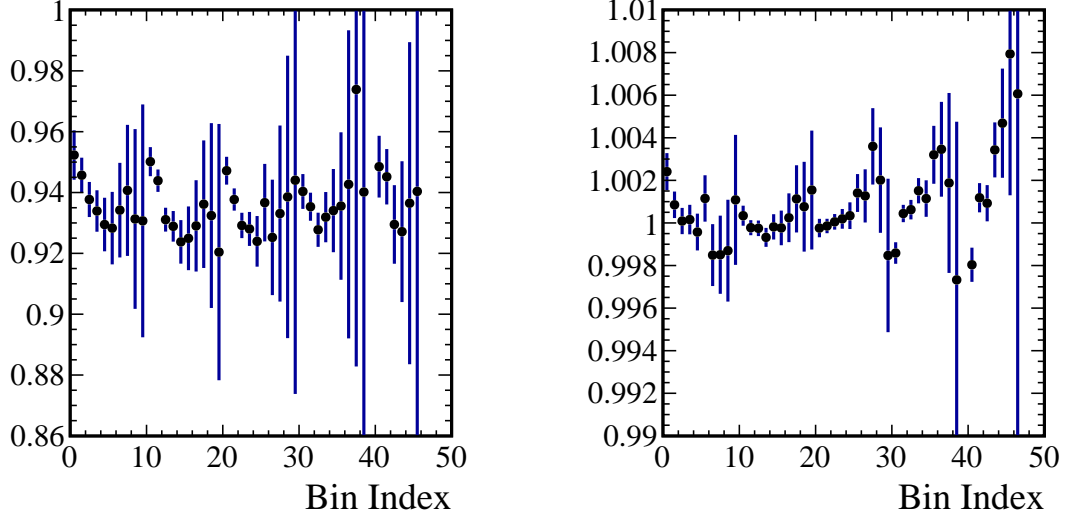
and τ of D^0) have poorer resolution, the separation power of these variables is degraded (see appendix B for more details). For the same reason, the efficiency increases with the increase of detector occupancy.

The low occupancy region doesn't affect pPb data too much as in data the detector occupancy is quite large. The fraction of events containing a signal decay with number of tracks below 30 is less than 1% in the Fwd sample, and is even smaller for the Bwd sample. On the other hand, from Fig. 14 we also see that the efficiency is lower when the detector occupancy is higher. Thus the efficiency estimated with the pp simulation must be corrected to account for the fact that efficiency depends on the multiplicity. There are two ways to include the effect of detector occupancy into the efficiency calculation. In the **first method**, the detector occupancy in simulation is weighted to match data. Practically, when we calculate the reconstruction&selection efficiency according to Eq. 7, in both numerator and denominator each event is given a weight, and the weight brings the detector occupancy distribution in simulation to match data. The weight is function of the detector occupancy, taken as the ratio of the detector occupancy distribution (histogramed) in pPb data over that in simulation (histogramed). The detector occupancy reweighting needs to be done separately for Fwd and Bwd collisions. The **second method** uses detector-occupancy dependent efficiency, i.e. Eq. 9 and combines it with observed distribution of detector occupancy variables in data as

$$\epsilon_{\mathrm{corr}}(p_T, y^*) = \frac{\sum_i w_i}{\sum w_i / \epsilon(x_i | p_T, y^*)}, \tag{10}$$

18
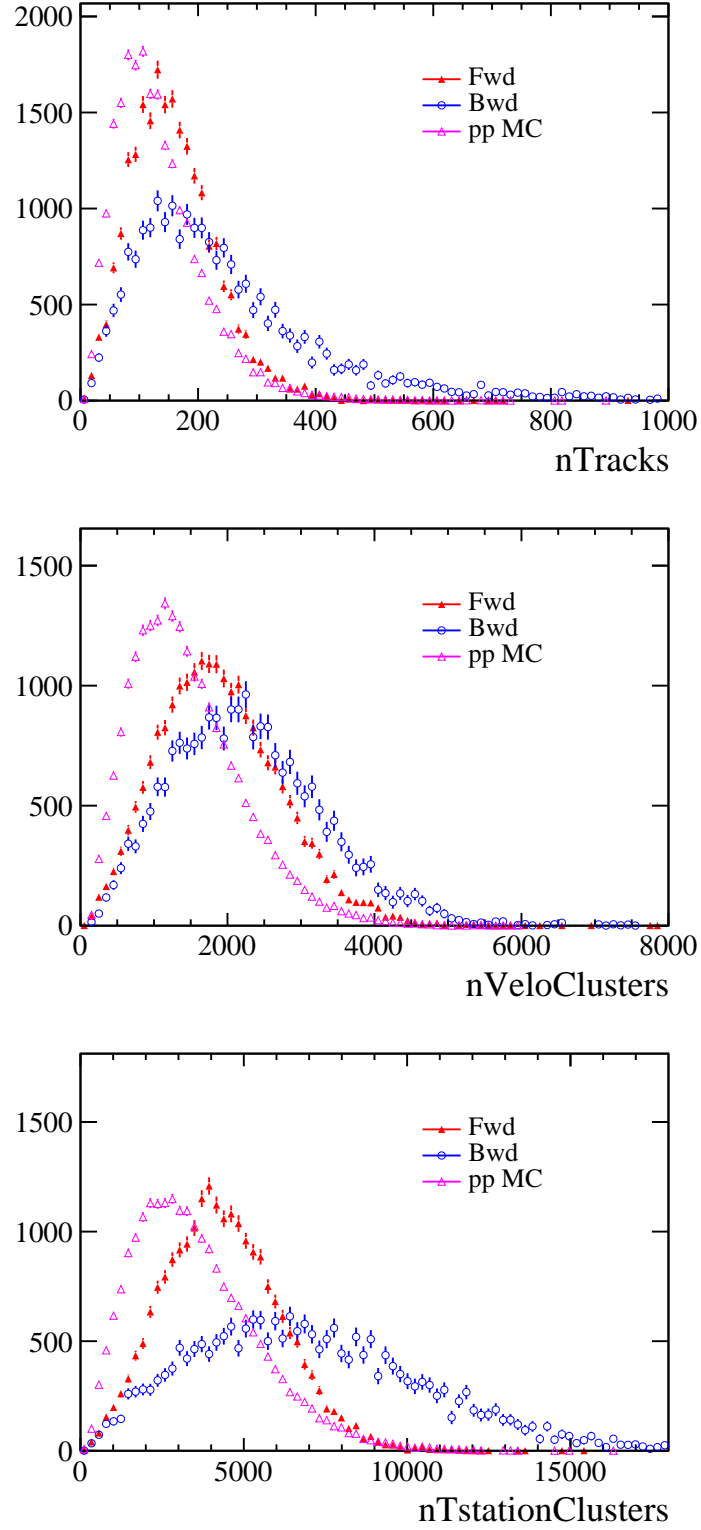
Figure 13: The distributions of numbers of reconstructed tracks (top), VELO clusters (middle), IT plus OT clusters (bottom) in proton-proton MC sample, Fwd and Bwd pPb collisions. pp simulation samples are produced with pileups aiming to reproduce in LHCb 2012 pp data.
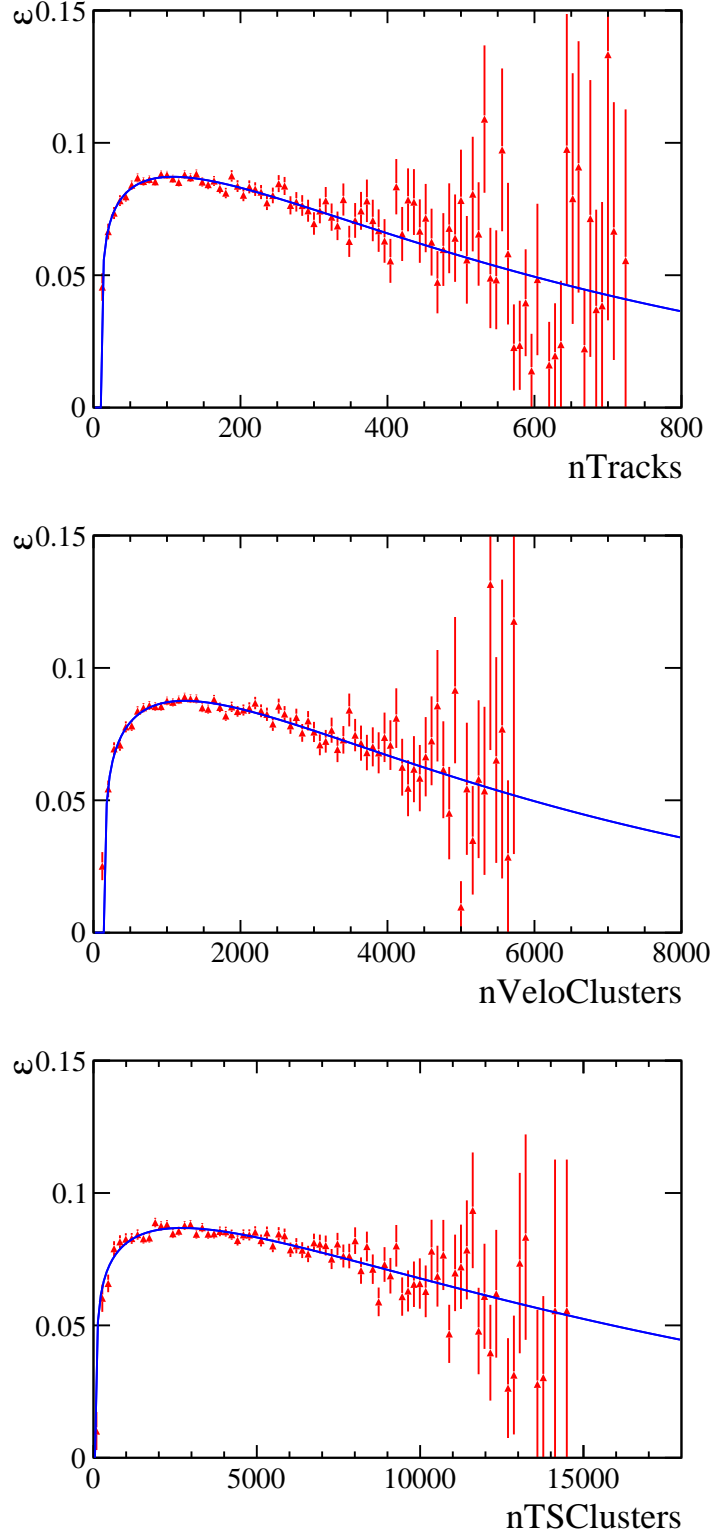
Figure 14: The reconstruction&selection efficiency in bins of numbers of reconstructed tracks (top), VELO clusters (middle), IT plus OT clusters (bottom), estimated using *pp* simulation sample. Statistical uncertainties only. The number of bins is 100 for each plot. The fit is also shown, as described in the text.
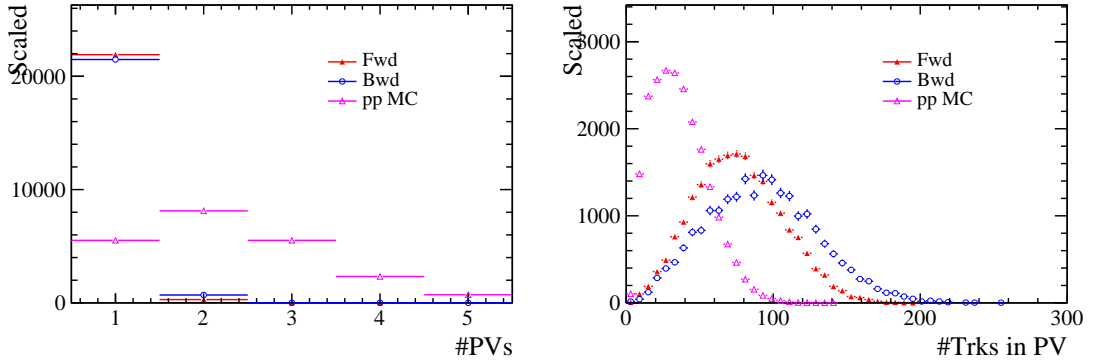
20

Figure 15: The number of (left) reconstructed PVs in simulation, and (right) tracks in the reconstructed PV.

where x_i is the quantity of the detector occupancy variable for the particular event, $\epsilon(x_i|p_\mathrm{T}, y^*)$ is detector-occupancy dependent efficiency (Eq. 9), w_i is the $sWeight$ used to subtract the background and is determined from an invariant mass fit of data in each D^0 (p_T, y^*) bin, and i is the D^0 candidate index; (p_T, y^*) means that we calculate the efficiency in each bin of the D^0.

In the following we will discuss the procedure of the second method to measure the efficiency. In fact both methods have disadvantages: for each D^0 p_T and y^* bin, we need to exploit either the event multiplicity distribution to obtain the weights (for method one) or the efficiency in bins of the detector occupancy distribution (the second method). In reality the precision is quite limited by the statistics of the simulation sample (and also data), especially in large p_T bins and/or high multiplicity regions, where the simulation sample (and data) is not sufficiently large. Fortunately, the shape of the efficiency as a function of the detector occupancy, $\epsilon(x)$, is almost identical in different D^0 kinematic bins. In Fig. 7, the EffTrk, EffVelo, EffTstation in different D^0 kinematic bins are shown. In Fig. 8, the efficiency as a function of TStation clusters is split into number of IT clusters and OT clusters. For the same plot, the efficiency in each kinematic region has been scaled by the inverse of the average efficiency of that region. It can be seen that the distributions overlay with each other closely. There are small discrepancies in smaller event multiplicity bins, but this is less important due to smaller contribution in pPb data in this region, and we will estimate its effect later by studying the variation of the result when the efficiency shape in the four-sub bins as in Fig. 7 are used respectively; the details can be found in section 6.2.1. In summary, we assume that the efficiency factorizes into the dependence on D^0 kinematics (p_T, y^*) and the dependence on detector occupancy, and we treat the deviations from this behaviour when evaluating the systematic uncertainties as described in section 6.2.1. Another useful observation is that distribution of the detector occupancy variable is also "almost" independent of the D^0 kinematics, as can be seen , for instance, in Fig. 9, which reprensents the distributions of number of VELO clusters for pp MC, Fwd and Bwd pPb collisions for different D^0 kinematic bins. Because of these observations, a

21

method is introduced to reduce the statistical effect. Let $\epsilon(x, p_{\mathrm{T}}, y) \equiv f_\epsilon(x)g_\epsilon(p_{\mathrm{T}}, y)$ be the efficiency as a function of the three variables, and $P(x, p_{\mathrm{T}}, y) \equiv A(x)B(p_{\mathrm{T}}, y)$ be the distribution (PDF) of the variables.

Since neither $f_\epsilon(x)$ nor $g_\epsilon(p_{\mathrm{T}}, y)$ are probability distributions, there is a relative normalization factor between the $f_\epsilon(x)$ and $g_\epsilon(p_{\mathrm{T}}, y)$ terms. Thus, they can be redefined as $f_\epsilon(x) \to S \times f_\epsilon(x)$ and $g_\epsilon(p_{\mathrm{T}}, y) \to 1/S \times g_\epsilon(p_{\mathrm{T}}, y)$, where S is an arbitrary factor. On the other hand, both $A(x)$ and $B(p_{\mathrm{T}}, y)$ can be considered as normalized to unity. Since, as mentioned above, the detector occupancy distribution $A(X)$ is assumed to be independent of the kinematics ($B(p_{\mathrm{T}}, y)$), the scale factor S, used to normalize $f_\epsilon(x)$ to unity, implies that $f_\epsilon(x)$ is the same for all kinematic bins (as already stated in the notation of $f_\epsilon(x)$, implying no kinematic dependency). The factorization has been written explicitly in these two equations. Then the efficiency as a function of detector occupancy integrating over the kinematics in a kinematic range Ω is

$$\epsilon(x|\Omega) = \frac{\int_\Omega P(x, p_{\mathrm{T}}, y)\epsilon(x, p_{\mathrm{T}}, y)dp_{\mathrm{T}}dy}{\int_\Omega P(x, p_{\mathrm{T}}, y)dp_{\mathrm{T}}dy} = f_\epsilon(x)\frac{\int_\Omega g_\epsilon(p_{\mathrm{T}}, y)B(p_{\mathrm{T}}, y)dp_{\mathrm{T}}dy}{\int_\Omega B(p_{\mathrm{T}}, y)dp_{\mathrm{T}}dy} \equiv f_\epsilon(x)\times C(\Omega),$$
(11)

where Ω stands for the integrated kinematic range, and $C(\Omega)$ is the average efficiency over the kinematc range Ω and is independent of detector occupancy. Practically, the integral in this equation (and similar ones in the following) is performed by summing over all candidates in the kinematic range Ω and the efficiency $\epsilon(x, p_{\mathrm{T}}, y)$ has to be calculated in bins of $\epsilon(x, p_{\mathrm{T}}, y)$ instead of ideal analytical formula. When deriving this equation, the detector occupancy distribution $A(x)$ cancels as expected. For simplicity we denote $\epsilon(x|\Omega)$ as $\epsilon_\Omega(x)$, which is the efficiency as a function of detector occupancy in the kinematic range Ω. Integrating again over the detector occupancy variables we have the average efficiency in the kinematic range Ω,

$$\overline{\epsilon}(\Omega, A) = \int A(x)\epsilon_\Omega(x)dx = \int A(x)f_\epsilon(x)C(\Omega)dx = C(\Omega)\int A(x)f_\epsilon(x)dx.$$
(12)

Note that in this equation, the average efficiency depends on the detector occupancy distribution, $A(x)$. Equivalently (and done in practice), for data $\overline{\epsilon}(\Omega, A)$ could be determined with Eq. 10 with the background subtraction implemented automatically. Following Eq. 12 we have the following equation for two different detector occupancy distributions, $A(x), A'(x)$

$$\frac{\overline{\epsilon}(p_{\mathrm{T}}, y, A)}{\overline{\epsilon}(p_{\mathrm{T}}, y, A')} = \frac{\overline{\epsilon}(\mathrm{ALL}, A)}{\overline{\epsilon}(\mathrm{ALL}, A')} = \frac{\int A(x)f_\epsilon(x)dx}{\int A'(x)f_\epsilon(x)dx}$$
(13)

If we consiser $A(x)$ as the detector occupancy distribution in data while $A'(x)$ in simulation, this equation describe the relative efficiency in data over that in simulation, and the relative efficiency is independent of kinematic bins (and kinematic distributions). $\overline{\epsilon}(p_{\mathrm{T}}, y, A')$ is equivalently just the efficiency calculated directly using the simulations sample, i.e. by counting the fraction of events passing the reconstruction&selection conditions without considering the multiplicity, which is automatically taken into account. In the end we can calculate the relative scale factor $\frac{\int A(x)f_\epsilon(x)dx}{\int A'(x)f_\epsilon(x)dx}$ combining all kinematic bins, and use it

to scale the raw efficiency calculated in simulation in each correponding kinematic bin, $\bar{\epsilon}(p_{\mathrm{T}}, y, A')$, determining the detector occupancy corrected efficiency $\bar{\epsilon}(p_{\mathrm{T}}, y, A)$. The basic idea is that the efficiency factorizes into two parts, that dependent on detector occupancy and that on D^0 kinematics and the first part is very similar in different kinematic region, so the decrease of the relative efficiency due to higher detector occupancy is the same in different kinematic bins. We can see from Eq.13 that the normaliztion factor of $f_\epsilon(x)$ cancels, confirming we could use arbitrary normalization for $f_\epsilon(x)$.

In summary , (1) we calculate the efficiency in bins of detector occupancy $f_\epsilon(x)$ combining all kinematic bins to increase the statistics (2) fit the efficiency $f_\epsilon(x)$ with an empirical function (3) determine the detector occupancy distribution in Fwd and Bwd pPb data samples respectively (4) calculate the detector occupancy averaged distribution using Eq.12 (5) calculate the raw efficiency in simulation using the counting method as in Eq.7 for the global kinematic bin as in step (1) and for each kinematic bin of D^0 mesons (6) scale the raw efficiency in each kinematic bin determined in (5) by the ratio of efficiencies in (1) and (5) for the global kinematic bin. The advantage of combining different kinematic bins is to reduce the statistial uncertainty. To be more general, if we see discrepancies of detector occupancy distribution or efficiency as a function of detector occupancy across a large kinematic phase space, we could merge smaller kinematic region (neighbouring bins) to perform these steps.

In practice, the three detector occupancy variables (number of VeloClusters, number of Tracks, number of T-station clusters) are given as references of detector occupancy, and their average result is used. The spread between the results using three different detector occupancy variables is $< 0.3\%$ for Fwd collision, and 2% for Bwd collision. The reconstruction&selection efficiency determined this way (i.e. when taking the particle multiplicity in data into account) over that of raw efficiency (without considering the detector occupancy in data) determined from simulation is 1.000 for Fwd collision, and 0.936 for Bwd collision, and are considered to be the same over all kinematic bins.

As said earlier the detector occupancy distributions $A(x)$ are similar in different D^0 (p_{T}, y^*) bins as observed in pPb data, while the remaining small difference could have some effect on the efficiency. The size of the effect is estimated by artificially introducing an increase to the detector occupancy by 10% (the detector multiplicity value of each event multiplied by 1.1), and the relative change of the efficiency is found to be 2% (1%) for the Bwd (Fwd) sample. In the default result, the detector occupancy distribution in data is obtained integrating over p_{T}, y^* bins, to increase the statistics. Alternatively, we could use the detector occupancy distribution in each $D^0, y*$ bin to determine the result, separately. The result with respect to those directly determined from simulation (before reweigting detector occupancy) is shown in Fig. 12. In the nominal result, it is a flat distribution, since a single factor is used to scale the simulation efficiency. However we can see the efficiency in Fig. 12 has a small dependence on D^0 p_{T} i.e. efficiency decreases with increasing p_{T}, but the effect is negligible on y. For Fwd sample, the variation is about 0.2% compared to the avarage, while for Bwd sample it is about 1%, which is considered as systematic uncertainty, as discussed in section 6.2.1.

There are two **uncertainties** coming from limited statistics. The first one is the

uncertainty of the average efficiency determined from simulation sample, $\bar{\epsilon}(p_{\mathrm{T}}, y^*)$, which is related to the simulation sample size in each (p_{T}, y^*) bin; it comes naturally when it is determined with the simulation sample of limited statistics. The other one is the fluctuation of detector occupancy distribution in data, which is related to data sample size. Both sources are treated as systematic uncertainties. The former one is (p_{T}, y^*) bin dependent, and the latter one is the same for all bins. The latter one is estimated using Bootstrap method to study the variations of the efficiencies: we generate toy MC samples by drawing events from the original data sample allowing repetition of events, and for each sample we recalculate the efficiency. The variation of the efficiency among the toy samples is relatively below 0.1% for both Bwd and Fwd samples as seen from the width of the distribution in Fig. 11, which plots the distributions of efficiencies in the toys divided by the raw efficiency from simulation.

In Fig. 10, the reconstruction&selection efficiency in each p_{T} and y^* bin for the prompt D^0 meson is shown for Fwd and Bwd configuration, and is summarized in Tables 14 and 15 in appendix A. The lower efficiency in high p_{T} large y bins is due to the requirement on momentum of the final state hadrons in the stripping $p < 100\,\mathrm{GeV}/c$.

5.3 Particle identification efficiency

The PID efficiency ϵ_{PID} is defined as the efficiency of the PID requirement on the two hadron tracks in the D^0 selection. The ϵ_{PID} is determined using the single track efficiency in data convolved with the track kinematic distribution in simulation (track calibration method) in any particular D^0 kinematic bin according to the formula

$$\epsilon_{\text{PID}} = \frac{\sum_i^N \epsilon_K(p_i^K, \eta_i^K)\epsilon_\pi(p_i^\pi, \eta_i^\pi)}{N}. \tag{14}$$

where N is the sum of the events in the simulation sample used to evaluate the PID. The single track efficiency $\epsilon_{K,\pi}(p, \eta)$ is determined using tag and probe method with a PID unbiased D^0 sample in the data taken in the same pPb period. The D^0 sample is $D^*(2010)+$ tagged, the detailed selections of this sample in the stripping is given in appendix C. One of the main reasons of the restripping the pPb data is to remove the p_{T} threshold requirement on the D^0 particle required in previous version of the stripping ($p_{\text{T}}(D^0) > 2\,\text{GeV}/c$), and this keeps more low-p_{T} tracks ($p_{\text{T}} \lesssim 1\,\text{GeV}$) which are important to calibrate the low-p_{T} bins of D^0. At the same time, the prescale of the PID calibration line is increased from 0.89 to 1.

There is an overlap between the calibration sample and the analysis D^0 sample, however since the D^0 in the calibration corresponds to only feeddown production of D^0, the overlap is not large. The detector occupancy, which the single track efficiency depends on, is also similar in the analysis sample and calibration sample, so we integrate over the detector occupancy and bin the efficiency only in (p, η) of the tracks. The calibration sample for Fwd and Bwd collisions are analyzed separately.

The single track efficiency for K calculated with the tag (π) and probe (K) method is defined as

$$\epsilon_K(p_K, \eta_K) = \frac{\text{\# signal } D^0 \text{ with both } K, \pi \text{ PID applied}}{\text{\# signal } D^0 \text{ with } \pi \text{ PID applied}}(p, \eta_K). \tag{15}$$

The efficiency for the π is determined in the same way, by swapping K with π in equation 15. To subtract the background events, fit to D^0 invariant mass is performed in the same way as the one for signal extraction of this analysis (see section 4). Tight PID cuts have been applied to the tag track to further suppress the background.

In Fig. 16, the single track PID efficiencies are shown in bins of (p, η) for the kaon and pion for both Fwd and Bwd pPb collisions. Taking the pion and kaon single track efficiencies, and the kinematics from simulation, the PID efficiency in each D^0 (p_{T}, y^*) is calculated, using Eq. 14.

There is an alternative method to calculate the PID in each D^0 (p_{T}, y^*) bin, by directly using the PID efficiency of the D^0 in the calibration sample, applying the PID cuts in the analysis sample on the two tracks (direct method). The efficiency in this case is defined as the fraction of D^0 signals with both tracks fulfilling the PID requirements. Although in the restripping, the p_{T} threshold is removed, due to the selection of additional soft pion, the p_{T} spectrum of the D^0 in the calibration sample is limited to $p_{\text{T}}(D^0) > 1\,\text{GeV}/c$.
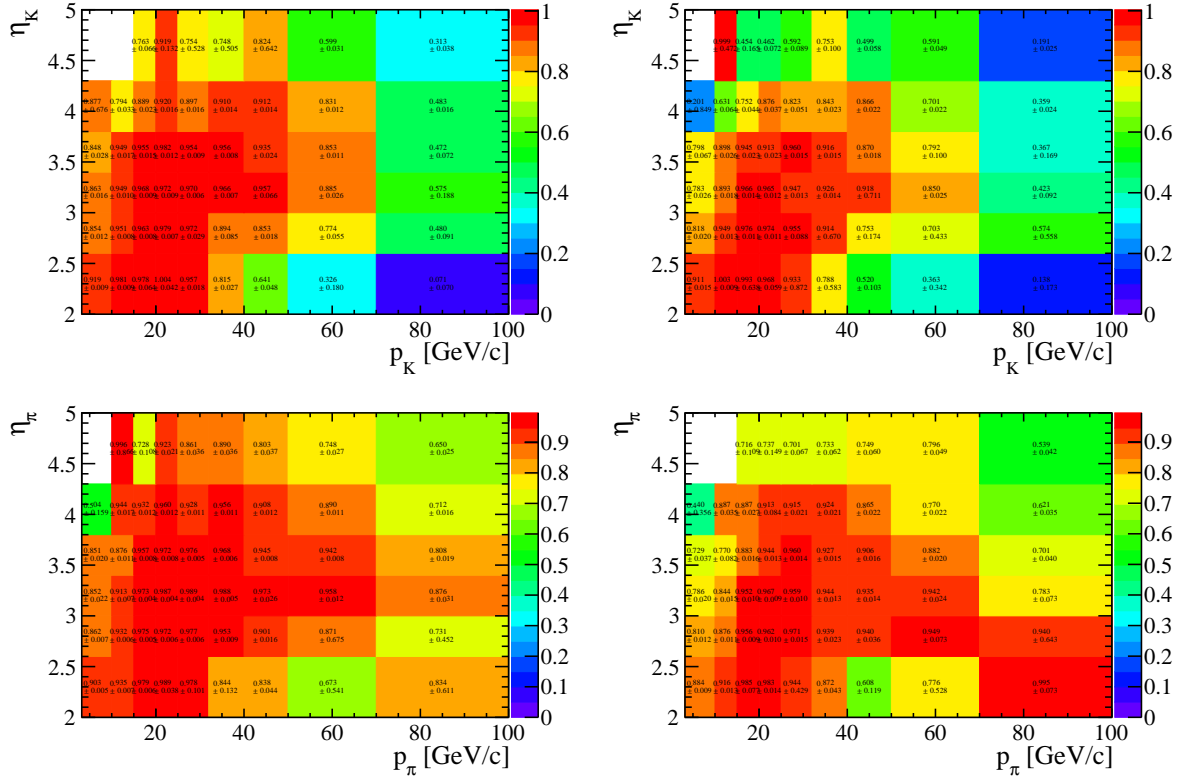
Figure 16: Single track PID efficiency for (top) kaon and (bottom) pion in bins of track (p, η) in the (left) Fwd and (right) Bwd pPb collisions. Statistical uncertainties only.

So the second method could only be done for the bins $p_{\mathrm{T}}(D^0) > 1\,\mathrm{GeV}/c$. This method gives consistent results compared to the results of calibration using tracks. (see 6.2.2 for discussions). The two methods are both studied: for each kinematic bin we use both methods to calculate the PID efficiency and their corresponding systematic uncertainties, and we take the value that has smaller total uncertainty. The result suggests that, for most of bins the track calibration method is the default one, while for a few high statistics bins (where other systematic effect is large for the track method), the direct method is selected.

In Fig. 17, the resulting PID efficiency in each p_{T} and y^* bin for the prompt D^0 meson is shown for Fwd and Bwd configuration, and is summarized in Tables 16 and 17 in appendix A.

5.4   Total efficiency

The total efficiency ϵ_{tot}, i.e. the product the geometrical acceptance efficiency, the reconstruction selection efficiency and the PID efficiency, is given in Figs. 18 and 19, and is summarized in appendix A. The efficiency in the Bwd configuration is smaller compared to that in the Fwd configuration, which is due to smaller reconstruction efficiency and

26
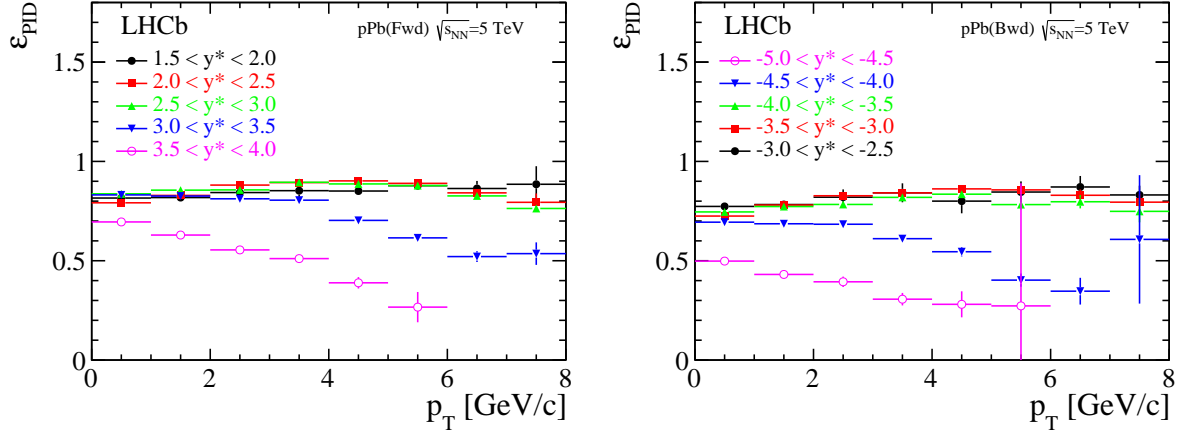
Figure 17: Calibrated particle identification efficiency ϵ_{PID} in bins of D^0 p_T and y^*, calculated using single track efficiencies, determined from calibration real data. Statistical uncertainties and systematic uncertainty added in quadrature.

Figure 18: Total efficiency as a function of p_T and y^* of the prompt D^0 for (left) Fwd and (right) Bwd configuration. The missing bins above p_T=7 GeV/c in the highest rapidity bin are due to the upper cut on the momentum of the pions and kaons (see Table 1). The efficiency in the Bwd sample is smaller, which is due to smaller reconstruction efficiency and PID efficiency as a result of higher detector occupancy. Statistical uncertainties and the PID systematic uncertainties added in quadrature.
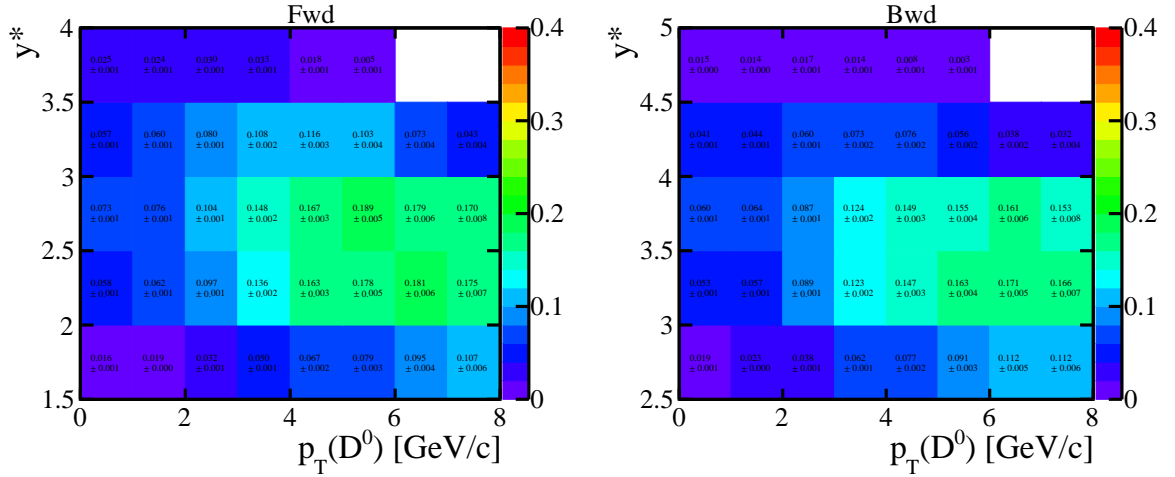
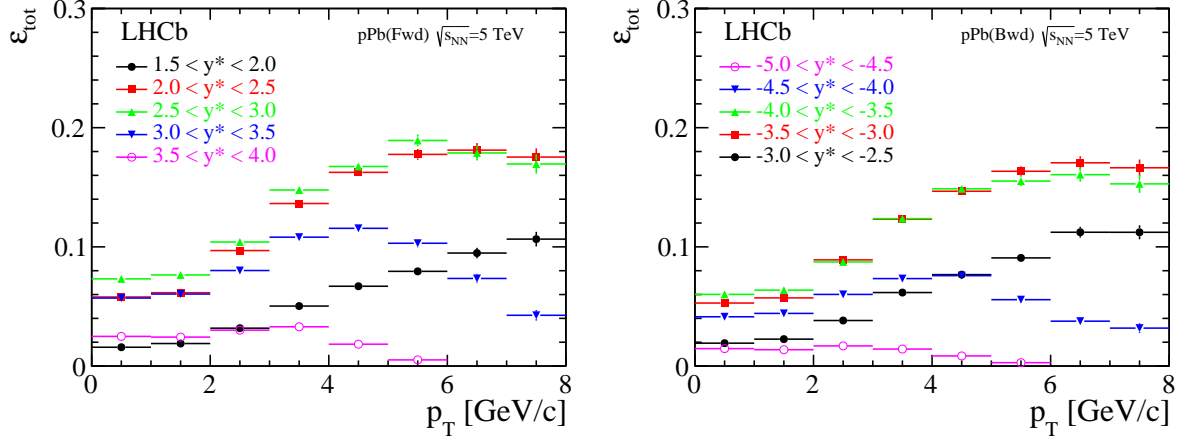517   PID efficiency as a result of higher detector occupancy.

27

Figure 19: Total efficiency as a function of p_T and y^* of the prompt D^0 for (left) Fwd and (right) Bwd configuration. Statistical uncertainties and the PID systematic uncertainties added in quadrature.

6 Systematic uncertainties

The systematic uncertainties are evaluated separately for the Fwd and Bwd sample, due to very different environment in the two collisions, if no other specified.

6.1 Signal yield systematic uncertainty

For the analysis, the signals are produced promptly, and those coming from b-hadron decays are removed by the fit to the $\log \chi^2_{\text{IP}}(D^0)$ variable as shown in Fig. 3 and 4. In general the $\log \chi^2_{\text{IP}}(D^0)$ distributions of prompt D^0 and $D^0-$from$-b$ are well described by the fit. The uncertainty of the fitted prompt fraction is a source of systematic effects. Other systematic effects concerning the fit to $\log \chi^2_{\text{IP}}(D^0)$ include the uncertainties of fixed parameters ρ_L, ρ_R, ϵ and background shape. For the Bwd sample, additional uncertainties are considered since the shape for the $D^0-$from$-b$ component is also fixed. The effects of ρ_L, ρ_R, ϵ is studied by varying these parameters in the ranges that are observed in simulation. For the background shape effect, we choose a different sideband window which is close to signal window to determine its distribution. The uncertainty on the $D^0-$from$-b$ shape in the Bwd fit is also studied by changing the parameters governing the shape within the range observed. These effects are studied one by one and are added together taking into account their correlations. These effects are considered to be fully correlated between the Fwd and Bwd results. In Fig. 20, the relative systematic uncertainty to the value of prompt D^0 fraction is shown summing over all these effects. As can been seen, it ranges between 0 and 5% and it is on average about 2% for the Fwd sample and 1.5% for the Bwd sample.

The signal yield systematic uncertainty related to the invariant mass fit is studied by using alternative models to perform the fit. For the signal component, we vary the
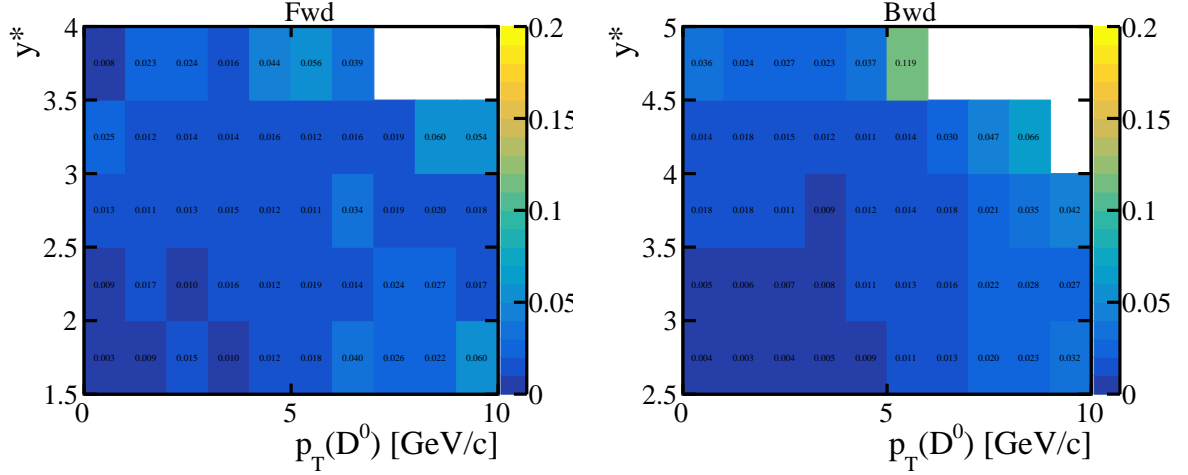
28

Figure 20: Relative Systematic uncertainty of prompt D^0 fraction in bins of p_T and y^* as determined from data. The empty bins correspond to no events in that region.

parameters that have been fixed during the fit. There is one particular case, fitting to simulated sample shows that sometimes the Gaussian and the CB component swap, i.e. their relative fraction and width swap, and as a result of the a parameter in the CB function. This swapped shape is also used to performed the fit. For the background, an exponential function is used as an alternative. We also performed the fit in a different mass window. In the end these effects are added in quadrature to give the final systematic uncertainty. The resulting systematic uncertainty in different kinematic bins is shown in Fig. 21. The result shows that the signal yield is quite stable with respect to these variations: for most of the bins the systematic uncertainty is below 1%, and a few percent for high background (low statistics) bins.

The stability of the signal models used in the fit is also studied using toy MC method. We combine the signal sample in simulation with artificially generated background linearly distributed in the mass window we fit. Then we perform invariant mass fit using exactly the same model as for data. The fit could always recover the correct yield of signal events in the toy sample, with a precision of 0.4% with average background level seen on data.

6.2 Efficiencies

6.2.1 Tracking and occupancy efficiency

As said earlier, the **tracking efficiency** in simulation is corrected using the table provided by the tracking group, which accounts for the difference of tracking efficiency in data and simulation. The uncertainties from the correction factors themselves in the table are negligible. The tracking efficiency difference in data/MC is studied with muons. An additional uncertainty of 1.1% (1.4%) is assigned to the $K(\pi)$ due to the hadronic interactions of these particles with the detector. This uncertainty is dominated by the
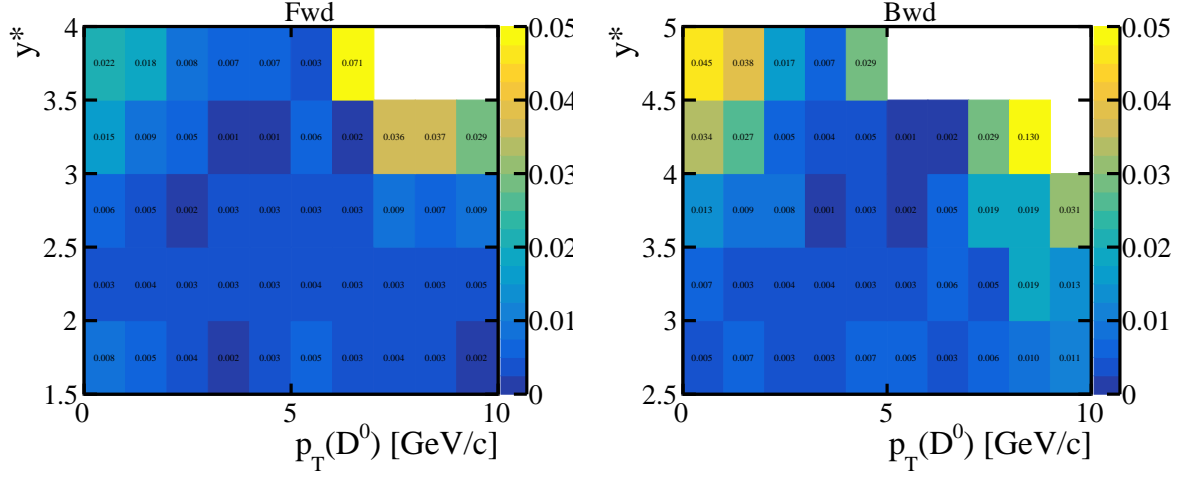
Figure 21: Relative systematic uncertainty related to invariant mass fit in bins of p_T and y^*. The empty bins correspond to no events in that region.

uncertainty on the material budget and hence full correlation between kaons and pions is assumed, yielding a total uncertainty of 2.5%.

The **efficiency as a function of the detector occupancy** variable is an important input from the simulation for this analysis. Due to limited statistics, especially in the high multiplicity regions, there is an uncertainty concerning the fit to the efficiency distribution, reflected by the uncertainties of the parameters in Table 4. To study this effect, we change the parameters one-by-one by 1σ, and study the variation of the efficiencies. It is found that the parameter that affect the efficiency mostly is p_2, which describe the slope of the drop in efficiency in high multiplicity regions. The efficiency variation due to p_2 is 1% (2%) for Fwd (Bwd) sample, and is quite below 1% for the other parameters. The systematic uncertainties estimated this way for each of the three detector occupancy variables are also consistent between each other.

As described in section 5.2, the choice of detector occupancy variable have an effect of $< 0.6\%$ (2%) on the efficiency for Fwd (Bwd) sample, and the numbers are quoted as systematic uncertainty. The variation of the detector occupancy distribution in data is another source of uncertainty to the efficiency, and is studied by comparing the efficiency obtained using the detector occupancy variable distribution in each bin, and the variation is estimated to be $< 0.2\%$ (1%) for the Fwd (Bwd) sample (see Fig. 12).

When obtaining the efficiency as a function of the detector occupancy, we integrate over all D^0 kinematic bins to increase the statistics, and assume the shape as a function of detector occupancy is independent of the kinematics. This is a good assumption for mid and high multiplicity bins, but there seems to be some discrepancy in low event multiplicity bins as can be seen from Fig. 7. To estimate the effect, we repeat the efficiency calculation using the event-multiplicity-dependent efficiency $\epsilon(x)$ (Eq. 9) determined in the four kinematic sub-bins as shown in Fig. 7, independently. As a result we get four

30

efficiencies, the largest variation among the four results is 1.4% (3.1%) for the Fwd (Bwd) collision, averaged over the three detector occupancy variables, and is quoted as systematic uncertainty. It should be noted that this estimation double counts some of the statistical fluctuation, due to the independence of different kinematic bins.

In summary, the efficiency is affected by the imperfect modelling of tracking efficiency by simulation (2.5%), the limited statistics in simulation to determine the efficiency as a function of the detector occupancy variable especially in high multiplicity region (1%, 2%), the choice of detector occupancy variable to represent detector occupancy (0.6%, 2%), the uncertainty of the detector occupancy distribution estimated in data (0.2%, 1%), and the dependence of the shape of the efficiency on the D^0 kinematics (1.4%, 3.1%). These effects are due to different mechanism, but the methods of estimating them have some kind of positive dependence (and thus double counting). For example, the choice of detector occupancy variable and the one due to limited statistics. However it is difficult to determine quantitatively the double counted value, so conservatively, we add them quadratically to assign a systematic uncertainty, yielding 3% and 5% for the Fwd and Bwd collision sample respectively.

6.2.2 PID Efficiency

Two methods have been used in complementary to determined the PID selection efficiency. In the track calibration method, the PID efficiency is calculated as the K^-, π^+ single track efficiencies convoluted with the kinematics from simulation, in each D^0 (p_T, y^*) bin. The single tracks efficiency is determined using a calibration D^0 sample. In the direct method, the PID efficiency in each (p_T, y^*) bin on the calibration sample is calculated by counting the percentage of D^0 signals with both tracks passing the PID requirement in the calibration sample.

For the direct method, the uncertainty of the efficiency estimated in each bin is a systematic effect. It is a statistical uncertainty in origin due to the sample size of the calibration sample, and this one reduces when we determine the total cross-section integrating over D^0 bins. The other systematic effect is from the background subtraction, which is studied by investigating the change of the results when sideband subtraction is used for background subtraction instead of the nominal one, which is the invariant mass fit method. The effect is found to be $< 1\%$ for most of the kinematic bins.

Concerning the track calibration method there are three main sources of systematic effects, the one due to limited statistics in the calibration sample, the one due to the binning scheme when determining the single track efficiency, and the one related to the determination of the single track efficiency (i.e. background subtraction). We will discuss these effects in details below.

The one due to limited statistics in the calibration sample is intrinsically related to the number of calibration tracks and is studied with a toy MC method; we fluctuate the single track efficiency in each (p, η) bin independently according to a Gaussian function, with mean, sigma as its nominal value and uncertainty respectively, and study the variation of the result PID efficiency. By repeating the process many times, we determine a collective set

of new PID efficiencies, and the spread among these new efficiencies is taken as systematic uncertainty. Practically for each D^0 (p_T, y^*) bin the result efficiency distribution is fitted with a Gaussian function, and the width of the Gaussian is quoted as systematic. The relative systematic of this source is given in Fig. 23 for each (p_T, y^*) bin for the Fwd and Bwd collision sample respectively. The relative uncertainty is about 1% in the middle kinematic bins, while up to 10% in boundary bins, which is expected to be due to fewer corresponding tracks in the calibration sample.

The one due to the binning scheme is studied by utilizing alternative binning scheme for the single track efficiency. Compared to the nominal binning scheme of 9 p bins and 6 η bins, we use more p bins (14) less η bins (4) or less p bins (6) bins and more η bins (9). New efficiencies are calculated with these two new binning scheme, and the deviation from nominal ones are considered as systematic uncertainty. It is found that in most of the cases, the efficiency is sensitive to only one of the two variations, except for the middle kinematic region, where both are sensitive and small. So we add in quadrature the sum of the variations as the systematic uncertainty of this source. The relative systematic uncertainty is given in Fig. 24 for each (p_T, y^*) bin for the Fwd and Bwd collision sample respectively

When calculating the single track efficiency, the number of D^0 signals in the calibration sample before/after the PID requirements are determined by the invariant mass fit. The quality of the invariant mass fit introduces a systematic uncertainty related to the single track efficiencies. Although the same signal and background models to the ones adopted in the analysis are used to perform the fit, the true invariant mass distribution could be different due to quite different selection criteria. To study the effect, as an alternative, we using sideband subtraction to determine the signal yield. The final effect on the calibrated D^0 PID selection efficiency is $< 1\%$ relatively, and found to be almost uniform across all kinematic regions and is similar for Fwd and Bwd collision result.

The total PID systematic uncertainty in the track calibration method is a quadratic sum of these three sources, and the result is given in Fig. 25. The values are $1-2\%$ for mid rapidity bins, while for high p_T, y^* bins the uncertainty is almost 100 percent, indicating lower measurement power in these bins. As a result we exclude the bins $5 < p_T < 10\,\mathrm{GeV}/c$, in the last rapidity bin and $8 < p_T < 10\,\mathrm{GeV}$ in the third y^* bin; this is also consistent with the observation of the almost zero fitted signal yield in these bins.

The two methods are compared in the common range $p_T > 1\,\mathrm{GeV}/c$, as shown in Fig. 26, which gives their pull distribution and the bin-bin difference, considering the respective systematic uncertainties. The pull distributions are fitted with Gaussian functions. If the two estimations are consistent, we should see a pull with mean and sigma consistent with zero and one respectively. While the mean has a value very consistent with zero, the sigma is around 20% larger than unity (with also about 20% uncertainty), which means that the systematic uncertainty are underestimated, so we scale the systematic uncertainty by 20% to take this into account.
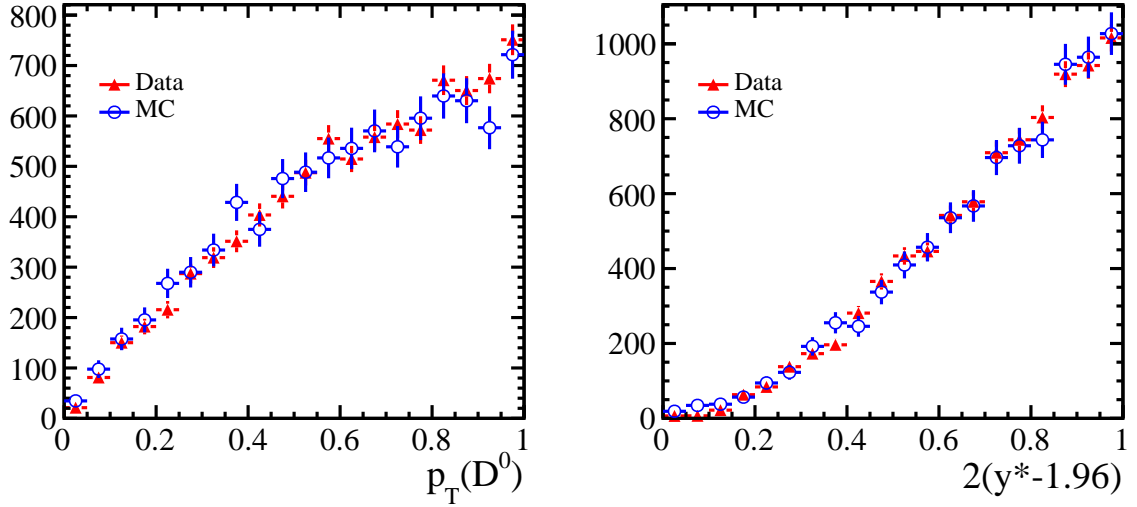
Figure 22: Comparison of (left) p_{T} and (right) y^* distributions between data and simulation for the most soft bin $0 < p_{\mathrm{T}} < 1\,\mathrm{GeV}$, $1.5 < y^* < 2$.

6.3 Kinematic distributions

Since the efficiencies depends on D^0 kinematic distributions, any discrepancy between data and simulation in D^0 $p_{\mathrm{T}} - y^*$ distributions will result in bias of efficiency. However since we make differential cross-section measurements and efficiencies are calculated in small bins of $p_{\mathrm{T}} - y^*$, the effect, if any, is significantly reduced. In particularly we also checked that within each each small bin of p_{T} and y^*, the p_{T} and y^* distributions in data are very well simulated in the simulation as can been seen in Fig. 22 for a bin which could mostly be affected (efficiency varies most strongly within that bin). In the end the effect is found to be negligible.

6.4 Other systematic uncertainties

The relative uncertainty of the corresponding luminosity is 1.86% (2.13%) for the Fwd (Bwd) data sample. The uncertainty of the branching fraction $\mathcal{B}(D^0 \to K^-\pi^+)$ is 1%. The limited statistics in the simulation sample introduces uncertainties to the efficiencies and is then propagated to the cross section measurements, which is negligible for mid kinematic bins, but is quite large in acceptance boundaries bins.

6.5 Summary of systematic uncertainties

The systematic uncertainties are summarized in Table 5 and shown in Fig. 27 bin by bin.
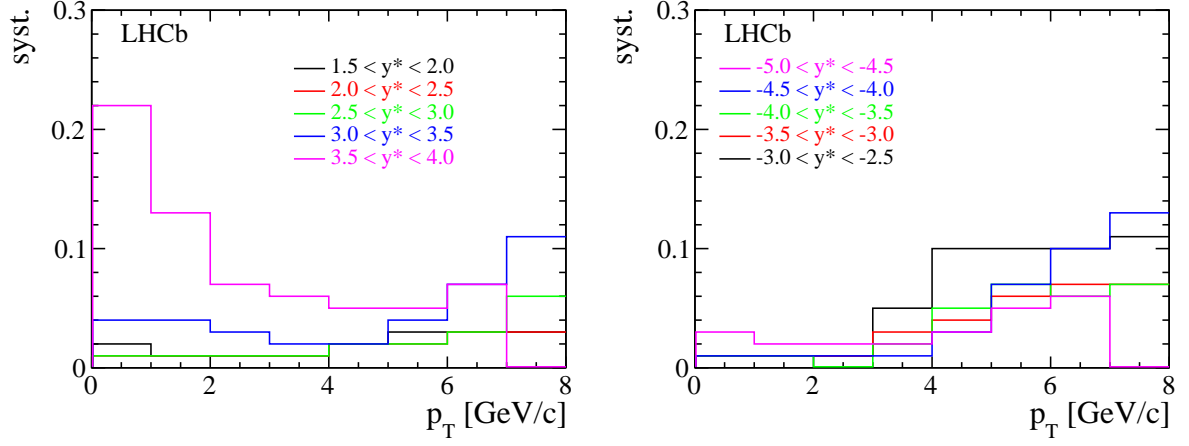
Figure 23: The relative PID efficiency systematic uncertainty, due to fluctuation of single track PID efficiency, in each (p_{T}, y^*) bin for the (left) Fwd and (right) Bwd sample.
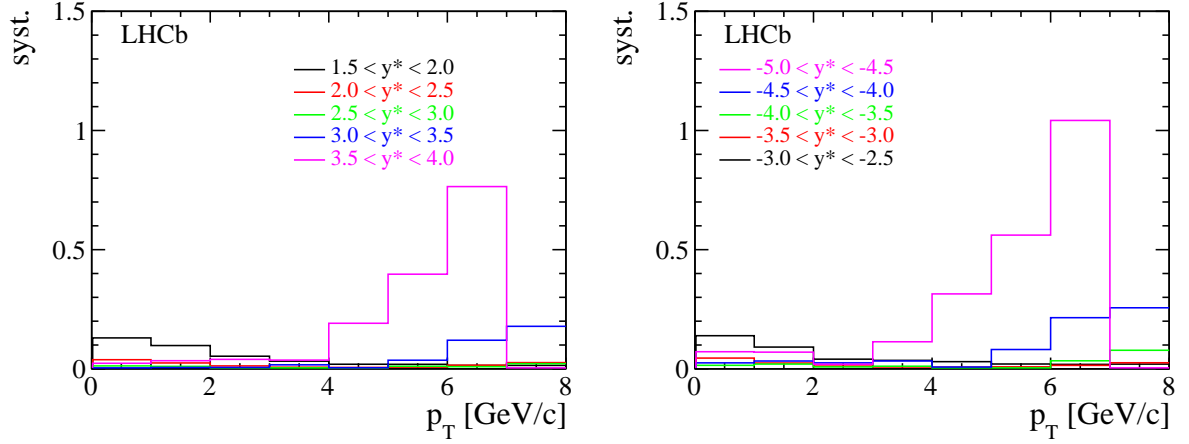
Figure 24: The relative PID efficiency systematic uncertainty, due to binning scheme of single track PID efficiency, in each (p_{T}, y^*) bin for the (left) Fwd and (right) Bwd sample. Rapidity for the Bwd is plotted with absolute value.
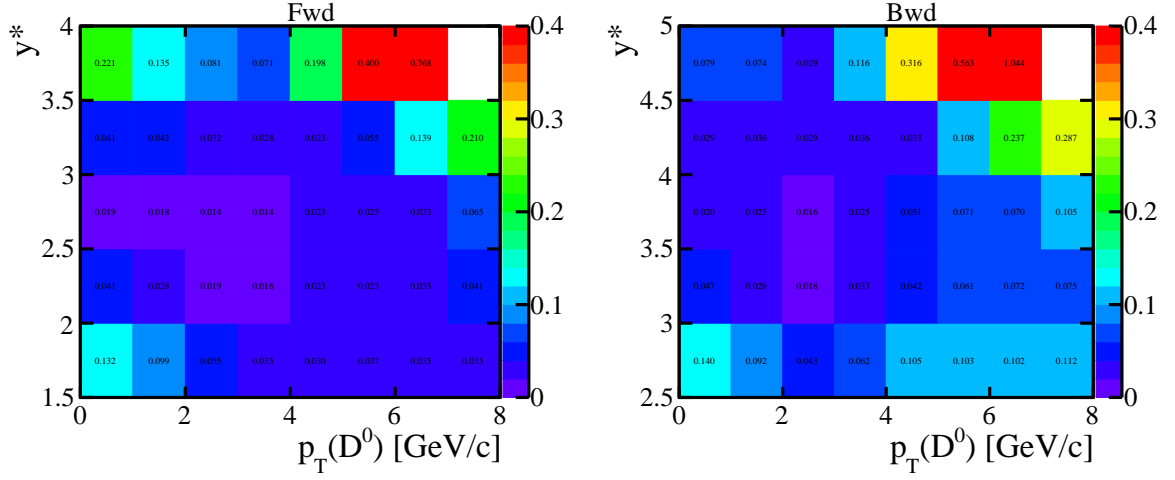
Figure 25: The total relative PID efficiency systematic uncertainty in each (p_T, y^*) bin for the (left) Fwd and (right) Bwd sample for the track calibration method. Rapidity for the Bwd is plotted with absolute value.
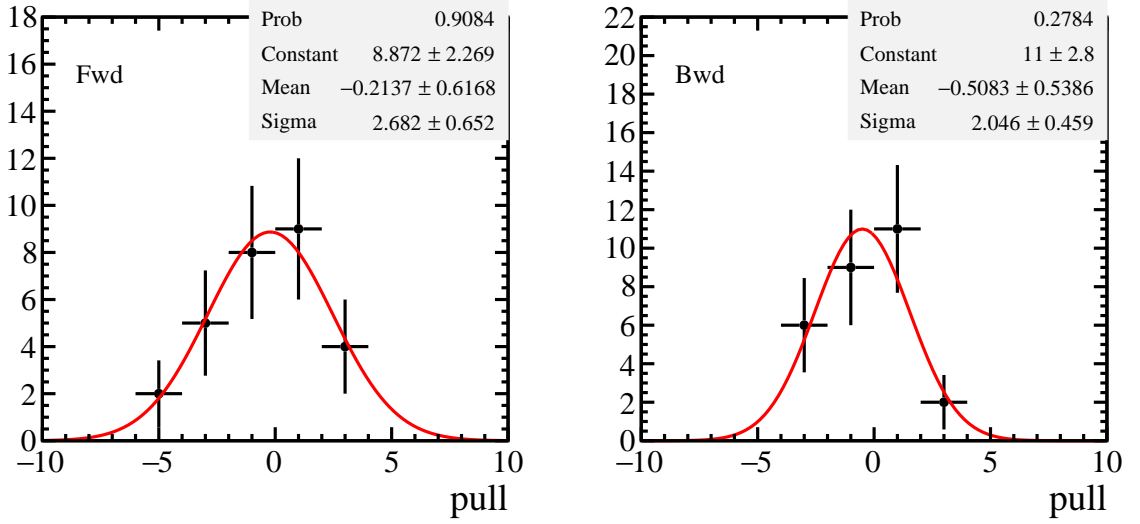
Figure 26: Distribution of (top) the pull of the PID efficiencies obtained using directly the PID calibration samples and the nominal results, and (bottom) the difference in absolute value in different bins.
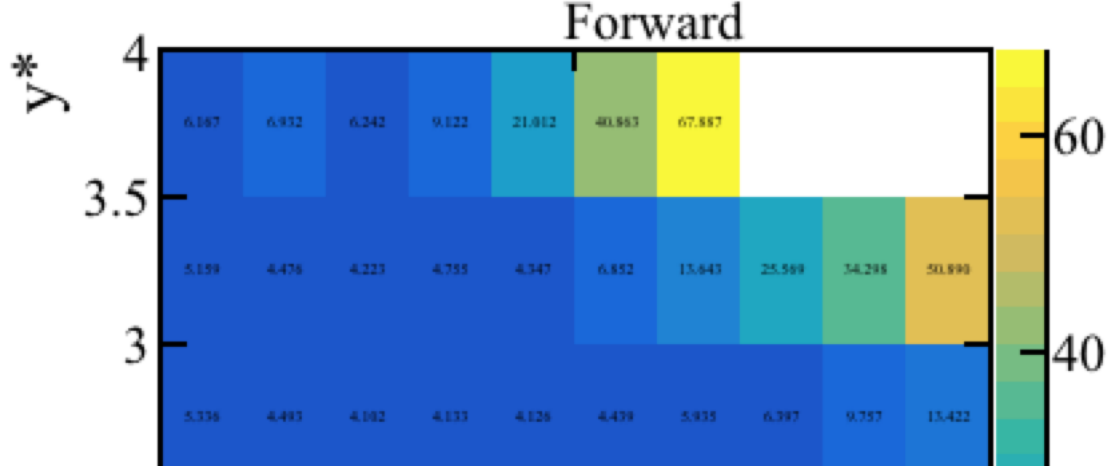
Figure 27: Total systematic uncertainties in each p_{T} and y bin for (left) Fwd and (right) Bwd.

Table 5: Summary of systematic and statistical uncertainties.

Source	Relative uncertainty (%)	
Correlated between bins	Fwd	Bwd
Mass fits to determine signal yields	0-5	0-5
χ^2_{IP} fits	0-5	0-5
Tracking	3.0	5.0
PID efficiency	0.6-17	0.6-30
Luminosity	1.9	2.1
$\mathcal{B}(D^0 \to K^- \pi^+)$	1.	1.
Uncorrelated between bins		
MC Sample size	1.0-4.0	1.0-5.0
Statistical uncertainty	0.5-20	1-20
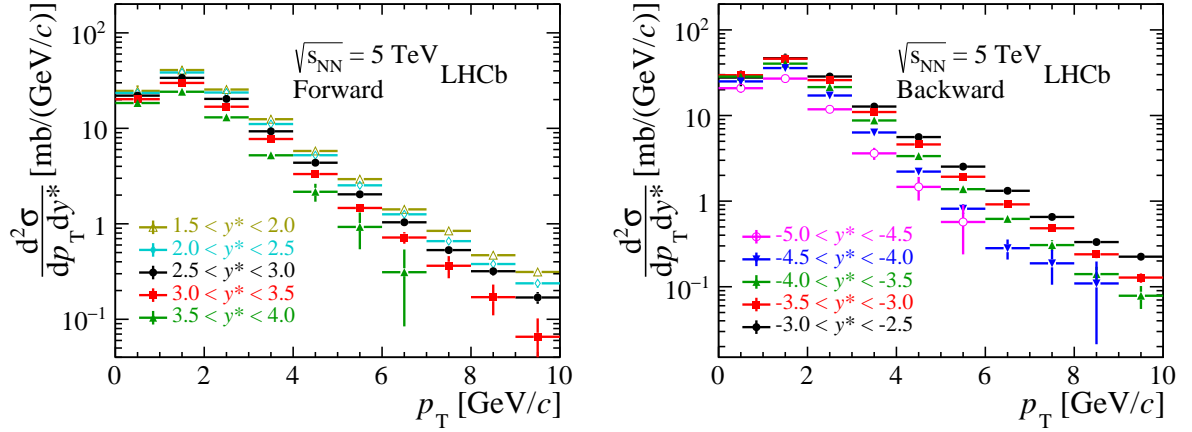
Figure 28: Double-differential cross-section $\frac{\mathrm{d}^2\sigma}{\mathrm{d}p_\mathrm{T}\mathrm{d}y^*}$ (mb/(GeV/c)) of prompt D^0 meson production in pPb collisions in the (left) forward and (right) backward collision samples. The uncertainty is the quadratic sum of the statistical and systematic components.

7   Results

7.1   Production cross-sections

The measured values of the double-differential cross-section of prompt D^0 mesons in proton-lead collisions in the forward and backward regions as a function of p_T and y^* are given in Table 6 and shown in Fig. 28. The one-dimensional differential prompt D^0 meson cross-sections as a function of p_T or y^* are reported in Tables 7 and 8, and are displayed in Fig. 29. The measurements are also shown as a function of p_T integrated[6] over y^* in the common rapidity range $2.5 < |y^*| < 4.0$.

The integrated cross-sections of prompt D^0 meson production in pPb forward data in the full and common fiducial regions are

$$\sigma_{\mathrm{forward}}(p_\mathrm{T} < 10\,\mathrm{GeV}/c, 1.5 < y^* < 4.0) = 230.6 \pm 0.5 \pm 13.0\,\mathrm{mb},$$

$$\sigma_{\mathrm{forward}}(p_\mathrm{T} < 10\,\mathrm{GeV}/c, 2.5 < y^* < 4.0) = 119.1 \pm 0.3 \pm\ \ 5.6\,\mathrm{mb}.$$

The integrated cross-sections of prompt D^0 meson production in Pbp backward data in the two fiducial regions are

$$\sigma_{\mathrm{backward}}(p_\mathrm{T} < 10\,\mathrm{GeV}/c, -2.5 < y^* < -5.0) = 252.7 \pm 1.0 \pm 20.0\,\mathrm{mb},$$

$$\sigma_{\mathrm{backward}}(p_\mathrm{T} < 10\,\mathrm{GeV}/c, -2.5 < y^* < -4.0) = 175.5 \pm 0.6 \pm 14.4\,\mathrm{mb},$$

where the first uncertainties are statistical and the second systematic.

---

[6] The integration over y^* is performed up to $|y^*|$=3.5 for $p_\mathrm{T} > 6\,\mathrm{GeV}/c$, neglecting the bin $3.5 < |y^*| < 4.0$ since it is not populated in the forward sample. This applies for the integrated cross-sections presented in this subsection, in Tables 7, 9 and 11 and in Figs. 29, 30, 33 and 34.

37

Table 6: Double-differential cross-section $\frac{\mathrm{d}^2\sigma}{\mathrm{d}p_\mathrm{T}\mathrm{d}y^*}$ (mb/(GeV/c)) for prompt D^0 meson production as functions of p_T and y^* in pPb forward and backward data, respectively. The first uncertainty is statistical, the second is the component of the systematic uncertainty that is uncorrelated between bins and the third is the correlated component. In the regions with no entries the signal is not statistically significant.

Forward (mb/(GeV/c))

p_T [GeV/c]	$1.5 < y^* < 2.0$	$2.0 < y^* < 2.5$	$2.5 < y^* < 3.0$	$3.0 < y^* < 3.5$	$3.5 < y^* < 4.0$
[0, 1]	$24.67 \pm 0.32 \pm 0.50 \pm 3.45$	$23.48 \pm 0.17 \pm 0.25 \pm 1.70$	$22.01 \pm 0.16 \pm 0.20 \pm 1.16$	$20.19 \pm 0.21 \pm 0.23 \pm 1.02$	$18.41 \pm 0.36 \pm 0.33 \pm 1.09$
[1, 2]	$40.79 \pm 0.34 \pm 0.61 \pm 3.83$	$38.45 \pm 0.19 \pm 0.35 \pm 2.19$	$33.79 \pm 0.18 \pm 0.26 \pm 1.50$	$29.89 \pm 0.22 \pm 0.28 \pm 1.31$	$24.17 \pm 0.34 \pm 0.40 \pm 1.63$
[2, 3]	$25.50 \pm 0.20 \pm 0.39 \pm 1.76$	$23.73 \pm 0.11 \pm 0.20 \pm 1.08$	$20.34 \pm 0.10 \pm 0.16 \pm 0.82$	$16.84 \pm 0.11 \pm 0.17 \pm 0.69$	$13.03 \pm 0.17 \pm 0.23 \pm 0.78$
[3, 4]	$12.46 \pm 0.11 \pm 0.21 \pm 0.63$	$11.09 \pm 0.06 \pm 0.10 \pm 0.47$	$9.31 \pm 0.05 \pm 0.09 \pm 0.38$	$7.73 \pm 0.06 \pm 0.09 \pm 0.36$	$5.22 \pm 0.09 \pm 0.11 \pm 0.46$
[4, 5]	$5.79 \pm 0.06 \pm 0.11 \pm 0.27$	$5.23 \pm 0.04 \pm 0.06 \pm 0.21$	$4.36 \pm 0.03 \pm 0.05 \pm 0.17$	$3.32 \pm 0.04 \pm 0.05 \pm 0.14$	$2.17 \pm 0.07 \pm 0.07 \pm 0.45$
[5, 6]	$2.94 \pm 0.04 \pm 0.07 \pm 0.14$	$2.53 \pm 0.03 \pm 0.04 \pm 0.11$	$2.04 \pm 0.02 \pm 0.03 \pm 0.09$	$1.47 \pm 0.02 \pm 0.03 \pm 0.10$	$0.93 \pm 0.07 \pm 0.07 \pm 0.37$
[6, 7]	$1.42 \pm 0.02 \pm 0.04 \pm 0.08$	$1.26 \pm 0.02 \pm 0.02 \pm 0.05$	$1.04 \pm 0.02 \pm 0.02 \pm 0.06$	$0.72 \pm 0.02 \pm 0.02 \pm 0.10$	$0.31 \pm 0.08 \pm 0.06 \pm 0.20$
[7, 8]	$0.84 \pm 0.02 \pm 0.03 \pm 0.04$	$0.66 \pm 0.01 \pm 0.02 \pm 0.04$	$0.53 \pm 0.01 \pm 0.01 \pm 0.03$	$0.36 \pm 0.02 \pm 0.02 \pm 0.09$	–
[8, 9]	$0.47 \pm 0.01 \pm 0.02 \pm 0.02$	$0.38 \pm 0.01 \pm 0.01 \pm 0.03$	$0.32 \pm 0.01 \pm 0.01 \pm 0.03$	$0.17 \pm 0.02 \pm 0.02 \pm 0.06$	–
[9, 10]	$0.31 \pm 0.01 \pm 0.02 \pm 0.02$	$0.24 \pm 0.01 \pm 0.01 \pm 0.02$	$0.17 \pm 0.01 \pm 0.01 \pm 0.02$	$0.07 \pm 0.01 \pm 0.01 \pm 0.03$	–

Backward (mb/(GeV/c))

| p_T [GeV/c]	$-3.0 < y^* < -2.5$	$-3.5 < y^* < -3.0$	$-4.0 < y^* < -3.5$	$-4.5 < y^* < -4.0$	$-5.0 < y^* < -4.5$
[0, 1]	$27.75 \pm 0.48 \pm 0.47 \pm 5.78$	$29.56 \pm 0.33 \pm 0.29 \pm 2.98$	$28.47 \pm 0.38 \pm 0.28 \pm 1.98$	$25.03 \pm 0.58 \pm 0.28 \pm 1.78$	$20.85 \pm 1.08 \pm 0.43 \pm 2.21$
[1, 2]	$46.66 \pm 0.51 \pm 0.69 \pm 6.13$	$46.10 \pm 0.35 \pm 0.38 \pm 3.40$	$40.35 \pm 0.38 \pm 0.33 \pm 2.61$	$35.82 \pm 0.56 \pm 0.38 \pm 2.54$	$27.00 \pm 1.01 \pm 0.45 \pm 2.81$
[2, 3]	$28.55 \pm 0.29 \pm 0.41 \pm 2.41$	$25.90 \pm 0.19 \pm 0.22 \pm 1.62$	$21.47 \pm 0.18 \pm 0.17 \pm 1.26$	$17.13 \pm 0.23 \pm 0.19 \pm 1.09$	$11.82 \pm 0.45 \pm 0.23 \pm 0.97$
[3, 4]	$12.73 \pm 0.15 \pm 0.18 \pm 0.93$	$10.98 \pm 0.10 \pm 0.10 \pm 0.64$	$8.75 \pm 0.09 \pm 0.08 \pm 0.50$	$6.33 \pm 0.10 \pm 0.08 \pm 0.45$	$3.61 \pm 0.17 \pm 0.09 \pm 0.55$
[4, 5]	$5.60 \pm 0.08 \pm 0.09 \pm 0.38$	$4.59 \pm 0.05 \pm 0.05 \pm 0.26$	$3.36 \pm 0.05 \pm 0.04 \pm 0.19$	$2.21 \pm 0.05 \pm 0.03 \pm 0.14$	$1.47 \pm 0.13 \pm 0.06 \pm 0.43$
[5, 6]	$2.53 \pm 0.05 \pm 0.05 \pm 0.16$	$1.93 \pm 0.03 \pm 0.03 \pm 0.11$	$1.38 \pm 0.03 \pm 0.02 \pm 0.08$	$0.82 \pm 0.03 \pm 0.02 \pm 0.10$	$0.57 \pm 0.14 \pm 0.06 \pm 0.30$
[6, 7]	$1.32 \pm 0.03 \pm 0.03 \pm 0.08$	$0.92 \pm 0.02 \pm 0.02 \pm 0.06$	$0.62 \pm 0.02 \pm 0.01 \pm 0.04$	$0.28 \pm 0.02 \pm 0.01 \pm 0.07$	–
[7, 8]	$0.65 \pm 0.02 \pm 0.02 \pm 0.04$	$0.48 \pm 0.02 \pm 0.01 \pm 0.04$	$0.31 \pm 0.01 \pm 0.01 \pm 0.04$	$0.19 \pm 0.03 \pm 0.01 \pm 0.08$	–
[8, 9]	$0.33 \pm 0.02 \pm 0.01 \pm 0.02$	$0.24 \pm 0.01 \pm 0.01 \pm 0.02$	$0.14 \pm 0.01 \pm 0.01 \pm 0.03$	$0.11 \pm 0.03 \pm 0.01 \pm 0.08$	–
[9, 10]	$0.22 \pm 0.01 \pm 0.01 \pm 0.02$	$0.13 \pm 0.01 \pm 0.01 \pm 0.01$	$0.08 \pm 0.01 \pm 0.00 \pm 0.02$	–	–
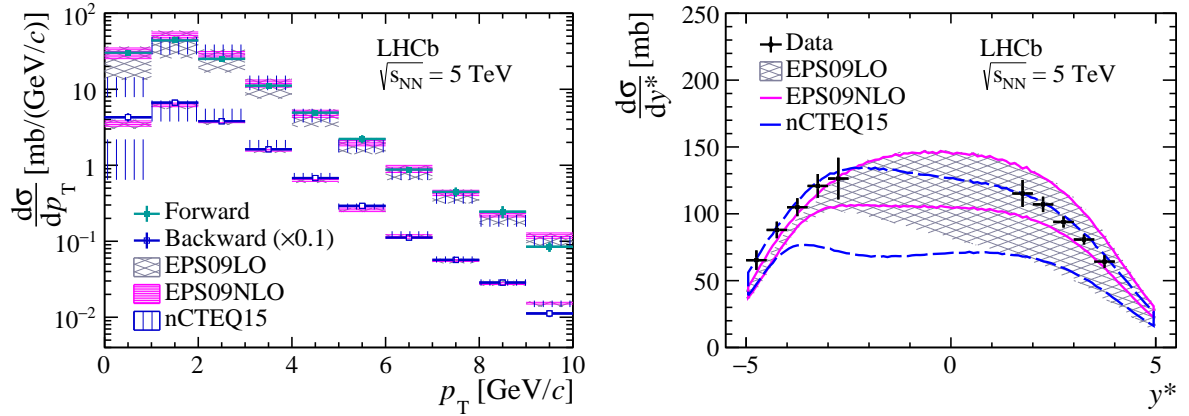
Figure 29: Differential cross-section of prompt D^0 meson production in pPb collisions as a function of (left) p_T ($\frac{d\sigma}{dp_T}$) and (right) y^* ($\frac{d\sigma}{dy^*}$) in the forward and backward collision samples. The uncertainty is the quadratic sum of the statistical and systematic components. The measurements are compared with theoretical predictions including different nuclear parton distribution functions as explained in the text.

The cross-sections as a function of p_T and y^*, shown in Fig. 29, are compared with calculations [46–48] validated with results of heavy-flavour production cross-section in pp collisions. The nuclear effects are considered by using three different sets of nuclear parton distribution functions (nPDFs), the leading-order EPS09 (EPS09LO) [49], the next-to-leading order EPS09 (EPS09NLO) [49] and nCTEQ15 [50]. The free nucleon PDF CT10NLO [51] is also used as a reference for the cross-section predictions in pp collisions. Within large theoretical uncertainties, all three sets of nPDFs can give descriptions consistent with the LHCb data, although a discrepancy is observed in the low p_T region between the measurements and the nCTEQ15 predictions.

7.2 Nuclear modification factors

The value of the D^0 meson production cross-section in pp collisions at $5\,\text{TeV}$, needed for the measurement of the nuclear modification factor $R_{p\text{Pb}}$, is taken from the LHCb measurement [44]. Correlations between the uncertainties of quantities that are common to both measurements are taken into account. The nuclear modification factor for prompt D^0 meson production is shown in Fig. 30 in bins of p_T and Fig. 31 in bins of y^*. The nuclear modification factors are calculated as a function of p_T integrated over y^* in the ranges described in Fig. 30 for both forward and backward samples. The values of $R_{p\text{Pb}}$, summarised in Tables 9 and 10, show a slight increase as a function of p_T, suggesting that the suppression may decrease with increasing transverse momentum.

The measurements are compared with calculations using EPS09LO, EPSNLO and nCTEQ15 nPDFs [46–48]. For the results in the backward configuration, all three predictions show reasonable agreement with each other and with LHCb data. In the

Table 7: Measured differential cross-section $\frac{\mathrm{d}\sigma}{\mathrm{d}p_{\mathrm{T}}}$ (mb/(GeV/c)) for prompt D^0 meson production as a function of p_{T} in pPb forward and backward data, respectively. The first uncertainty is statistical, the second is the component of the systematic uncertainty that is uncorrelated between bins and the third is the correlated component. The results in the last two columns are integrated over the common rapidity range $2.5 < |y^*| < 4.0$ for $p_{\mathrm{T}} < 6 \, \mathrm{GeV}/c$ and over $2.5 < |y^*| < 3.5$ for $6 < p_{\mathrm{T}} < 10 \, \mathrm{GeV}/c$.

	Forward (mb/(GeV/c))		
$p_{\mathrm{T}}[\,\mathrm{GeV}/c]$	$1.5 < y^* < 4.0$	$2.5 < y^* < 4.0$	$2.5 < y^* < 3.5$
$[0,1]$	$54.38 \pm 0.29 \pm 0.36 \pm 3.96$	$30.31 \pm 0.22 \pm 0.22 \pm 1.59$	$-$
$[1,2]$	$83.54 \pm 0.30 \pm 0.45 \pm 5.01$	$43.92 \pm 0.22 \pm 0.28 \pm 2.17$	$-$
$[2,3]$	$49.72 \pm 0.16 \pm 0.27 \pm 2.45$	$25.11 \pm 0.11 \pm 0.16 \pm 1.11$	$-$
$[3,4]$	$22.91 \pm 0.09 \pm 0.14 \pm 1.10$	$11.13 \pm 0.06 \pm 0.08 \pm 0.55$	$-$
$[4,5]$	$10.43 \pm 0.06 \pm 0.08 \pm 0.54$	$4.92 \pm 0.04 \pm 0.05 \pm 0.32$	$-$
$[5,6]$	$4.95 \pm 0.05 \pm 0.06 \pm 0.35$	$2.21 \pm 0.04 \pm 0.04 \pm 0.26$	$-$
$[6,7]$	$2.37 \pm 0.05 \pm 0.04 \pm 0.21$	$-$	$0.88 \pm 0.01 \pm 0.01 \pm 0.07$
$[7,8]$	$1.20 \pm 0.02 \pm 0.02 \pm 0.09$	$-$	$0.45 \pm 0.01 \pm 0.01 \pm 0.06$
$[8,9]$	$0.67 \pm 0.01 \pm 0.01 \pm 0.06$	$-$	$0.24 \pm 0.01 \pm 0.01 \pm 0.04$
$[9,10]$	$0.39 \pm 0.01 \pm 0.01 \pm 0.04$	$-$	$0.08 \pm 0.00 \pm 0.00 \pm 0.01$
	Backward (mb/(GeV/c))		
$p_{\mathrm{T}}[\,\mathrm{GeV}/c]$	$-5.0 < y^* < -2.5$	$-4.0 < y^* < -2.5$	$-3.5 < y^* < -2.5$
$[0,1]$	$65.83 \pm 0.70 \pm 0.40 \pm 6.85$	$42.89 \pm 0.35 \pm 0.31 \pm 5.15$	$-$
$[1,2]$	$97.97 \pm 0.68 \pm 0.52 \pm 8.30$	$66.56 \pm 0.36 \pm 0.43 \pm 5.80$	$-$
$[2,3]$	$52.43 \pm 0.32 \pm 0.29 \pm 3.57$	$37.96 \pm 0.20 \pm 0.25 \pm 2.56$	$-$
$[3,4]$	$21.21 \pm 0.14 \pm 0.13 \pm 1.45$	$16.23 \pm 0.10 \pm 0.11 \pm 1.01$	$-$
$[4,5]$	$8.62 \pm 0.09 \pm 0.06 \pm 0.62$	$6.78 \pm 0.05 \pm 0.05 \pm 0.41$	$-$
$[5,6]$	$3.61 \pm 0.08 \pm 0.04 \pm 0.33$	$2.92 \pm 0.03 \pm 0.03 \pm 0.18$	$-$
$[6,7]$	$1.57 \pm 0.03 \pm 0.02 \pm 0.12$	$-$	$1.12 \pm 0.02 \pm 0.02 \pm 0.07$
$[7,8]$	$0.81 \pm 0.02 \pm 0.01 \pm 0.09$	$-$	$0.57 \pm 0.01 \pm 0.01 \pm 0.04$
$[8,9]$	$0.41 \pm 0.02 \pm 0.01 \pm 0.07$	$-$	$0.29 \pm 0.01 \pm 0.01 \pm 0.02$
$[9,10]$	$0.22 \pm 0.01 \pm 0.01 \pm 0.02$	$-$	$0.11 \pm 0.01 \pm 0.01 \pm 0.01$

forward configuration, nCTEQ15 and EPS09LO show better agreement with the data than EPS09NLO. Calculations [52] using CTEQ6M [53] nucleon PDF and EPS09NLO nPDF give results for $R_{p\mathrm{Pb}}$ that are similar to a combination of CT10NLO and EPS09NLO.

The nuclear modification factors for prompt D^0 are also compared with those for prompt J/ψ [38] in Fig. 31 as a function of p_{T} integrated over rapidity, and they are found to be consistent. This is the first measurement of $R_{p\mathrm{Pb}}$ in this kinematic range. The ratios of the nuclear modification factors of J/ψ and $\psi(2S)$ mesons to D^0 mesons as a function of rapidity are shown in Fig. 32 where a different suppression between the two charmonium states can be observed. In Figs. 30 and 31 the measurements are also compared with calculations in the colour glass condensate framework (CGC) [54], which includes the effect of the saturation of partons at small x. The CGC model is found to be able to describe the trend of prompt D^0 meson nuclear modifications as a function of p_{T} and of rapidity. The uncertainty band for this model is much smaller than for the nuclear PDF calculations,

Table 8: Differential cross-section $\frac{\mathrm{d}\sigma}{\mathrm{d}y^*}$ (mb) for prompt D^0 meson production as a function of $|y^*|$ in pPb forward and backward data, respectively. The first uncertainty is statistical, the second is the component of the systematic uncertainty that is uncorrelated between bins and the third is the correlated component.

	Forward (mb)
y^*	$0 < p_{\mathrm{T}} < 10\,\mathrm{GeV}/c$
$[1.5, 2.0]$	$115.19 \pm 0.53 \pm 0.91 \pm 9.99$
$[2.0, 2.5]$	$107.05 \pm 0.29 \pm 0.50 \pm 5.73$
$[2.5, 3.0]$	$93.90 \pm 0.27 \pm 0.38 \pm 4.14$
$[3.0, 3.5]$	$80.76 \pm 0.33 \pm 0.42 \pm 3.71$
$[3.5, 4.0]$	$64.24 \pm 0.55 \pm 0.58 \pm 4.79$
	Backward (mb)
y^*	$0 < p_{\mathrm{T}} < 10\,\mathrm{GeV}/c$
$[-3.0, -2.5]$	$126.35 \pm 0.78 \pm 0.95 \pm 15.54$
$[-3.5, -3.0]$	$120.84 \pm 0.53 \pm 0.53 \pm 8.89$
$[-4.0, -3.5]$	$104.93 \pm 0.58 \pm 0.47 \pm 6.66$
$[-4.5, -4.0]$	$87.92 \pm 0.85 \pm 0.52 \pm 6.13$
$[-5.0, -4.5]$	$65.32 \pm 1.57 \pm 0.68 \pm 7.07$
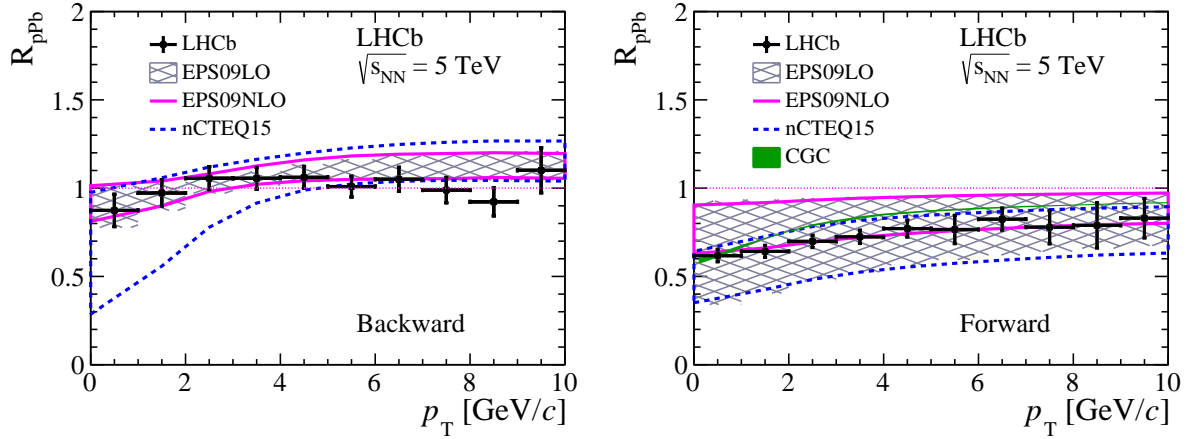
Figure 30: Nuclear modification factor $R_{p\mathrm{Pb}}$ as a function of p_{T} for prompt D^0 meson production in the (left) backward data and (right) forward data, integrated over the common rapidity range $2.5 < |y^*| < 4.0$ for $p_{\mathrm{T}} < 6\,\mathrm{GeV}/c$ and over $2.5 < |y^*| < 3.5$ for $6 < p_{\mathrm{T}} < 10\,\mathrm{GeV}/c$. The uncertainty is the quadratic sum of the statistical and systematic components. The CGC predictions are only available for the forward region.

737 since it only contains the variation of charm quark masses and factorisation scale which
738 largely cancel in this ratio of cross-sections. Another CGC framework calculation gives
739 similar results for nuclear modifications of charm production [?]. In the context of pPb
740 collisions, recent measurements have shown that long-range collective effects, which have
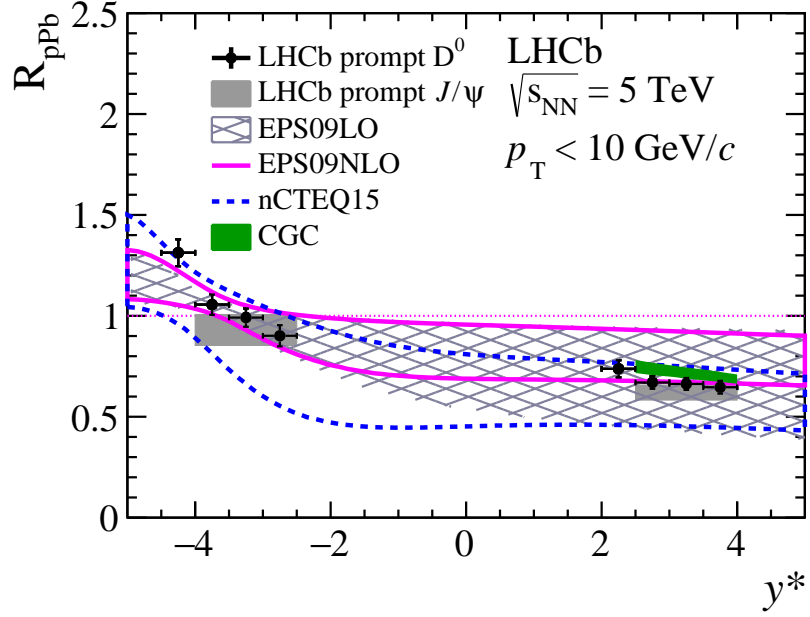
41

Figure 31: Nuclear modification factor $R_{p\mathrm{Pb}}$ as a function of y^* for prompt D^0 meson production, integrated up to $p_\mathrm{T} = 10\,\mathrm{GeV}/c$. The uncertainty is the quadratic sum of the statistical and systematic components.

previously been observed in relatively large nucleus-nucleus collision systems, may also be present in smaller collision systems at large charged particle multiplicities [**?**, 27–29]. If these effects are due to the creation of a hydrodynamic system, momentum anisotropies at the quark level can arise, which may modify the final distribution of observed heavy-quark hadrons [**?**]. Since the measurements in this analysis do not consider a classification in charged particle multiplicity, potential modifications in high-multiplicity events are weakened as the presented observables are integrated over charged particle multiplicity.

7.3 Forward-backward ratio

In the forward-backward production ratio R_{FB} the common uncertainty between the forward and backward measurements largely cancels. The uncertainties of branching fraction, signal yield and tracking are considered fully correlated, while the PID uncertainty is considered 90% correlated since it is a mixture of statistical uncertainty (uncorrelated) and the uncertainties due to the binning scheme and yield determination (correlated). All other uncertainties are uncorrelated. The measured R_{FB} values are shown in Fig. 33, as a function of p_T integrated over the range $2.5 < |y^*| < 4.0$, and as a function of y^* integrated up to $p_\mathrm{T} = 10\,\mathrm{GeV}/c$. The R_{FB} values in different kinematic bins are also summarised in Table 11. Good agreement is found between measurements and theoretical predictions using EPS09LO and nCTEQ15 nPDFs.

Table 9: Nuclear modification factor $R_{p\text{Pb}}$ for prompt D^0 meson production in different p_T ranges, integrated over the common rapidity range $2.5 < |y^*| < 4.0$ for $p_\text{T} < 6\,\text{GeV}/c$ and over $2.5 < |y^*| < 3.5$ for $6 < p_\text{T} < 10\,\text{GeV}/c$ for the forward (positive y^*) and backward (negative y^*) samples. The first uncertainty is statistical and the second systematic.

$p_\text{T}[\,\text{GeV}/c]$	Forward	Backward
$[0, 1]$	$0.62 \pm 0.01 \pm 0.03$	$0.87 \pm 0.01 \pm 0.09$
$[1, 2]$	$0.64 \pm 0.01 \pm 0.03$	$0.97 \pm 0.01 \pm 0.07$
$[2, 3]$	$0.70 \pm 0.01 \pm 0.03$	$1.06 \pm 0.01 \pm 0.07$
$[3, 4]$	$0.72 \pm 0.01 \pm 0.04$	$1.06 \pm 0.01 \pm 0.06$
$[4, 5]$	$0.77 \pm 0.01 \pm 0.05$	$1.06 \pm 0.01 \pm 0.06$
$[5, 6]$	$0.77 \pm 0.02 \pm 0.08$	$1.01 \pm 0.02 \pm 0.06$
$[6, 7]$	$0.82 \pm 0.02 \pm 0.06$	$1.05 \pm 0.03 \pm 0.06$
$[7, 8]$	$0.78 \pm 0.03 \pm 0.09$	$0.99 \pm 0.04 \pm 0.06$
$[8, 9]$	$0.79 \pm 0.05 \pm 0.12$	$0.92 \pm 0.05 \pm 0.07$
$[9, 10]$	$0.83 \pm 0.07 \pm 0.09$	$1.10 \pm 0.10 \pm 0.09$
$[0, 10]$	$0.66 \pm 0.00 \pm 0.03$	$0.97 \pm 0.01 \pm 0.07$

Table 10: Nuclear modification factor $R_{p\text{Pb}}$ for prompt D^0 meson production in different y^* ranges, integrated up to $p_\text{T} = 10\,\text{GeV}/c$. The first uncertainty is statistical and the second systematic.

y^*	$R_{p\text{Pb}}$
$[-4.5, -4.0]$	$1.31 \pm 0.02 \pm 0.06$
$[-4.0, -3.5]$	$1.05 \pm 0.01 \pm 0.05$
$[-3.5, -3.0]$	$0.99 \pm 0.01 \pm 0.04$
$[-3.0, -2.5]$	$0.90 \pm 0.01 \pm 0.05$
$[2.0, 2.5]$	$0.74 \pm 0.01 \pm 0.04$
$[2.5, 3.0]$	$0.67 \pm 0.00 \pm 0.03$
$[3.0, 3.5]$	$0.66 \pm 0.00 \pm 0.03$
$[3.5, 4.0]$	$0.65 \pm 0.01 \pm 0.03$

In the common kinematic range $p_\text{T} < 10\,\text{GeV}/c$, $2.5 < |y^*| < 4.0$, the forward-backward ratio R_FB is $0.71 \pm 0.01(\text{stat}) \pm 0.04(\text{syst})$, indicating a significant asymmetry. The predictions for R_FB integrated over the same kinematic range are $0.71^{+0.21}_{-0.24}$ for EPS09 at leading order, $0.81^{+0.10}_{-0.09}$ for EPS09 at next-to-leading order and $0.69^{+0.07}_{-0.07}$ for the nCTEQ15 nPDF set, which are all in good agreement with the measured value. The forward-backward production ratio increases slightly with increasing p_T, and decreases strongly with increasing rapidity $|y^*|$. This behaviour is consistent with the expectations from the QCD calculations.

In order to compare the production of open charm and charmonium, the ratio of R_FB for prompt J/ψ mesons divided by R_FB for prompt D^0 mesons is shown in Fig. 34. The measurement shows that R_FB has the same size for prompt D^0 and prompt J/ψ mesons

Table 11: Forward-backward ratio R_{FB} for prompt D^0 meson production in different p_{T} ranges, integrated over the common rapidity range $2.5 < |y^*| < 4.0$ for $p_{\mathrm{T}} < 6\,\mathrm{GeV}/c$ and over $2.5 < |y^*| < 3.5$ for $6 < p_{\mathrm{T}} < 10\,\mathrm{GeV}/c$, and in different y^* ranges integrated up to $p_{\mathrm{T}} = 10\,\mathrm{GeV}/c$. The first uncertainty is the statistical and the second is the systematic component.

$p_{\mathrm{T}}[\,\mathrm{GeV}/c]$	R_{FB}
$[0,1]$	$0.71 \pm 0.01 \pm 0.06$
$[1,2]$	$0.66 \pm 0.00 \pm 0.04$
$[2,3]$	$0.66 \pm 0.00 \pm 0.03$
$[3,4]$	$0.69 \pm 0.01 \pm 0.03$
$[4,5]$	$0.73 \pm 0.01 \pm 0.04$
$[5,6]$	$0.76 \pm 0.02 \pm 0.08$
$[6,7]$	$0.79 \pm 0.02 \pm 0.05$
$[7,8]$	$0.79 \pm 0.03 \pm 0.09$
$[8,9]$	$0.86 \pm 0.04 \pm 0.12$
$[9,10]$	$0.75 \pm 0.06 \pm 0.09$
$[0,10]$	$0.68 \pm 0.00 \pm 0.04$
$|y^*|$	R_{FB}
$[2.5,3.0]$	$0.74 \pm 0.01 \pm 0.07$
$[3.0,3.5]$	$0.67 \pm 0.00 \pm 0.03$
$[3.5,4.0]$	$0.61 \pm 0.01 \pm 0.03$

within the uncertainties in the LHCb kinematic range.

8 Conclusion

The prompt D^0 production cross-section has been measured with LHCb proton-lead collision data at $\sqrt{s_{NN}} = 5\,\mathrm{TeV}$, in the forward and backward configurations. Cold nuclear modifications factors and forward backward production ratios are measured. Large asymmetry in the forward/backward production is observed, suggesting strong cold nuclear matter effect.
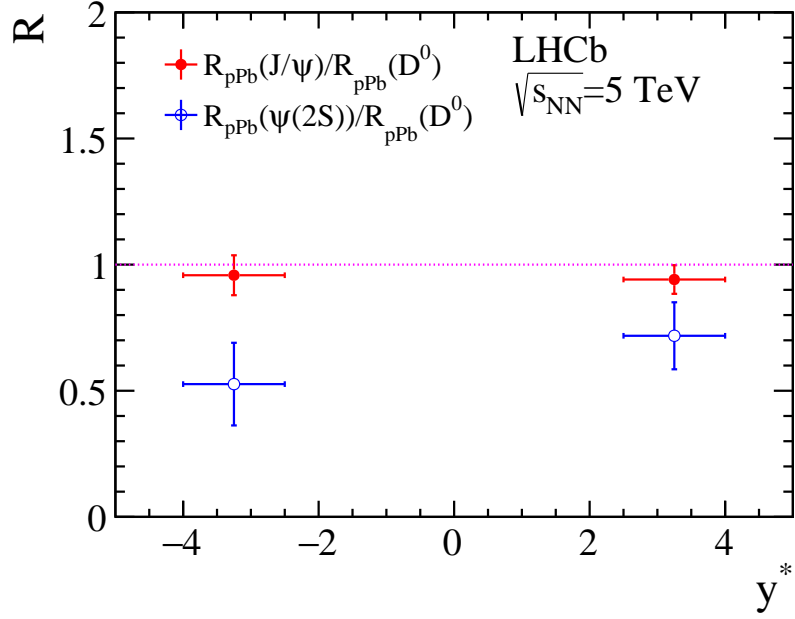
Figure 32: Ratio of nuclear modification factors $R_{p\text{Pb}}$ of J/ψ and $\psi(2S)$ to D^0 mesons in bins of rapidity integrated up to $p_T = 10\,\text{GeV}/c$ in the common rapidity range $2.5 < |y^*| < 4.0$. The uncertainty is the quadratic sum of the statistical and systematic components.
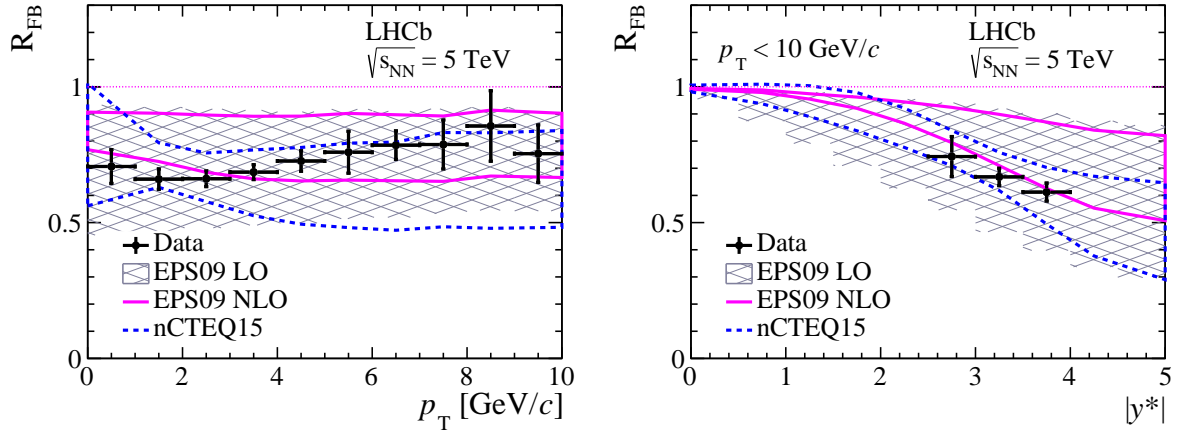
Figure 33: Forward-backward ratio R_{FB} for prompt D^0 meson production (left) as a function of p_T integrated over the common rapidity range $2.5 < |y^*| < 4.0$ for $p_T < 6\,\text{GeV}/c$ and over $2.5 < |y^*| < 3.5$ for $6 < p_T < 10\,\text{GeV}/c$; (right) as a function of y^* integrated up to $p_T = 10\,\text{GeV}/c$. The uncertainty is the quadratic sum of the statistical and systematic components.
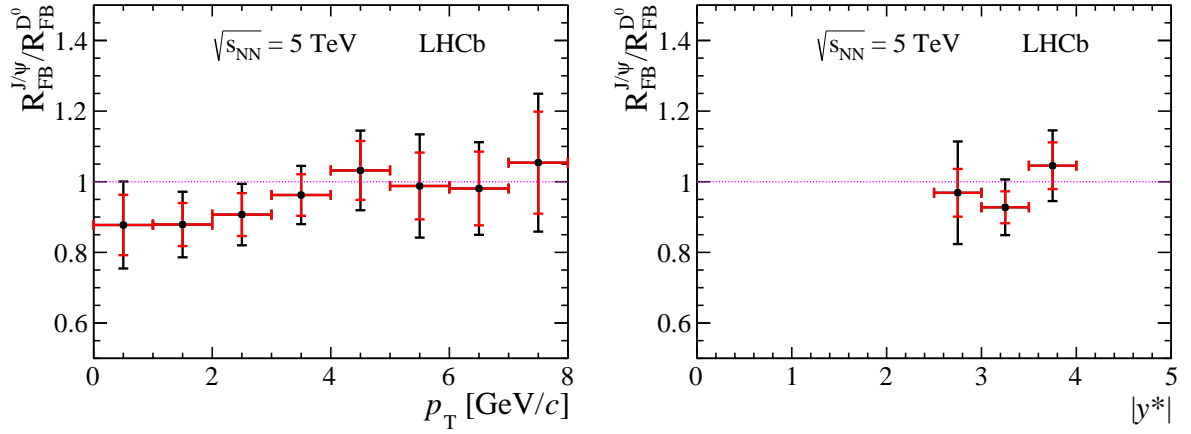
Figure 34: Relative forward-backward production ratio R_{FB} for prompt D^0 mesons over that for prompt J/ψ mesons (left) as a function of p_T integrated over the common rapidity range $2.5 < |y^*| < 4.0$ for $p_T < 6\,\mathrm{GeV}/c$ and over $2.5 < |y^*| < 3.5$ for $6 < p_T < 10\,\mathrm{GeV}/c$; (right) as a function of y^* integrated up to $p_T = 10\,\mathrm{GeV}/c$. The red inner bars in the uncertainty represent the statistical uncertainty and the black outer bars the quadratic sum of the statistical and systematic components.

A Efficiency tables

The efficiencies tables for ϵ_{acc} are 13 and 12. The efficiencies tables for ϵ_{Rec} are 15 and 14.
The efficiencies tables for ϵ_{PID} are 17 and 16. The efficiencies tables for ϵ_{Tot} are 19 and 18.
Uncertainties are statistical only.

Table 12: Geometrical acceptance efficiencies in bins of D^0 p_{T} and $y*$ for Fwd collision configuration.

$p_{\mathrm{T}}[\,\mathrm{GeV}/c]\backslash y*$	$(1.5, 2]$	$(2, 2.5]$	$(2.5, 3]$	$(3, 3.5]$	$(3.5, 4]$
$[0, 1]$	0.739 ± 0.007	0.914 ± 0.004	0.950 ± 0.004	0.917 ± 0.005	0.787 ± 0.008
$[1, 2]$	0.778 ± 0.006	0.930 ± 0.004	0.968 ± 0.003	0.944 ± 0.004	0.830 ± 0.007
$[2, 3]$	0.837 ± 0.006	0.960 ± 0.004	0.984 ± 0.003	0.963 ± 0.004	0.868 ± 0.009
$[3, 4]$	0.886 ± 0.008	0.985 ± 0.003	0.988 ± 0.003	0.983 ± 0.004	0.937 ± 0.009
$[4, 5]$	0.931 ± 0.008	0.993 ± 0.003	0.998 ± 0.002	0.990 ± 0.005	0.987 ± 0.006
$[5, 6]$	0.940 ± 0.011	0.993 ± 0.004	1.000 ± 0.000	1.000 ± 0.000	0.979 ± 0.012
$[6, 7]$	0.968 ± 0.010	0.996 ± 0.004	1.000 ± 0.000	1.000 ± 0.000	1.000 ± 0.000
$[7, 8]$	0.975 ± 0.013	1.000 ± 0.000	0.992 ± 0.008	1.000 ± 0.000	1.000 ± 0.000
$[8, 9]$	0.973 ± 0.015	1.000 ± 0.000	1.000 ± 0.000	1.000 ± 0.000	1.000 ± 0.000
$[9, 10]$	1.000 ± 0.000	1.000 ± 0.000	1.000 ± 0.000	1.000 ± 0.000	1.000 ± 0.000

Table 13: Geometrical acceptance efficiencies in bins of D^0 p_{T} and $y*$ for Bwd Configuration.

$p_{\mathrm{T}}[\,\mathrm{GeV}/c]\backslash y*$	$(2.5, 3]$	$(3, 3.5]$	$(3.5, 4]$	$(4, 4.5]$	$(4.5, 5]$
$[0, 1]$	0.783 ± 0.006	0.924 ± 0.004	0.952 ± 0.004	0.908 ± 0.005	0.751 ± 0.008
$[1, 2]$	0.813 ± 0.005	0.940 ± 0.004	0.970 ± 0.003	0.930 ± 0.004	0.814 ± 0.008
$[2, 3]$	0.871 ± 0.006	0.970 ± 0.003	0.984 ± 0.003	0.956 ± 0.005	0.851 ± 0.010
$[3, 4]$	0.914 ± 0.007	0.988 ± 0.003	0.989 ± 0.003	0.977 ± 0.005	0.934 ± 0.010
$[4, 5]$	0.952 ± 0.007	0.997 ± 0.002	1.000 ± 0.000	0.989 ± 0.005	0.986 ± 0.007
$[5, 6]$	0.948 ± 0.010	0.995 ± 0.003	1.000 ± 0.000	1.000 ± 0.000	0.970 ± 0.015
$[6, 7]$	0.982 ± 0.008	1.000 ± 0.000	1.000 ± 0.000	1.000 ± 0.000	1.000 ± 0.000
$[7, 8]$	0.980 ± 0.011	1.000 ± 0.000	0.992 ± 0.008	1.000 ± 0.000	1.000 ± 0.000
$[8, 9]$	0.990 ± 0.010	1.000 ± 0.000	1.000 ± 0.000	1.000 ± 0.000	1.000 ± 0.000
$[9, 10]$	1.000 ± 0.000	1.000 ± 0.000	1.000 ± 0.000	1.000 ± 0.000	1.000 ± 0.000

Table 14: Reconstruction-selection efficiencies in bins of D^0 p_{T} and $y*$ for Fwd collision configuration.

$p_{\mathrm{T}}[\,\mathrm{GeV}/c]\backslash y*$	$(1.5, 2]$	$(2, 2.5]$	$(2.5, 3]$	$(3, 3.5]$	$(3.5, 4]$
$[0, 1]$	0.027 ± 0.001	0.083 ± 0.001	0.097 ± 0.001	0.080 ± 0.001	0.048 ± 0.001
$[1, 2]$	0.031 ± 0.000	0.085 ± 0.001	0.098 ± 0.001	0.082 ± 0.001	0.051 ± 0.001
$[2, 3]$	0.046 ± 0.001	0.120 ± 0.001	0.132 ± 0.001	0.112 ± 0.001	0.066 ± 0.001
$[3, 4]$	0.069 ± 0.001	0.162 ± 0.001	0.175 ± 0.002	0.148 ± 0.002	0.075 ± 0.001
$[4, 5]$	0.089 ± 0.002	0.189 ± 0.002	0.203 ± 0.002	0.178 ± 0.002	0.051 ± 0.002
$[5, 6]$	0.107 ± 0.002	0.210 ± 0.003	0.222 ± 0.003	0.174 ± 0.003	0.021 ± 0.002
$[6, 7]$	0.119 ± 0.003	0.219 ± 0.004	0.230 ± 0.004	0.141 ± 0.004	0.006 ± 0.001
$[7, 8]$	0.127 ± 0.004	0.226 ± 0.005	0.232 ± 0.006	0.087 ± 0.005	0.000 ± 0.000
$[8, 9]$	0.139 ± 0.005	0.233 ± 0.007	0.216 ± 0.008	0.061 ± 0.005	0.000 ± 0.000
$[9, 10]$	0.127 ± 0.007	0.223 ± 0.009	0.202 ± 0.010	0.036 ± 0.005	0.000 ± 0.000

Table 15: Reconstruction-selection efficiencies in bins of D^0 p_{T} and $y*$ for Bwd collision configuration.

$p_{\mathrm{T}}[\,\mathrm{GeV}/c]\backslash y*$	$(2.5, 3]$	$(3, 3.5]$	$(3.5, 4]$	$(4, 4.5]$	$(4.5, 5]$
$[0, 1]$	0.033 ± 0.001	0.082 ± 0.001	0.089 ± 0.001	0.071 ± 0.001	0.041 ± 0.001
$[1, 2]$	0.038 ± 0.001	0.082 ± 0.001	0.091 ± 0.001	0.073 ± 0.001	0.043 ± 0.001
$[2, 3]$	0.056 ± 0.001	0.116 ± 0.001	0.122 ± 0.001	0.101 ± 0.001	0.053 ± 0.001
$[3, 4]$	0.082 ± 0.001	0.156 ± 0.001	0.162 ± 0.001	0.134 ± 0.002	0.056 ± 0.001
$[4, 5]$	0.105 ± 0.002	0.181 ± 0.002	0.190 ± 0.002	0.154 ± 0.002	0.034 ± 0.001
$[5, 6]$	0.125 ± 0.002	0.201 ± 0.003	0.207 ± 0.003	0.143 ± 0.003	0.012 ± 0.001
$[6, 7]$	0.136 ± 0.003	0.208 ± 0.004	0.218 ± 0.004	0.107 ± 0.004	0.002 ± 0.001
$[7, 8]$	0.146 ± 0.004	0.215 ± 0.005	0.210 ± 0.006	0.058 ± 0.004	0.000 ± 0.000
$[8, 9]$	0.162 ± 0.006	0.220 ± 0.007	0.191 ± 0.007	0.035 ± 0.004	0.000 ± 0.000
$[9, 10]$	0.145 ± 0.007	0.220 ± 0.009	0.164 ± 0.009	0.016 ± 0.004	0.000 ± 0.000

Table 16: PID efficiencies in bins of D^0 p_{T} and $y*$ for Fwd collision configuration.

$p_{\mathrm{T}}[\,\mathrm{GeV}/c]\backslash y*$	$(2.5, 3]$	$(3, 3.5]$	$(3.5, 4]$	$(4, 4.5]$	$(4.5, 5]$
$[0, 1]$	0.818 ± 0.092	0.793 ± 0.041	0.837 ± 0.024	0.850 ± 0.013	0.729 ± 0.024
$[1, 2]$	0.819 ± 0.059	0.830 ± 0.027	0.866 ± 0.015	0.847 ± 0.013	0.671 ± 0.027
$[2, 3]$	0.840 ± 0.040	0.875 ± 0.018	0.899 ± 0.007	0.840 ± 0.008	0.585 ± 0.020
$[3, 4]$	0.872 ± 0.025	0.906 ± 0.011	0.914 ± 0.006	0.800 ± 0.016	0.513 ± 0.034
$[4, 5]$	0.898 ± 0.018	0.921 ± 0.008	0.911 ± 0.006	0.735 ± 0.005	0.430 ± 0.071
$[5, 6]$	0.918 ± 0.018	0.917 ± 0.007	0.885 ± 0.012	0.669 ± 0.029	0.373 ± 0.123
$[6, 7]$	0.925 ± 0.015	0.893 ± 0.013	0.835 ± 0.017	0.618 ± 0.065	0.327 ± 0.175
$[7, 8]$	0.912 ± 0.011	0.856 ± 0.024	0.799 ± 0.026	0.562 ± 0.114	0.000 ± 1.000
$[8, 9]$	0.892 ± 0.014	0.822 ± 0.043	0.754 ± 0.050	0.523 ± 0.140	0.000 ± 1.000
$[9, 10]$	0.858 ± 0.013	0.776 ± 0.050	0.718 ± 0.070	0.438 ± 0.175	0.000 ± 1.000

Table 17: PID efficiencies in bins of D^0 p_T and $y*$ for Bwd collision configuration.

$p_\mathrm{T}[\,\mathrm{GeV}/c]\backslash y*$	$(2.5, 3]$	$(3, 3.5]$	$(3.5, 4]$	$(4, 4.5]$	$(4.5, 5]$
$[0, 1]$	0.742 ± 0.124	0.703 ± 0.049	0.731 ± 0.022	0.715 ± 0.016	0.572 ± 0.033
$[1, 2]$	0.749 ± 0.074	0.754 ± 0.030	0.772 ± 0.017	0.719 ± 0.018	0.510 ± 0.032
$[2, 3]$	0.784 ± 0.041	0.814 ± 0.019	0.817 ± 0.010	0.706 ± 0.016	0.426 ± 0.019
$[3, 4]$	0.828 ± 0.032	0.858 ± 0.012	0.833 ± 0.008	0.645 ± 0.024	0.357 ± 0.041
$[4, 5]$	0.863 ± 0.026	0.876 ± 0.007	0.826 ± 0.005	0.571 ± 0.012	0.272 ± 0.064
$[5, 6]$	0.883 ± 0.022	0.874 ± 0.009	0.793 ± 0.009	0.510 ± 0.045	0.225 ± 0.094
$[6, 7]$	0.886 ± 0.016	0.852 ± 0.022	0.732 ± 0.023	0.462 ± 0.092	0.207 ± 0.140
$[7, 8]$	0.861 ± 0.014	0.816 ± 0.029	0.682 ± 0.064	0.419 ± 0.140	0.000 ± 1.000
$[8, 9]$	0.834 ± 0.016	0.778 ± 0.038	0.627 ± 0.098	0.339 ± 0.205	0.000 ± 1.000
$[9, 10]$	0.786 ± 0.020	0.740 ± 0.050	0.573 ± 0.124	0.285 ± 0.307	0.000 ± 1.000

Table 18: Total efficiencies in bins of D^0 p_T and $y*$ for Fwd collision configuration.

$p_\mathrm{T}[\,\mathrm{GeV}/c]\backslash y*$	$(2.5, 3]$	$(3, 3.5]$	$(3.5, 4]$	$(4, 4.5]$	$(4.5, 5]$
$[0, 1]$	0.016 ± 0.002	0.061 ± 0.003	0.080 ± 0.002	0.063 ± 0.001	0.027 ± 0.004
$[1, 2]$	0.020 ± 0.001	0.067 ± 0.002	0.084 ± 0.002	0.066 ± 0.002	0.026 ± 0.002
$[2, 3]$	0.034 ± 0.002	0.104 ± 0.002	0.119 ± 0.001	0.091 ± 0.002	0.032 ± 0.002
$[3, 4]$	0.055 ± 0.002	0.147 ± 0.002	0.161 ± 0.002	0.118 ± 0.003	0.029 ± 0.002
$[4, 5]$	0.078 ± 0.003	0.174 ± 0.003	0.186 ± 0.003	0.120 ± 0.002	0.016 ± 0.003
$[5, 6]$	0.090 ± 0.004	0.195 ± 0.005	0.195 ± 0.005	0.102 ± 0.005	0.005 ± 0.002
$[6, 7]$	0.102 ± 0.005	0.196 ± 0.006	0.184 ± 0.007	0.071 ± 0.008	0.001 ± 0.001
$[7, 8]$	0.112 ± 0.007	0.193 ± 0.008	0.168 ± 0.011	0.037 ± 0.008	0.000 ± 0.000
$[8, 9]$	0.123 ± 0.008	0.188 ± 0.012	0.143 ± 0.016	0.022 ± 0.007	0.000 ± 0.000
$[9, 10]$	0.109 ± 0.008	0.166 ± 0.013	0.126 ± 0.020	0.010 ± 0.005	0.000 ± 0.000

Table 19: Tot efficiencies in bins of D^0 p_T and $y*$ for Bwd collision configuration.

| $p_\mathrm{T}[\,\mathrm{GeV}/c]\backslash y*$	$(2.5, 3]$	$(3, 3.5]$	$(3.5, 4]$	$(4, 4.5]$	$(4.5, 5]$
$[0, 1]$	0.019 ± 0.003	0.054 ± 0.004	0.065 ± 0.002	0.048 ± 0.001	0.017 ± 0.001
$[1, 2]$	0.023 ± 0.002	0.060 ± 0.002	0.070 ± 0.002	0.049 ± 0.001	0.016 ± 0.001
$[2, 3]$	0.039 ± 0.002	0.095 ± 0.002	0.100 ± 0.001	0.067 ± 0.002	0.015 ± 0.001
$[3, 4]$	0.065 ± 0.003	0.137 ± 0.002	0.135 ± 0.002	0.079 ± 0.003	0.013 ± 0.001
$[4, 5]$	0.090 ± 0.003	0.162 ± 0.002	0.156 ± 0.002	0.076 ± 0.002	0.005 ± 0.001
$[5, 6]$	0.108 ± 0.003	0.177 ± 0.003	0.159 ± 0.003	0.058 ± 0.005	0.001 ± 0.001
$[6, 7]$	0.121 ± 0.004	0.176 ± 0.006	0.146 ± 0.005	0.035 ± 0.007	0.000 ± 0.000
$[7, 8]$	0.125 ± 0.004	0.169 ± 0.007	0.122 ± 0.012	0.016 ± 0.005	0.000 ± 0.000
$[8, 9]$	0.134 ± 0.005	0.159 ± 0.009	0.097 ± 0.016	0.007 ± 0.004	0.000 ± 0.000
$[9, 10]$	0.111 ± 0.006	0.146 ± 0.011	0.074 ± 0.017	0.002 ± 0.003	0.000 ± 0.000
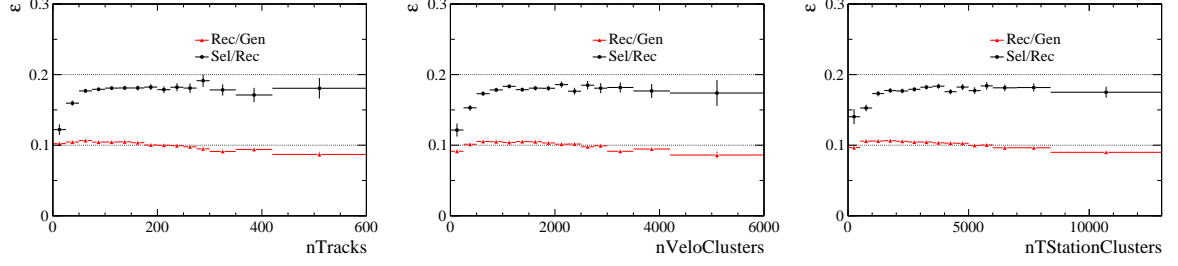
Figure 35: Reconstruction efficiency (red triangle) and selection efficiency (black filled circle). The numbers are scales for better visibility.

B   More on reconstruction-selection efficiencies

In Fig. 35, the reconstruction efficiency, which is the fraction of D^0 reconstructed with minimum requirements on the vertex and final state tracks (but no geometrical requirements related to PV), and the selection efficiency, which is the fraction of D^0 selected (in those reconstructed) using PV related variables including D^0 decaytime, $\chi^2_{\rm IP}$ of the final state tracks. It can be seen from the plot that, at high multiplicity the shape (efficiency decreasing at high multiplicity) is dominated by reconstruction efficiency, while at low multiplicity the shape (efficiency decreasing at low multiplicity) is dominated by the selection efficiency. The decreasing efficiency at high multiplicity is understood to be degraded tracking power; while the at low multiplicity, properly due to poorer resolution of PV reconstruction, and thus worse separation between the D^0 quantities and the PV.

C   Selections for the PID calibration sample

The stripping line for this sample is `NoPIDDstarWithD02RSKPiLine`. The reconstruction of D^0 starts from `StdAllNoPIDsPions` and `StdAllNoPIDsKaons`, the selections are listed in Table 20. The misID background of $D^0 \to \pi^- K^+, K^+ K^-, \pi^+ \pi^-$ are reduced by applying vetoing the $\pm 25 \, {\rm MeV}/c^2$ mass window in the corresponding mass hypotheses. The background is further reduced by tagging the $D^{*+}(2010)$, requiring the invariant mass of the D^0 with a soft pion in $\pm 75 \, {\rm MeV}/c^2$ of the $D^{*+}(2010)$ mass. The soft pion is required to have $p_{\rm T} > 150 \, {\rm MeV}/c$. The sum of the transverse momenta of the D^0 and the soft pion is required to larger than $2200 \, {\rm MeV}/c$. The $D^{*+}(2010)$ is also required to have good vertex fit quality.

D   Mass fit results

The result mean and sigma of the mass fits are given in Figs. 36 and 37 in bins of D^0 $(p_{\rm T}, y*)$ for the Fwd and Bwd collisions respectively. The mean value is almost constant over the kinematic bins, suggesting good alignment and reconstruction. The resolution

Table 20: Stripping selections for calibration D^0 sample.

Quantity	Selections
p_{T} (track)	$> 250\,\text{MeV}/c$
p (track)	$> 2000\,\text{MeV}/c$
χ^2_{IP} (track)	> 16
DIRA	> 0.9999
$\chi^2/\text{ndf}(\text{vtx})$	< 13
Vertex Displacement Chi2	$\chi^2(\text{VD}) > 49$
$p_{\text{T}}(D^0)$	$> 1.5\,\text{GeV}/c$
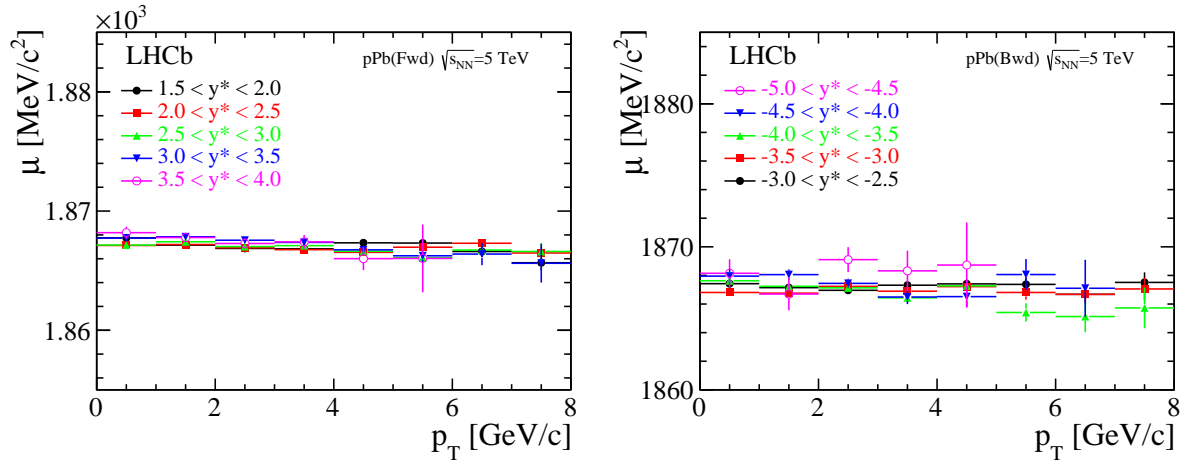
Figure 36: The μ parameter of the signal CB function from the D^0 invariant mass fit as a function of p_{T} and $y*$ for (left) Fwd and (right) Bwd configuration.

decreases with p_{T} as expected.

The $\log \chi^2_{\text{IP}}(D^0)$ distributions for the prompt D^0, $D^0{-}\text{from}{-}b$ and the sideband are given in Figs. 38, 39 and 40.

The invariant mass fit plots in each p_{T} and y^* bins are given in Fig. 41 and 42 for the Fwd and Bwd data respectively.

E PID systematic uncertainty

When fluctuating the single track PID efficiencies, the distribution of resulting D^0 PID efficiency is given in Figs. 43 and 44 for the Fwd and Bwd sample. Each distribution is fitted with a Gaussian function, and the width of the gaussian is quoted.
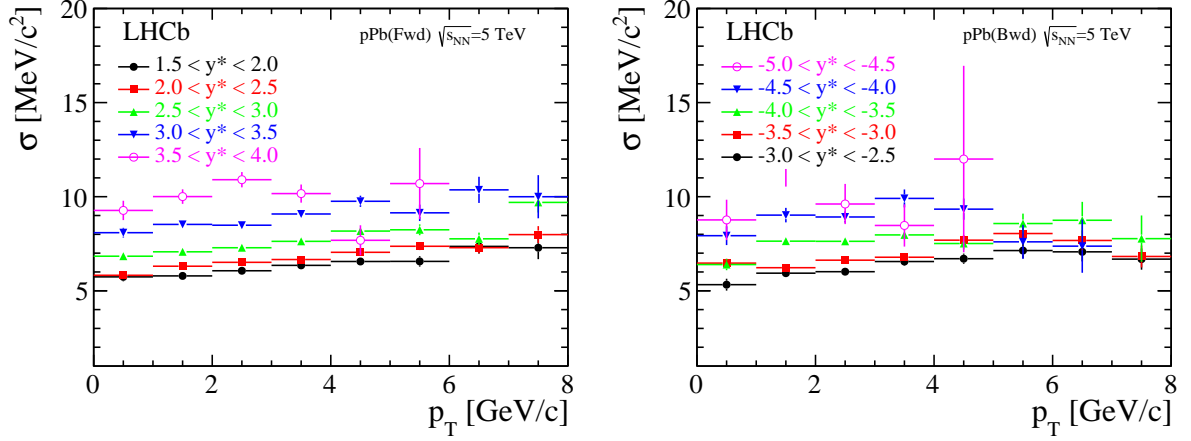
Figure 37: The σ parameter of the signal CB function from the D^0 invariant mass fit as a function of p_T and $y*$ for (left) Fwd and (right) Bwd configuration.
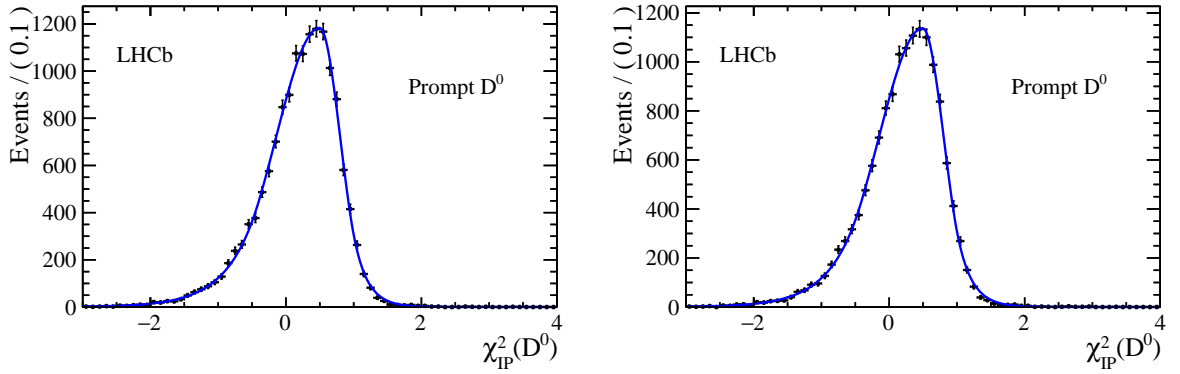
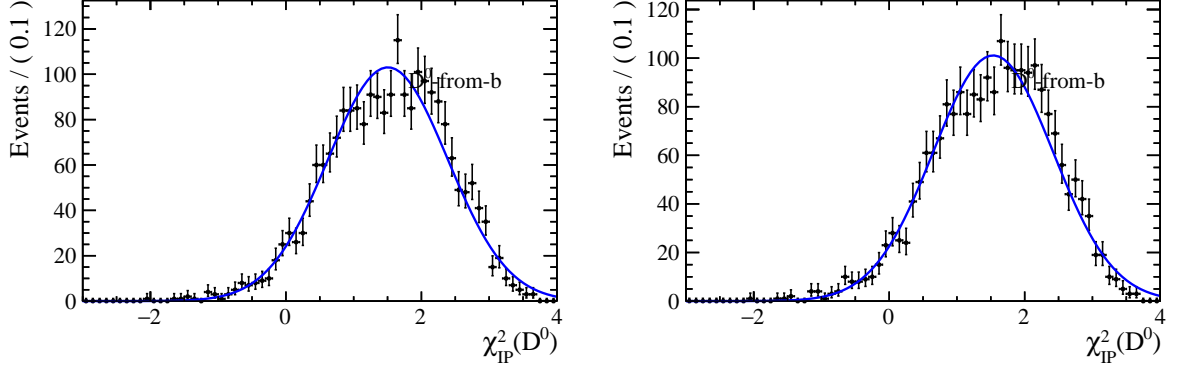

Figure 38: The $\log \chi^2_{IP}(D^0)$ distribution for prompt D^0, determined from simulation, corresponding the $y*$ range of (left) Fwd and (right) Bwd collision.

# F Geometrical selection

There is also a stripping line which only geometrical variables, constructed from the impact parameter of K^-, π^+, and D^0, and the closest distance of the two tracks d, $\nu_2 = ln(IP_K \times IP_\pi/(IP^2_{D^0} + d^2)) > 0$, and the other one, $nu_2p_T = log(nu_2 * p_{TK} * p_{T\pi}) > 14$. Offline we apply also the cuts in the nominal analysis except the PID. Due to prescale of 0.1 in both of stripping line and the one in the nominal analysis, and the two samples are almost totally statistically different. With this new selection, we repeat the analysis except the detailed systematic evaluation. The efficiency of the selections are roughly 50% of those in the nominal analysis at low D^0 p_T, and is very similar to the nominal one in high p_T bins. But it should be noted that, the two selections doesn't select exactly the same group of events, since for example in the nominal selections, the PID efficiency is around

Figure 39: The $\log \chi^2_{\text{IP}}(D^0)$ distribution for $D^0-$from$-b$, determined from simulation, corresponding the $y*$ range of (left) Fwd and (right) Bwd collision.
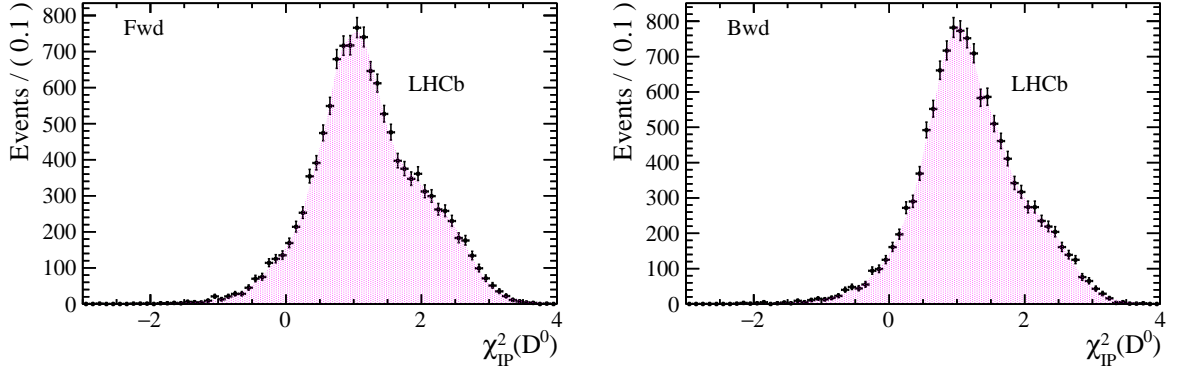
Figure 40: The $\log \chi^2_{\text{IP}}(D^0)$ distribution for data sideband events, for the (left) Fwd and (right) Bwd collision sample.

80%, and those rejected by PID in nominal selection could be accepted by the alternative selection. In Fig. 45, we compare the efficiency corrected yield in each bin between the two analysis as their pull distribution. The systematic uncertainties of nominal analysis haven been taken into account, while for the alternative one, only statistical uncertainty is included. From the plot, it can be concluded that the two selections are very similar. There could be slight bias between the two selections as the pull has an negative average, the difference can be attributed to additional systematic uncertainties in the alternative selections, for example the invariant mass fit which needs more work due to double and/or single misID peaking background.
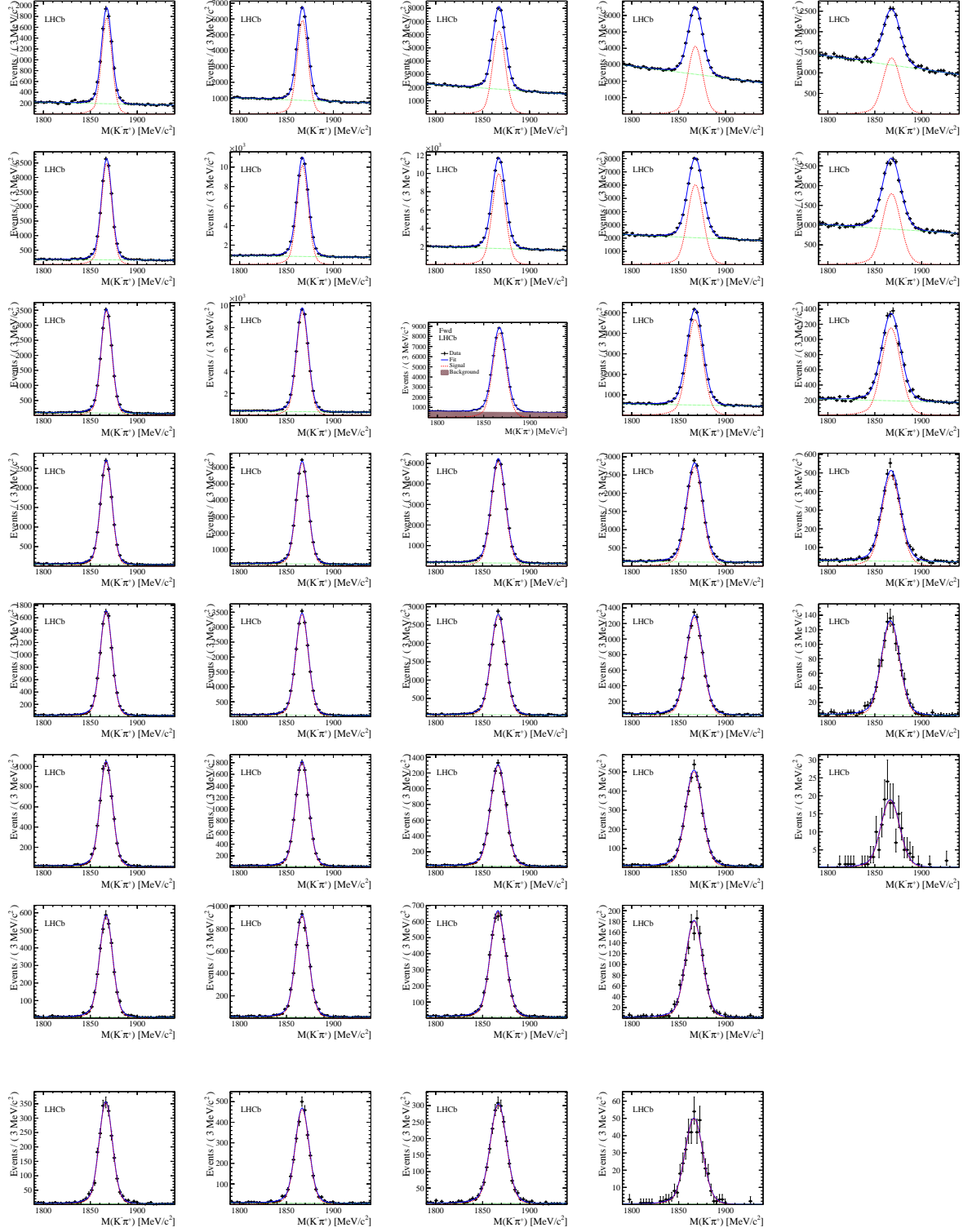
Figure 41: Invariant mass fit result in each p_T and y^* bin in the Fwd sample. The row runs for p_T bins, the column runs for y^* bins.

54
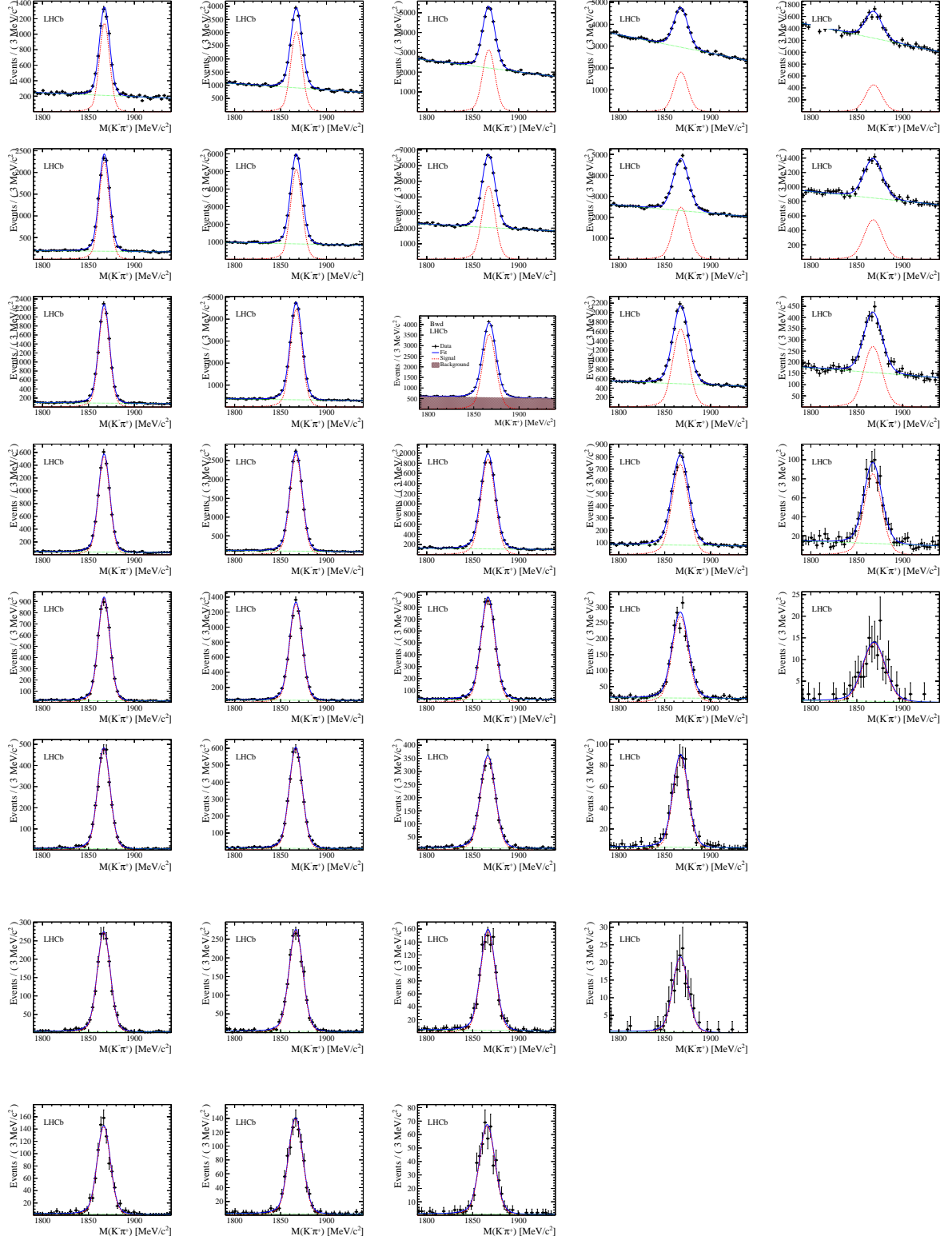
Figure 42: Invariant mass fit result in each p_T and y^* bin in the Bwd sample. The row runs for p_T bins, the column runs for y^* bins.

55

G Efficiency with private simulation production

Private Pbp (Bwd) simulation samples are generated using EPOS package to produce the minimum bias collision at $\sqrt{s_{NN}} = 5\,\mathrm{TeV}$, while signal D^0 are produced with Pythia and embedded into the EPOS simulation. The simulation is not affected by the truncation problem seen in PbPb collisions when the event multiplicity is quit high (corresponding to very high central collisions). The merged events then passed through LHCb simulation production steps. The details are documented here in the twiki page Heavy ion twiki. Due to computing power limited, only small samples are generated to validate (cross-check) the efficiency. The same codes to produce the nominal efficiencies are applied to the EPOS simulation sample. The most import thing to check is the reconstruction-selection efficiency. In Fig. 46, the efficiency as a function of different event multiplicities are shown. The efficiency in EPOS sample has been scaled by a factor of 107% to make the two match. The scale factor is due to the fact that in the EPOS sample, due to smaller center-of-mass energy (the pp simulation is at $\sqrt{s_{NN}} = 8\,\mathrm{TeV}$ corresponding to 2012 LHCb data), the p_{T} spectrum is softer and thus leading to smaller efficiency. Nevertheless, we see that the (shape) efficiencies in the two simulation productions agree with each other. Especially the one as a function of TStation clusters. There might be some drop of efficiency at high event multiplicity for efficiencies as functions of nTracks and nVeloClusters, but still in one-sigma agreement.

H Cross-section of D^0 in 5 TeV pp extrapolated with FONLL

The LHCb measured D^0 cross-sections at 7 and 13 TeV could be extrapolated 5 TeV incorporating the FONLL calculations, assuming that the FONLL could predict the collision energy dependence of the cross-section. In other words, the ratio of the D^0 cross-section at $\sqrt{s_{NN}} = 5\,\mathrm{TeV}$ over that at $\sqrt{s_{NN}} = 7\,\mathrm{TeV}$ (or $13\,\mathrm{TeV}$) is predicated by FONLL. Thus, we have $\frac{\sigma_i}{\sigma_j} = \frac{T_i}{T_j}$, where σ_i (T_i) is the real (FONLL predicted) cross-section at collision energy i. Using the LHCb measurements at 7 and 13 TeV, we get two predictions for the cross-section at 5 TeV as $\sigma_a \equiv \sigma_7 \frac{T_5}{T_7}$ or $\sigma_b \equiv \sigma_{13} \frac{T_5}{T_{13}}$. We take the weighted average of the two results, with the weight to be inverse of their uncertainties squared, as

$$\sigma_5 = \frac{\sigma_a \frac{1}{(\delta\sigma_a)^2} + \sigma_b \frac{1}{(\delta\sigma_b)^2} - \rho(\sigma_a + \sigma_b)\frac{1}{\delta\sigma_a \delta\sigma_b}}{\frac{1}{(\delta\sigma_a)^2} + \frac{1}{(\delta\sigma_b)^2} - 2\rho\frac{1}{\delta\sigma_a \delta\sigma_b}}, \delta\sigma_5^2 = \frac{1}{\frac{1}{(\delta\sigma_a)^2} + \frac{1}{(\delta\sigma_b)^2} - 2\rho\frac{1}{\delta\sigma_a \delta\sigma_b}},$$

where, $\delta\sigma_a = \delta\sigma_7 \frac{T_5}{T_7}$, $\delta\sigma_b = \delta\sigma_{13} \frac{T_5}{T_{13}}$. From the above equation, we can extract the effect of the correlation between the two systematic uncertainties. Assuming a correlation of 20%, the uncertainty will change by 10% The estimations using 13 TeV points and 7 TeV points give different results, for example in the common rapidity bin, $\sigma_{7\,\mathrm{TeV}}(p_{\mathrm{T}} < 8\,\mathrm{GeV}/c, 2.5 < |y| < 4) = 814 \pm 66\,\mu\mathrm{b}$ and $\sigma_{13\,\mathrm{TeV}}(p_{\mathrm{T}} < 8\,\mathrm{GeV}/c, 2.5 < |y| < 4) = 1063 \pm 65\,\mu\mathrm{b}$. The uncertainty from FONLL predictions are evaluated by varying the scales and PDF, as

870 given by the predictions. The largest variation w.r.t the nominal values are taken as uncertainty due to theory. The numbers are summarized in right column of Table 21.

Table 21: The extrapolated prompt D^0 cross-section at $\sqrt{s_{pp}} = 5\,\mathrm{TeV}$ in different p_T range integrated over the rapidity range $2.5 < y < 4$. The first uncertainty is from the fit, i.e. due to uncertainties of cross-section measurements at 7 and 13 TeV; the second is from comparison of fit models for the "fit" case, or from theory uncertainties in the "FONLL" case. The FONLL extrapolation result is quoted here for internal comparison but not for the results of this analysis. Refer to text for the discussions.

$p_\mathrm{T}[\,\mathrm{GeV}/c]$	Analytical fit	FONLL
$[0, 1]$	$183.74 \pm 24.76 \pm 5.25$	$269.46 \pm 14.43 \pm 18.52$
$[1, 2]$	$285.33 \pm 37.69 \pm 4.14$	$363.04 \pm 17.94 \pm 55.98$
$[2, 3]$	$142.94 \pm 18.60 \pm 4.30$	$187.12 \pm 8.82 \pm 15.75$
$[3, 4]$	$57.15 \pm 7.80 \pm 5.35$	$78.80 \pm 3.71 \pm 4.34$
$[4, 5]$	$25.55 \pm 3.75 \pm 2.94$	$37.84 \pm 1.67 \pm 1.51$
$[5, 6]$	$12.69 \pm 2.07 \pm 1.39$	$19.65 \pm 0.85 \pm 0.36$
$[6, 7]$	$5.92 \pm 1.11 \pm 0.93$	$9.57 \pm 0.45 \pm 0.13$
$[7, 8]$	$2.84 \pm 0.74 \pm 0.64$	$5.49 \pm 0.29 \pm 0.06$
$[0, 8]$	$713.6 \pm 94.5 \pm 46.6$	$949.7 \pm 46.9 \pm 83.3$

871

872 The extrapolated cross-section of D^0 in 5 TeV pp collisions are different between
873 two analytic method and FONLL method. This is understood to be that, the LHCb
874 measurements at 7 and 13 TeV suggest that the cross-section as a function of the colliding
875 center-of-mass energy is a power law function with $p_0 \approx 1$ (approximately linear), while
876 in the FONLL prediction, $p_0 \approx 2/3 \pm 0.1$ significantly less than unity. The discrepancy
877 can be seen directly in Fig. 47. Since FONLL predicts weaker energy dependence, in the
878 extrapolation using FONLL the cross-section at 5 TeV is more close to 7 and/or 13 TeV,
879 but it is smaller in the linear extrapolation. The inconsistency between the two results is
880 also seen in reference [40], where the ratio of D^0 differential cross-section at 13 TeV over
881 that at 7 TeV is found to be larger than that predicted by FONLL.

882 # I Uncertainty propagation

Suppose there are two variables v_1, and v_2, and their relative uncertainties $[x_i, y_j]$, $[X_m, z_n]$, respectively. There are no correlations among different sources of uncertainties. $x_i, X_m, i == m$ are totally correlated, and while y_i, Z_n are not correlated with each other and with other uncertainties. Let $r = v_1/v_2$, then we have $\log r = \log v_1 - \log v_2$, and $\delta r/r = \sqrt{(\delta v_1/v_1)^2 + (\delta v_2/v_2)^2 - 2\rho * (\delta v_1/v_1) * (\delta v_2/v_2)}$. The total relative uncertainty $\delta v_1/v_1 = \sqrt{\sum x_i^2 + \sum y_j^2}$, and $\delta v_2/v_2 = \sqrt{\sum X_m^2 + \sum z_n^2}$. The correlation between the total uncertainties of δv_1 and $\delta_v 2$ is

$$\rho = \frac{\sum (x_i * v_1) * (X_i * v_2)}{\delta v_1 * \delta v_2} = \frac{\sum x_i * X_i}{(\delta v_1/v_1) * (\delta v_2/v_2)}.$$

That is

$$\rho * (\delta v_1/v_1) * (\delta v_2/v_2) \equiv 2 * \sum x_i * X_i.$$

Then we have

$$\delta r/r = \sqrt{(\delta v_1/v_1)^2 + (\delta v_2/v_2)^2 - 2 * \sum x_i * X_i}.$$

This is the final equation, which allows us calculate simply the uncertainties of the ratios, without the need of investigating the details of each component. For example, suppose the cross-section at 13 TeV is $1000\,\mu$b $\pm\,50\,\mu$b, and the one at 5 TeV is $400\,\mu$b $\pm$ $30\,\mu$b, and the correlated uncertainty between the two is $20\,\mu$b in the first number and $5\,\mu$b in the second number. The uncertainty of the ratio is thus calculated as $\sqrt{(50/1000)^2 + (30/400)^2 - 2 * 20/1000 * 5/400} = 8.7\%$.

J   Investigations of pp reference cross-section measurement

NOTE, only for LHCb internal.

First we saw that the measured D^0 rapidity distributions are very different in pPb analysis and that in pp at 5 TeV as shown in Fig. 48. This could explain why we get a strange shape for $R_{p\mathrm{Pb}}$ as a function of $y*$. The pPb result is more like the one predicted by FONLL. More comparisons are made among different analyses of D^0 cross-sections in pp at $5, 7, 13$ TeV, pPb at 5 TeV. Basically, the measurement in pPb data are more consistent with the measurement in pp at 7 TeV (both are RunI data), but not those at RunII (pp at $5, 13$ TeV). In particular, for the rapidity bin $2 < y < 2.5$, the 5 TeV result is even higher than the 7 TeV result, which should not be true. No inconsistencies are found between 5 TeV and 13 TeV pp measurements, and their ratio is found to be described by FONLL, which could be understood since both are RunII measurements and are made with similar conditions (trigger, selections, simulation samples).

As we already know that, for RunII simulation (sim09a), a large correction, evaluated using the J/ψ sample by the tracking group, should be applied to the simulation samples due to improper modelling of the second metal effect in VELO, and the correction is found to be function of rapidity. The correction table gives 10% correction in the rapidity bin $2 < y < 2.5$ of D^0. To understand why the corrections could fully remove the discrepancies seen between simulation and data, a new simulation sample (sim09b) is studied which should be not be affected by the second metal effect. We didn't try to repeat the whole pp at 5 TeV analysis but just compare the reconstruction efficiencies in the sim09a and sim09b samples. In Fig. 49, the efficiency as a function of y is shown for the $1 < p_{\mathrm{T}} < 2$ bins (similar behavior for other bins), as can be seen, large discrepancy is identified decreasing with increasing rapidity. The discrepancy is as large as 30% in the first rapidity bin, which is much larger than the value obtained using tracking correction table. If we correct the measurement of D^0 cross section in pp at 5 TeV using the ratio of the efficiency in sim09b and sim09a, assuming other efficiencies unchanged (and with the tracking efficiency correction factors already applied in original paper removed), we could get the following

58

cold nuclear modification factors, shown in Fig. 50 and 51, which are more as expected. Further studies of J/ψ simulation samples between sim09a and sim09b also suggest that the tracking correction table is not enough to take the second metal effect into account. More details of the studies can be found in the recent IFT wg update: `slides`.

References

[1] B. A. Kniehl, G. Kramer, I. Schienbein, and H. Spiesberger, *Reconciling open charm production at the Fermilab Tevatron with QCD*, Phys. Rev. Lett. **96** (2006) 012001, `arXiv:hep-ph/0508129`.

[2] B. A. Kniehl, G. Kramer, I. Schienbein, and H. Spiesberger, *Inclusive Charmed-Meson Production at the CERN LHC*, Eur. Phys. J. **C72** (2012) 2082, `arXiv:1202.0439`.

[3] M. Cacciari, M. Greco, and P. Nason, *The P(T) spectrum in heavy flavor hadroproduction*, JHEP **05** (1998) 007, `arXiv:hep-ph/9803400`.

[4] M. Cacciari and P. Nason, *Charm cross-sections for the Tevatron Run II*, JHEP **09** (2003) 006, `arXiv:hep-ph/0306212`.

[5] M. Cacciari *et al.*, *Theoretical predictions for charm and bottom production at the LHC*, JHEP **10** (2012) 137, `arXiv:1205.6344`.

[6] R. Maciula and A. Szczurek, *Open charm production at the LHC - k_t-factorization approach*, Phys. Rev. **D87** (2013), no. 9 094022, `arXiv:1301.3033`.

[7] STAR, J. Adams *et al.*, *Experimental and theoretical challenges in the search for the quark gluon plasma: The STAR Collaboration's critical assessment of the evidence from RHIC collisions*, Nucl. Phys. **A757** (2005) 102, `arXiv:nucl-ex/0501009`.

[8] ALICE, B. Abelev *et al.*, *Suppression of high transverse momentum D mesons in central Pb-Pb collisions at $\sqrt{s_{NN}} = 2.76$ TeV*, JHEP **09** (2012) 112, `arXiv:1203.2160`.

[9] J. Uphoff, O. Fochler, Z. Xu, and C. Greiner, *Open Heavy Flavor in Pb+Pb Collisions at $\sqrt{s} = 2.76$ TeV within a Transport Model*, Phys. Lett. **B717** (2012) 430, `arXiv:1205.4945`.

[10] M. He, R. J. Fries, and R. Rapp, *Heavy Flavor at the Large Hadron Collider in a Strong Coupling Approach*, Phys. Lett. **B735** (2014) 445, `arXiv:1401.3817`.

[11] S. Wicks, W. Horowitz, M. Djordjevic, and M. Gyulassy, *Elastic, inelastic, and path length fluctuations in jet tomography*, Nucl. Phys. **A784** (2007) 426, `arXiv:nucl-th/0512076`.

[12] W. A. Horowitz, *Testing pQCD and AdS/CFT Energy Loss at RHIC and LHC*, AIP Conf. Proc. **1441** (2012) 889, `arXiv:1108.5876`.

[13] R. Sharma, I. Vitev, and B.-W. Zhang, *Light-cone wave function approach to open heavy flavor dynamics in QCD matter*, Phys. Rev. **C80** (2009) 054902, arXiv:0904.0032.

[14] M. Arneodo, *Nuclear effects in structure functions*, Phys. Rept. **240** (1994) 301.

[15] S. Malace, D. Gaskell, D. W. Higinbotham, and I. Cloet, *The Challenge of the EMC Effect: existing data and future directions*, Int. J. Mod. Phys. **E23** (2014) 1430013, arXiv:1405.1270.

[16] K. J. Eskola, H. Paukkunen, and C. A. Salgado, *EPS09: A New Generation of NLO and LO Nuclear Parton Distribution Functions*, JHEP **04** (2009) 065, arXiv:0902.4154.

[17] D. de Florian and R. Sassot, *Nuclear parton distributions at next-to-leading order*, Phys. Rev. **D69** (2004) 074028, arXiv:hep-ph/0311227.

[18] M. Hirai, S. Kumano, and T.-H. Nagai, *Determination of nuclear parton distribution functions and their uncertainties in next-to-leading order*, Phys. Rev. **C76** (2007) 065207, arXiv:0709.3038.

[19] H. Fujii and K. Watanabe, *Heavy quark pair production in high energy pA collisions: Open heavy flavors*, Nucl. Phys. **A920** (2013) 78, arXiv:1308.1258.

[20] P. Tribedy and R. Venugopalan, *QCD saturation at the LHC: Comparisons of models to p + p and A + A data and predictions for p + Pb collisions*, Phys. Lett. **B710** (2012) 125, arXiv:1112.2445, [Erratum: Phys. Lett.B718,1154(2013)].

[21] J. L. Albacete, A. Dumitru, H. Fujii, and Y. Nara, *CGC predictions for p + Pb collisions at the LHC*, Nucl. Phys. **A897** (2013) 1, arXiv:1209.2001.

[22] A. H. Rezaeian, *CGC predictions for p+A collisions at the LHC and signature of QCD saturation*, Phys. Lett. **B718** (2013) 1058, arXiv:1210.2385.

[23] I. Vitev, *Non-Abelian energy loss in cold nuclear matter*, Phys. Rev. **C75** (2007) 064906, arXiv:hep-ph/0703002.

[24] M. Lev and B. Petersson, *Nuclear Effects at Large Transverse Momentum in a QCD Parton Model*, Z. Phys. **C21** (1983) 155.

[25] F. Arleo, S. Peigne, and T. Sami, *Revisiting scaling properties of medium-induced gluon radiation*, Phys. Rev. **D83** (2011) 114036, arXiv:1006.0818.

[26] LHCb collaboration, R. Aaij *et al.*, *Measurement of two-particle correlations in proton-ion collisions at* $\sqrt{s_{NN}} = 5$ *TeV*, arXiv:1512.00439, to appear in Phys.Lett.B.

[27] CMS, S. Chatrchyan *et al.*, *Observation of long-range near-side angular correlations in proton-lead collisions at the LHC*, Phys. Lett. **B718** (2013) 795, arXiv:1210.5482.

[28] ALICE, B. Abelev *et al.*, *Long-range angular correlations on the near and away side in p-Pb collisions at* $\sqrt{s_{NN}} = 5.02$ *TeV*, Phys. Lett. **B719** (2013) 29, arXiv:1212.2001.

[29] ATLAS, G. Aad *et al.*, , Phys. Rev. Lett. **110** (2013), no. 18 182302, arXiv:1212.5198.

[30] PHENIX, S. S. Adler *et al.*, *Nuclear effects on hadron production in d = Au and p + p collisions at s(NN)**(1/2) = 200-GeV*, Phys. Rev. **C74** (2006) 024904, arXiv:nucl-ex/0603010.

[31] PHENIX, A. Adare *et al.*, , Phys. Rev. Lett. **111** (2013), no. 20 202301, arXiv:1305.5516.

[32] LHCb collaboration, *Study of* $\psi(2S)$ *production and cold nuclear matter effects in pPb collisions at* $\sqrt{s_{NN}} = 5$ *TeV*, LHCb-CONF-2015-005.

[33] PHENIX, A. Adare *et al.*, *Cold-nuclear-matter effects on heavy-quark production in d+Au collisions at* $\sqrt{s_{NN}} = 200$ *GeV*, Phys. Rev. Lett. **109** (2012), no. 24 242301, arXiv:1208.1293.

[34] ALICE, B. B. Abelev *et al.*, *Suppression of* $\psi(2S)$ *production in p-Pb collisions at* $\sqrt{s_{NN}} = 5.02$ *TeV*, JHEP **12** (2014) 073, arXiv:1405.3796.

[35] PHENIX, A. Adare *et al.*, , Phys. Rev. Lett. **112** (2014), no. 25 252301, arXiv:1310.1005.

[36] STAR, J. Adams *et al.*, *Open charm yields in d + Au collisions at s(NN)**(1/2) = 200-GeV*, Phys. Rev. Lett. **94** (2005) 062301, arXiv:nucl-ex/0407006.

[37] LHCb collaboration, A. A. Alves Jr. *et al.*, *The LHCb detector at the LHC*, JINST **3** (2008) S08005.

[38] LHCb collaboration, R. Aaij *et al.*, *Study of J/ψ production and cold nuclear matter effects in pPb collisions at* $\sqrt{s_{NN}} = 5$ *TeV*, JHEP **02** (2014) 072, arXiv:1308.6729.

[39] LHCb collaboration, R. Aaij *et al.*, *Prompt charm production in pp collisions at* $\sqrt{s} = 7$ *TeV* , Nucl. Phys. **B871** (2013) 1, arXiv:1302.2864.

[40] LHCb collaboration, R. Aaij *et al.*, *Measurements of prompt charm production cross-sections in pp collisions at* $\sqrt{s} = 13$ *TeV*, JHEP **03** (2016) 159, arXiv:1510.01707.

[41] Particle Data Group, K. A. Olive *et al.*, *Review of particle physics*, Chin. Phys. **C38** (2014) 090001, and 2015 update.

[42] M. L. Miller, K. Reygers, S. J. Sanders, and P. Steinberg, *Glauber modeling in high energy nuclear collisions*, Ann. Rev. Nucl. Part. Sci. **57** (2007) 205, arXiv:nucl-ex/0701025.

[43] ALICE, J. Adam *et al.*, *Centrality dependence of particle production in p-Pb collisions at $\sqrt{s_{\mathrm{NN}}}$= 5.02 TeV*, Phys. Rev. **C91** (2015), no. 6 064905, arXiv:1412.6828.

[44] LHCb collaboration, R. Aaij *et al.*, *Measurements of prompt charm production cross-sections in pp collisions at $\sqrt{s} = 5$ TeV*, arXiv:1610.02230, submitted to JHEP.

[45] T. Skwarnicki, *A study of the radiative cascade transitions between the Upsilon-prime and Upsilon resonances*, PhD thesis, Institute of Nuclear Physics, Krakow, 1986, DESY-F31-86-02.

[46] J.-P. Lansberg and H.-S. Shao, *Towards an automated tool to evaluate the impact of the nuclear modification of the gluon density on quarkonium, D and B meson production in proton–nucleus collisions*, Eur. Phys. J. **C77** (2017), no. 1 1, arXiv:1610.05382.

[47] H.-S. Shao, *HELAC-Onia 2.0: an upgraded matrix-element and event generator for heavy quarkonium physics*, Comput. Phys. Commun. **198** (2016) 238, arXiv:1507.03435.

[48] H.-S. Shao, *HELAC-Onia: An automatic matrix element generator for heavy quarkonium physics*, Comput. Phys. Commun. **184** (2013) 2562, arXiv:1212.5293.

[49] K. J. Eskola, H. Paukkunen, and C. A. Salgado, *EPS09: A New Generation of NLO and LO Nuclear Parton Distribution Functions*, JHEP **04** (2009) 065, arXiv:0902.4154.

[50] K. Kovarik *et al.*, *nCTEQ15 - Global analysis of nuclear parton distributions with uncertainties in the CTEQ framework*, Phys. Rev. **D93** (2016), no. 8 085037, arXiv:1509.00792.

[51] H.-L. Lai *et al.*, *New parton distributions for collider physics*, Phys. Rev. **D82** (2010) 074024, arXiv:1007.2241.

[52] M. L. Mangano, P. Nason, and G. Ridolfi, *Heavy quark correlations in hadron collisions at next-to-leading order*, Nucl. Phys. **B373** (1992) 295.

[53] D. Stump *et al.*, *Inclusive jet production, parton distributions, and the search for new physics*, JHEP **10** (2003) 046, arXiv:hep-ph/0303013.

[54] B. Ducl006, T. Lappi, and H. Mäntysaari, *Forward J/ψ production in proton-nucleus collisions at high energy*, Phys. Rev. **D91** (2015), no. 11 114005, arXiv:1503.02789.
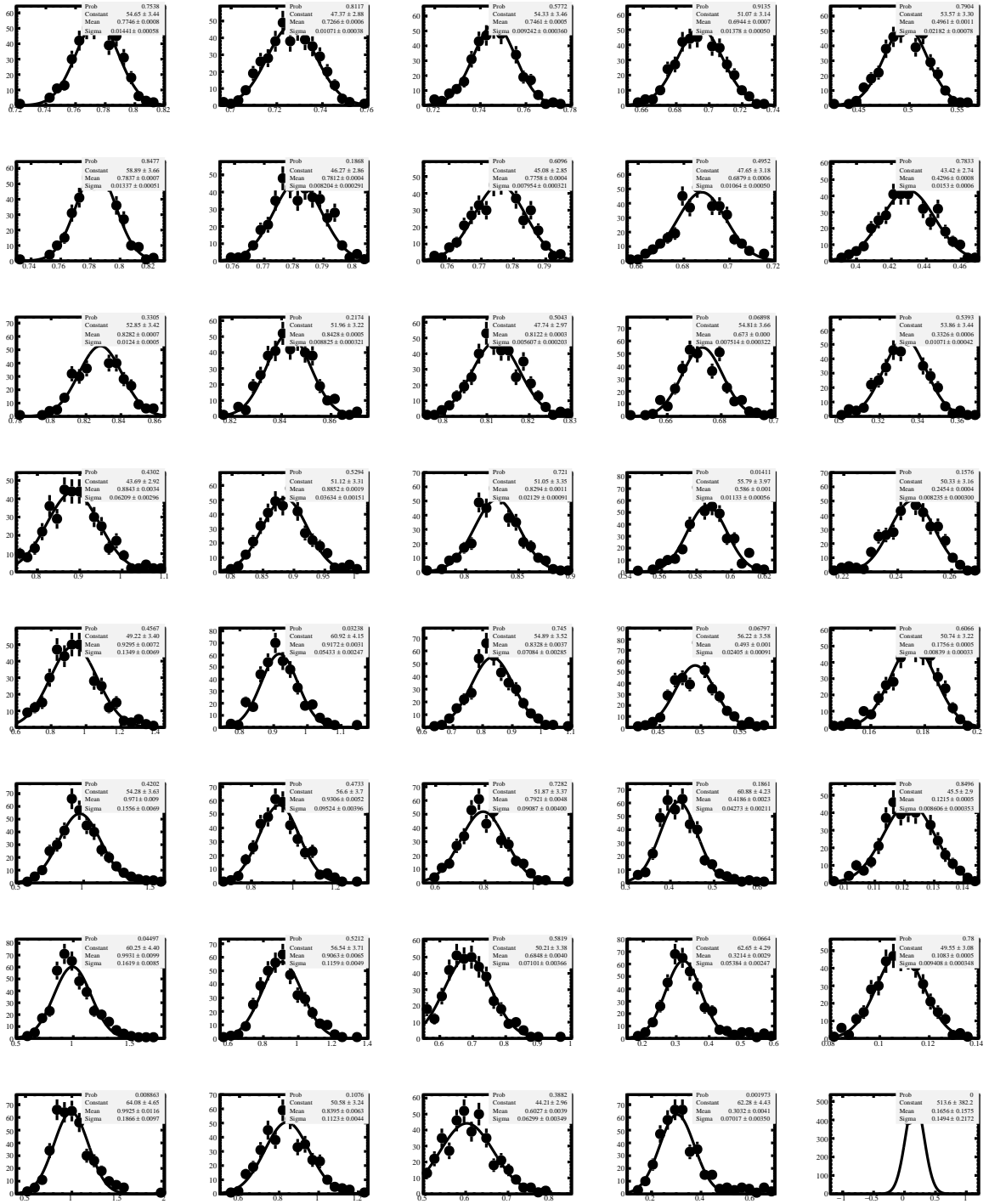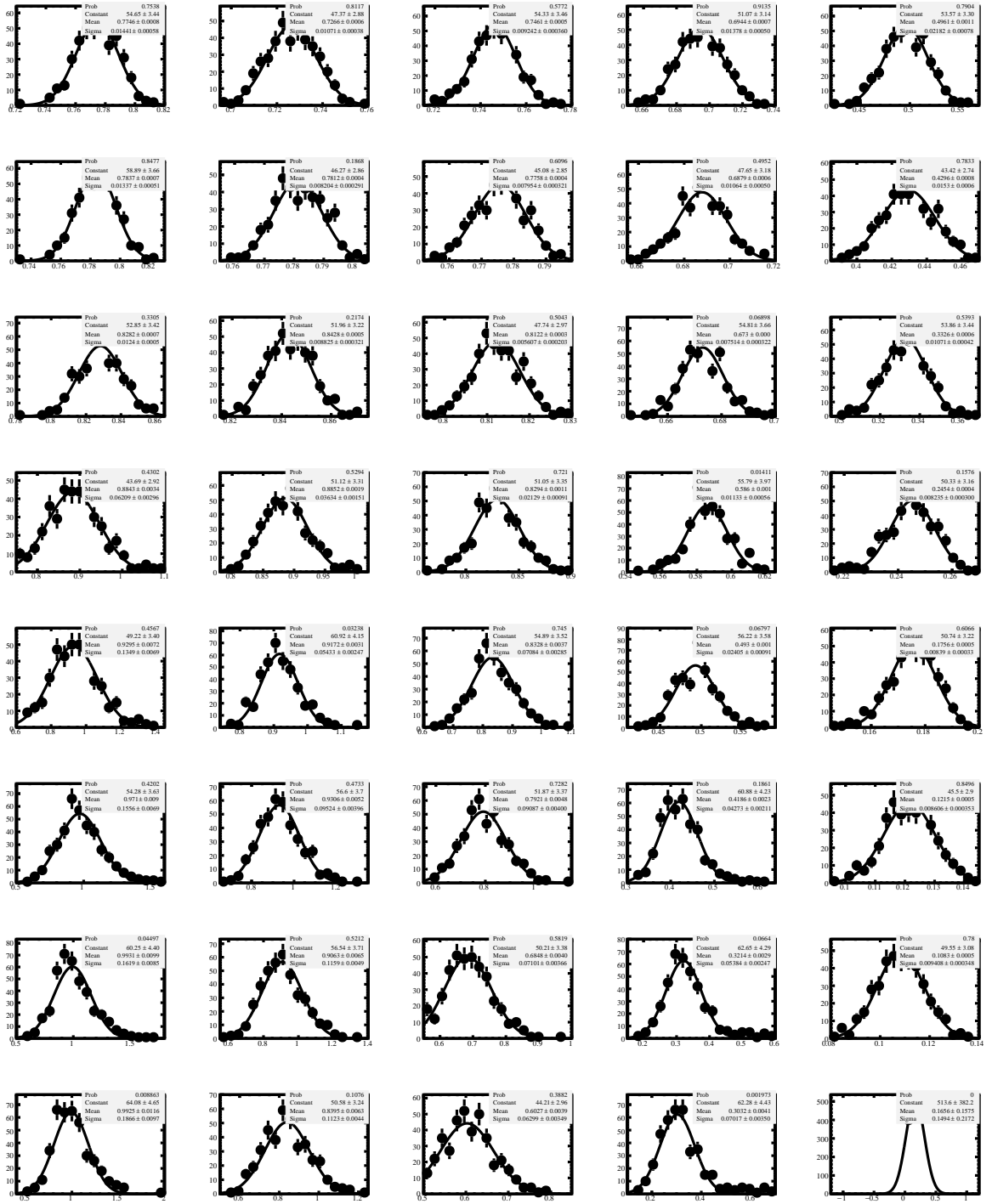
Figure 43: Distribution of PID efficiencies with respect to the fluctuation of single track efficiency simultaneously for K^- and π^+, in the Fwd collision sample. Plots correspond to different D^0 (p_T, y^*) bins.
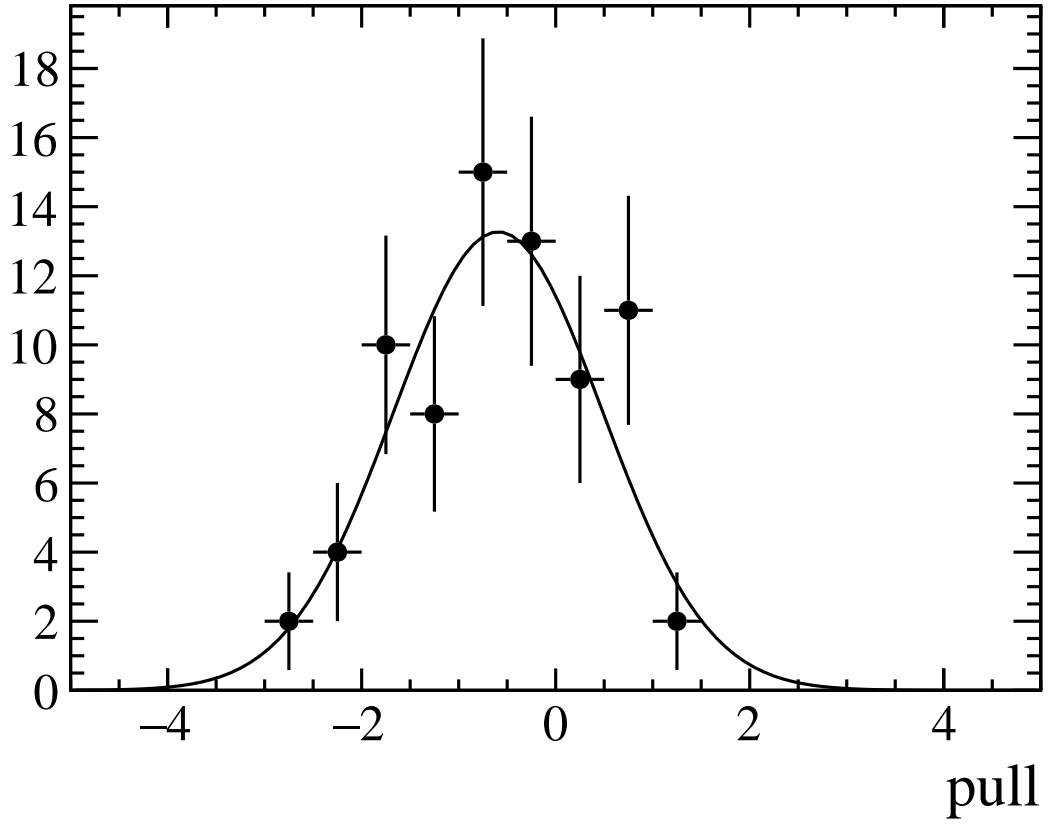
Figure 44: Distribution of PID efficiencies with respect to the fluctuation of single track efficiency simultaneously for K^- and π^+, in the Bwd collision sample. Plots correspond to different D^0 (p_T, y^*) bins.

64

Figure 45: Pull distribution of efficiency corrected yield,
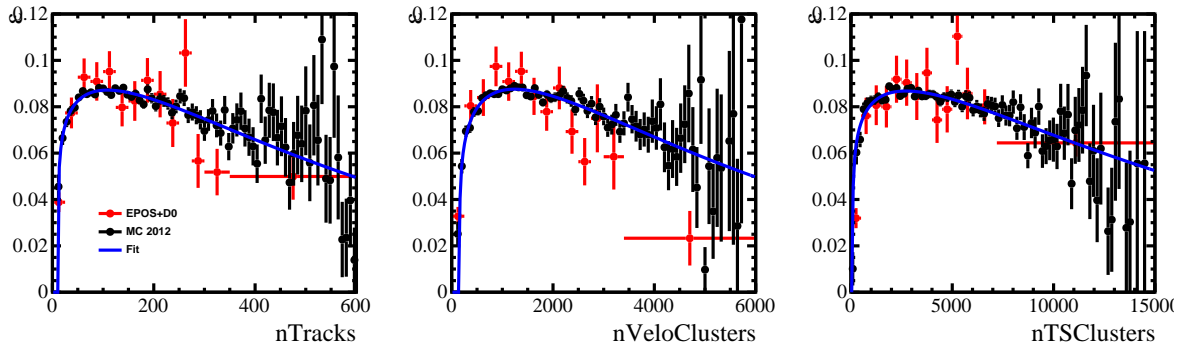
Figure 46: Efficiency in pp simulation compared to private Pbp simulation.
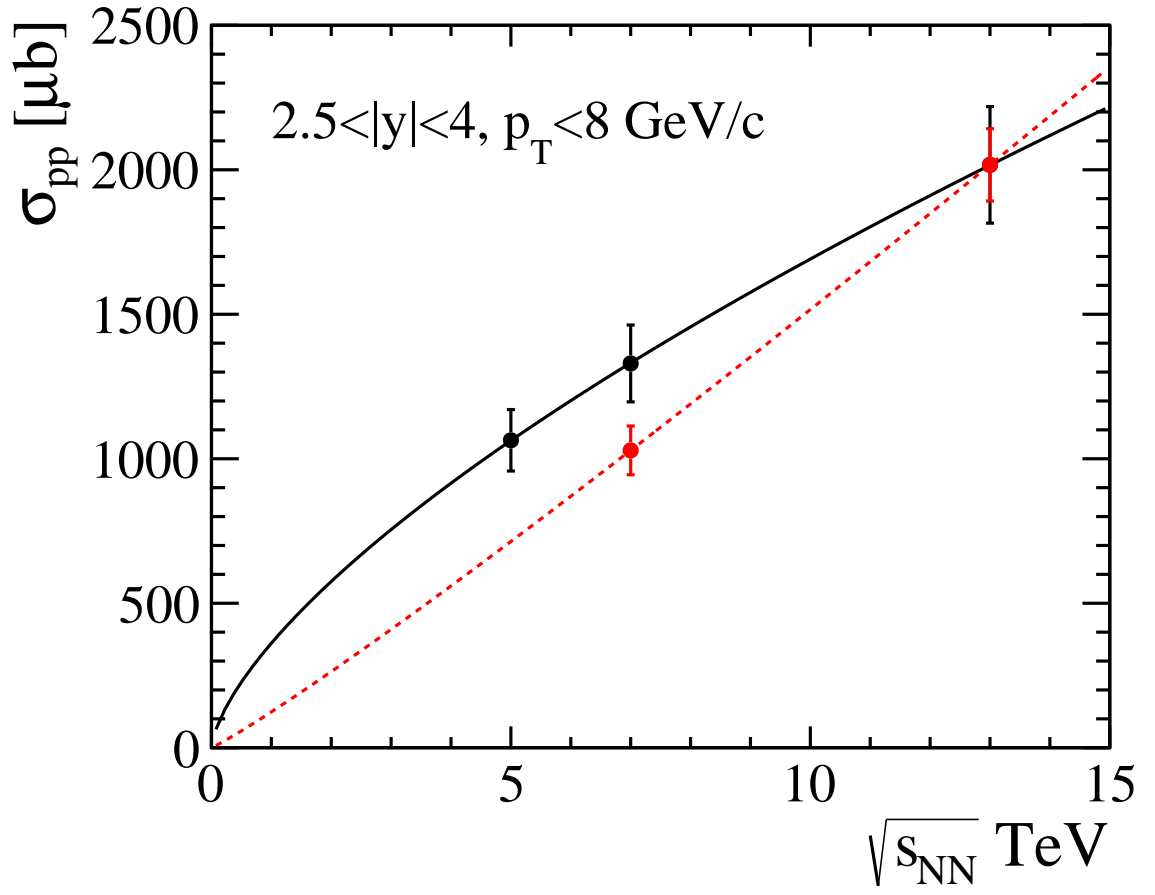
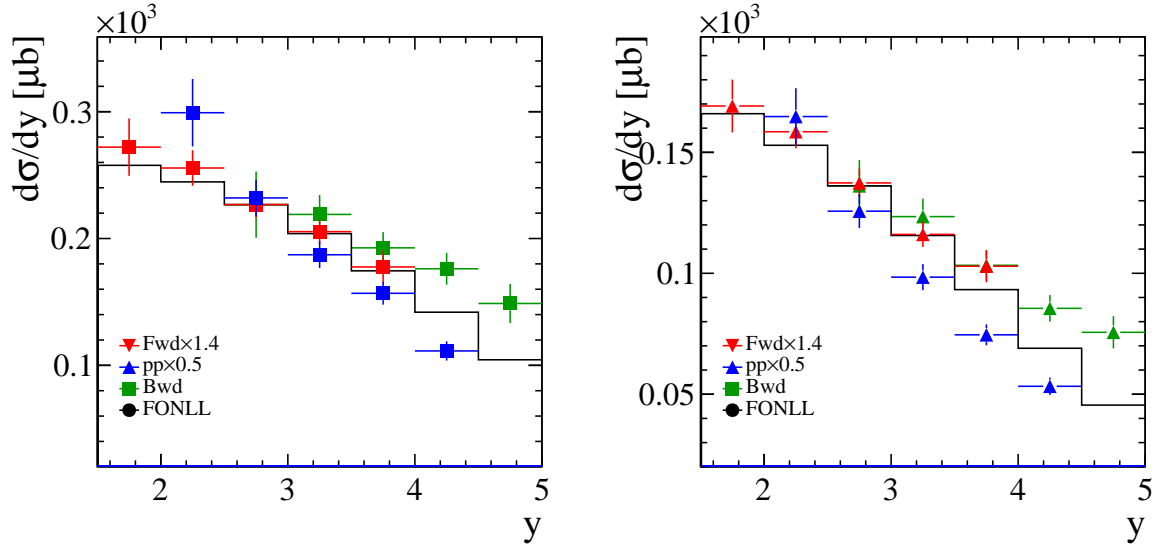Figure 47: Comparison of FONLL predicated cross-sections and LHCb measurements.

Figure 48: Comparison of D^0 cross-section as a function of y for p_T bins (left) $1 < p_T < 2$ TeVand (right) $2 < p_T < 3$ GeV, measured in pp at $\sqrt{s} = 5$ TeV and pPb Fwd and Bwd at $\sqrt{s_{NN}} = 5$ TeV. FONLL predictions are also shown for a comparison.
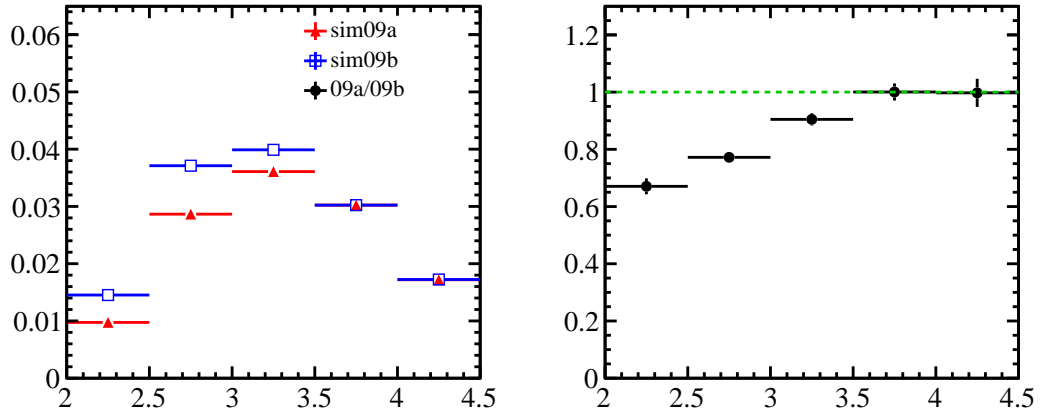

Figure 49: (left) Reconstruction efficiency as a function of rapidity for the p_T bin $1 < p_T < 2$ GeV evaluated using the sim09a and sim09b simulation sample respectively, (right) their ratio.
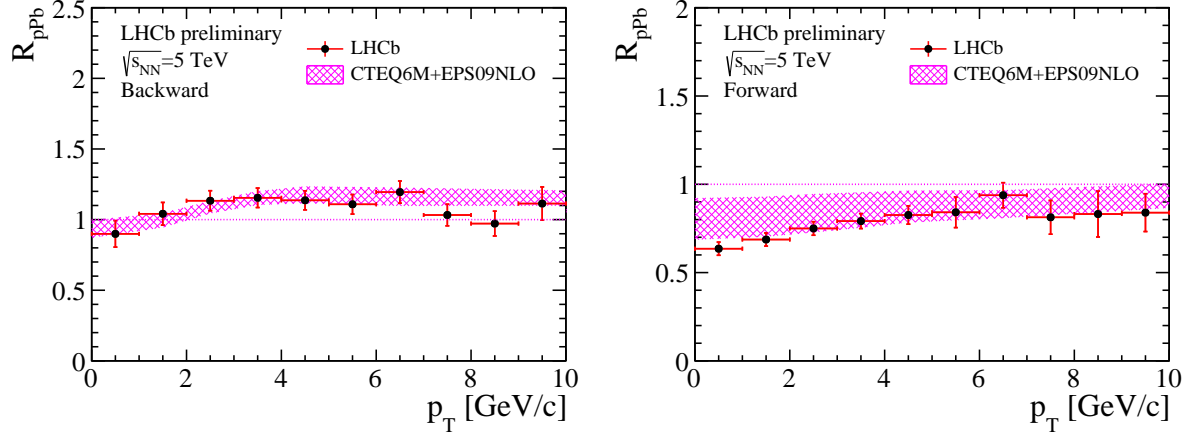
Figure 50: Nuclear modification factor $R_{p\mathrm{Pb}}$ as a function of p_T for prompt D^0 in the (left) forward data and (right) backward data, integrated over the common rapidity range $2.5 < |y^*| < 4$. The measurement of D^0 cross-section in pp at 5 TeV is corrected using the efficiency ratio between sim09b and sim09a.
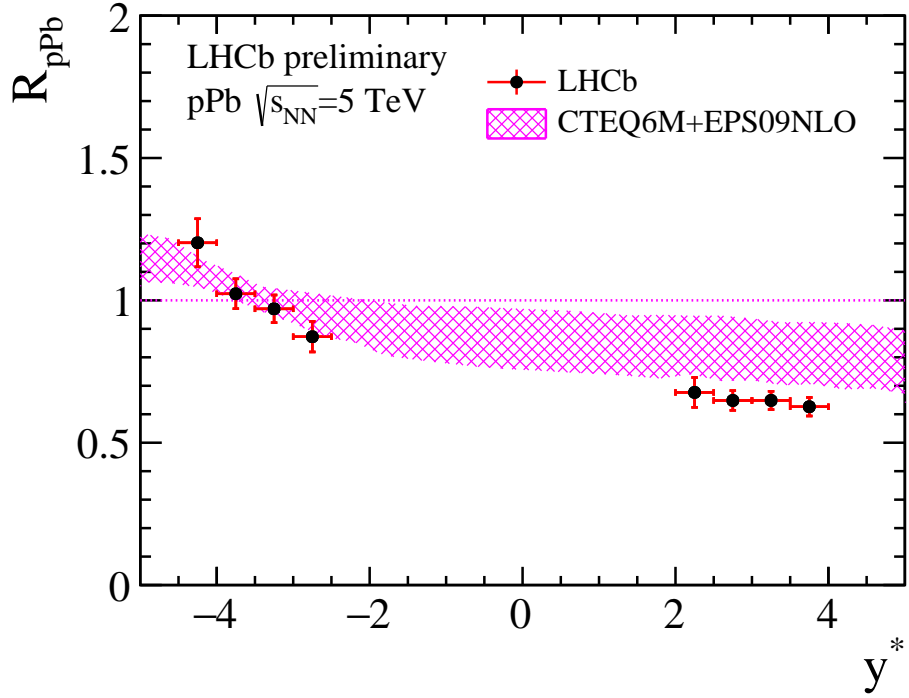

Figure 51: Nuclear modification factor $R_{p\mathrm{Pb}}$ in bins of y^* for prompt D^0, integrated over the p_T range $pt < 10\,\mathrm{GeV}/c$. In the right plots, more y^* bins are used. The uncertainty is the quadratic sum of the statistical and systematic components. The measurement of D^0 cross-section in pp at 5 TeV is corrected using the efficiency ratio between sim09b and sim09a.